Doctoral Dissertation

Development of novel dissimilar linear friction welding methods of steels and aluminum alloys

FURKAN

July 2025

Division of Materials and Manufacturing Science
Graduate School of Engineering
The University of Osaka

*This thesis is lovingly dedicated to my beloved mother, **Afsaree Bano.***

Acknowledgement

First of all, I would like to express my deepest gratitude and sincere appreciation to Director/Professor Hidetoshi FUJII of the Joining and Welding Research Institute (JWRI), The University of Osaka, for providing me with an excellent research environment and for his warm and dedicated guidance and encouragement throughout the course of this study and the preparation of this thesis. Under his passionate supervision, I have not only gained technical expertise but also grown significantly on a personal level. I am sincerely thankful for his unwavering support.

I would like to extend my heartfelt gratitude to Professor Ninshu MA of the Joining and Welding Research Institute, and Professor Hiroyuki Y. YASUDA of the Division of Materials and Manufacturing Science, Graduate School of Engineering, The University of Osaka, for their invaluable advice and insightful feedback to improve further.

I am also profoundly grateful to Professor Kohsaku USHIODA and Associate Professor Yoshiaki MORISADA for their kind support, expert guidance, and thoughtful discussions throughout my Ph.D. research. Professor USHIODA's dedication, especially during progress meetings and technical panel discussions, provided invaluable direction and encouragement, which have greatly enriched my research. Also, I cherish our early morning walks at a quarter past five during the JWS meetings, which offered both inspiration and meaningful conversation. Professor MORISADA's insightful advice and technical expertise were crucial in advancing the quality and depth of this study. I deeply appreciate his continuous support and mentorship.

I would also like to thank Assistant Professor Takuya MIURA for his kind and consistent support in experiments.

Special thanks are extended to Associate Professor Yasuhiro AOKI and Assistant Professor Takayuki YAMASHITA for their invaluable assistance and continuous encouragement throughout. I am especially grateful for Professor YAMASHITA's helpful, professional, and approachable nature, which created a supportive environment for learning and discussion.

I am thankful to Assistant Professor Abhishek SHARMA for his helpful nature and being a good friend at JWRI.

I sincerely thank the secretaries of the Fujii Laboratory for their invaluable administrative support.

I am also grateful to all the members of the Fujii Laboratory, including the staff, researchers, and all the amazing previous and present students, for their ongoing encouragement and assistance in my research. The students, in particular, made this journey smoother with their helpful spirit and cheerful nature.

Special thanks are due to the Ministry of Education, Culture, Sports, Science and Technology (MEXT) for awarding me the prestigious Super Global Research Fellowship, and to the Graduate School of Engineering at The University of Osaka for their generous and greatly appreciated financial support.

I would also like to express my sincere appreciation and deep respect to the Joining and Welding Research Institute's research facilities and technical staff division, especially Mr. MURAKAMI of TEM facility. This work would not have been possible without their unwavering support.

Finally, I would like to express my heartfelt gratitude to my beloved mother, Mrs. AFSAREE Bano, whose constant prayers, unconditional love, and unwavering emotional support have been my greatest strength.

I am equally grateful to my dear father, Mr. MUSHRRAF Ali, and my siblings for their endless encouragement, steadfast belief in me, and the warmth they have shared through every step of my academic journey.

Furkan
May 2025

Abstract

Dissimilar joining of steel and Al alloys is gaining interest in transportation industries, such as aerospace, shipbuilding, and automotive sectors, due to its potential for weight savings, improved performance, and cost efficiency. However, conventional fusion welding of steel and Al alloys faces challenges such as formation of hard and brittle intermetallic compounds (IMCs) at joint interface due to high heat input, along with risks of porosity and solidification cracking, which can negatively impact joint performance. To mitigate these challenges, solid-state welding technique is gaining attention which is capable of producing a joint below the melting point of parent materials and minimize IMCs formation.

Linear friction welding (LFW) is a solid-state joining process involving a part reciprocating back and forth in a linear manner under axial pressure against a stationary part, generating a plasticized layer at the joint interface. Much of this plasticized material is expelled as flash from the joint region, exposing fresh metal surfaces to make contact and forms a joint. The primary objective of this study is to overcome the inherent challenges associated with dissimilar material joining in conventional LFW and to develop novel LFW method that ensures sound dissimilar joining between steel and Al alloys with enhanced joint strength and improved fracture mode by promoting simultaneous interfacial deformation of mating material.

Direct LFW between mild steel (MS) and A7075 Al alloy was attempted and sound dissimilar joint was obtained by optimization of welding parameters. Under an applied pressure of 300 MPa, corresponding to the cross-point strength on temperature-strength curves of both alloys, the simultaneous interfacial deformation of both alloys was promoted during welding which leads to suppress the interfacial joint defects. An extremely thin IMC layer of ~34.7 nm thickness was identified at the dissimilar joining interface. As a result, the fabricated weld revealed excellent joint strength exhibiting 100% joint efficiency with respect to MS with a fracture in the base metal region of MS. To the best of author's knowledge, this is the first study to report 100 % joint efficiency between A7075 and any iron-based alloy dissimilar LFW joint and exhibiting a base metal fracture towards steel side.

Conventional direct LFW between SS400/A7075 alloy was difficult due to the absence of interfacial plastic deformation towards SS400 during welding, which led to several un-

jointed regions throughout the joint interface and eventually resulted in poor joint strength exhibiting an interfacial fracture. Therefore, center-driven double-sided (CDDS)-LFW was employed to effectively weld SS400 and A7075 Al alloy using MS as a center material. The interface temperatures were controlled by changing the applied pressures, corresponding to the different cross-point strengths at each interface, which facilitated simultaneous interfacial deformation of the mating materials at both MS/A7075 and MS/SS400 interfaces. Additionally, the obtained joint exhibited a superior tensile strength of ~347.5 MPa, revealing 100% joint efficiency concerning MS, and the fracture took place in the base metal region of MS, away from both the joint interface, i.e., SS400/MS and MS/A7075. However, the joint strength remained limited by the strength of the center material, i.e., MS base metal itself, indicating ongoing challenge to further improve the joint strength of SS400/A7075 dissimilar weld.

Further, a novel sacrificing-sheet linear friction welding (SSLFW) method, by oscillating a center sheet of SS400 steel utilizing the CDDS-LFW machine, was exploited to further enhance the joint strength of dissimilar weld between SS400 and A7075 Al alloy. In this novel method, by establishing a preheating stage that frictionally heats only SS400 side for a certain period of time, the center sheet was effectively expelled from the joint interface, and SSLFW that directly joins the SS400 and A7075 has been achieved. Unlike the CDDS-LFW method, where center material remains at the joint interface and becomes the weakest portion of the weld, SSLFW eliminates this dependency by expelling center sheet from joint interface and enabling direct joining between the side materials. Consequently, joints produced by exploiting SSLFW revealed the maximum joint strength of ~448 MPa after post-weld aging treatment. This indicates a significant improvement over the CDDS-LFW method for SS400/A7075 dissimilar joints, effectively overcoming its strength limitation of ~347.5 MPa.

Additionally, applicability of SSLFW method was further explored by applying it to more challenging material combination, i.e., S45C and A6061 Al alloy, which exhibit significant strength difference across all temperature ranges. The operating conditions of novel SSLFW were optimized by investigating the influence of key process parameters, i.e., preheat time, upset length and applied pressures, on mechanical properties and interfacial microstructure. The results indicated that defect-free, sound joint with high joint strength can be achieved using optimum welding parameters. Consequently, considerably high joint efficiency of 73% with respect to A6061 alloy was obtained after SSLFW, and it further increased to 96% subsequent post-weld aging treatment.

Table of contents

Chapter 1: Introduction

1.1. Overview and motivation of the study

Over the years, change in climate conditions has been one of the most significant concerns, as it affects the economic, social and environmental aspects of our lives. The increase in greenhouse gases (GHGs) in the atmosphere results from several human activities, contributing to a significant rise in the earth's temperature [1,2]. Among various GHGs, viz., CO_2, CH_4, N_2O, etc., the major influencing gas is CO_2, which is considered the major cause of global warming. Global warming is likely to reach 1.5℃ by 2050 if current CO_2 emissions levels continue [3]. The International Panel on Climate Change (IPCC) "1.5 °C Special Report" states that in order to keep the global average temperature increase below 1.5°C, carbon dioxide emissions must be reduced to net zero by around 2050 [4,5]. One of the most effective ways to suppress CO_2 emissions is the weight reduction of vehicles, and joining dissimilar materials has been accepted as one of the most representative methods for weight reduction. Therefore, the demand for dissimilar joints of steel and aluminum is rapidly increasing especially for transportation industries such as automotive, aerospace, aviation, railway, and shipbuilding for weight reduction, improved fuel efficiency, environmental concern, and energy and cost saving [6–11]. Therefore, steel and aluminum alloys are expected to represent the highly preferred dissimilar combination of engineering materials within the transportation sector [12,13]. In addition to their use in the transportation sector, steel and aluminum multi-material components are widely utilized in spherical pressure vessels composed of aluminum alloys/steel, ultra-high vacuum pressure equipment and specialized cooling systems [14,15]. Therefore, assembling lightweight structural parts, using materials such as steel and aluminum alloys, into functional assemblies has become of great importance for today's

society and industries. Although joining steel and aluminum alloys is essential for many structural applications, conventional methods such as mechanical fastening and adhesive bonding are often unsuitable due to increased component weight and stress concentrations near fastening areas [16]. Similarly, the fusion welding process poses challenges in dissimilar joining of these materials because of the formation of thick and brittle intermetallic compounds (IMCs) at the interface, which can negatively impact the joint performance [17]. Minimizing the thickness of interfacial IMCs is thus critical to enhancing joint strength and preventing brittle fracture. Linear friction welding (LFW), a solid-state welding technique, enables joining below the melting point of base materials, therefore effectively suppressing IMC formation and producing sound dissimilar joints [18]. However, poor weldability in many dissimilar friction-welded joints is often attributed to the lack of simultaneous interfacial deformation of parent materials, which can hinder effective expulsion of oxide and impurity from the joining area, leading to unbonded regions and weld defects [19]. In such cases, obtaining simultaneous interfacial deformation around the critical joint interface of dissimilar materials is essential to expel oxides and suppress the unjointed region, ensuring sound joining.

1.2. Thesis structure

Fig. 1-1 illustrates the flow of this study. In total, this thesis consists of 8 chapters, including the current one. The remaining chapters are as follows.

Chapter 2 presents a comprehensive literature review. An overview of friction welding methods is presented. Emphasis was placed on the dissimilar joining of steel and aluminum alloy using solid-state welding methods. Also, LFW method, process inputs, weld defects and effect of different process parameters are discussed based on past LFW studies. More importantly, the concept of controlling the welding temperature using LFW

and cross-point concept in dissimilar LFW is also elaborated.

Chapter 3 lists the test materials and describes the experimental procedure of metallographic and mechanical testing.

In Chapter 4, direct joining of A7075-T6/mild steel (MS) was conducted using conventional LFW method and a sound joint was obtained by optimizing the process parameters and minimizing the formation of interface IMC thickness. The mechanical properties, and interface macro and microstructure are investigated.

Chapter 5 reports the dissimilar joining of SS400 steel, and A7075-T6 aluminum alloy using MS as center material utilizing innovative center-driven double-sided linear friction welding (CDDS-LFW) method by exploiting cross-point concept. The applied pressure towards each interface, i.e., SS400/MS and MS/A7075-T6, was systematically selected based on the temperature dependence of materials' strengths. The microstructure evolution and mechanical properties were thoroughly investigated. Additionally, this chapter presents the challenges during conventional LFW of SS400/A7075-T6 from the viewpoint of joining temperature.

Chapter 6 proposes a novel joining method, called sacrificing-sheet linear friction welding (SSLFW), to fabricate sound dissimilar joint between steel and aluminum alloy. The efforts are invested to further improve the joint strength of SS400 steel and A7075. Differing from Chapter 5, in this chapter, center MS was replaced with a sheet of SS400 steel. The sound joining was accomplished by establishing a preheating stage during SSLFW. The joining mechanism is clarified, and mechanical properties and interface microstructure evolution are investigated.

Chapter 7 explores the SSLFW of S45C steel and A6061-T6 aluminum alloy, where there exists an extremely large difference in strength of two materials in a temperature

range from room temperature to melting point of A6061. The influence of applied pressure, upset length, and preheating time on joint's interfacial microstructure and mechanical properties is investigated. The SSLFW process is optimized and the obtained results are discussed.

Finally, a summary of the research main findings and recommendations for further research are presented in Chapter 8.

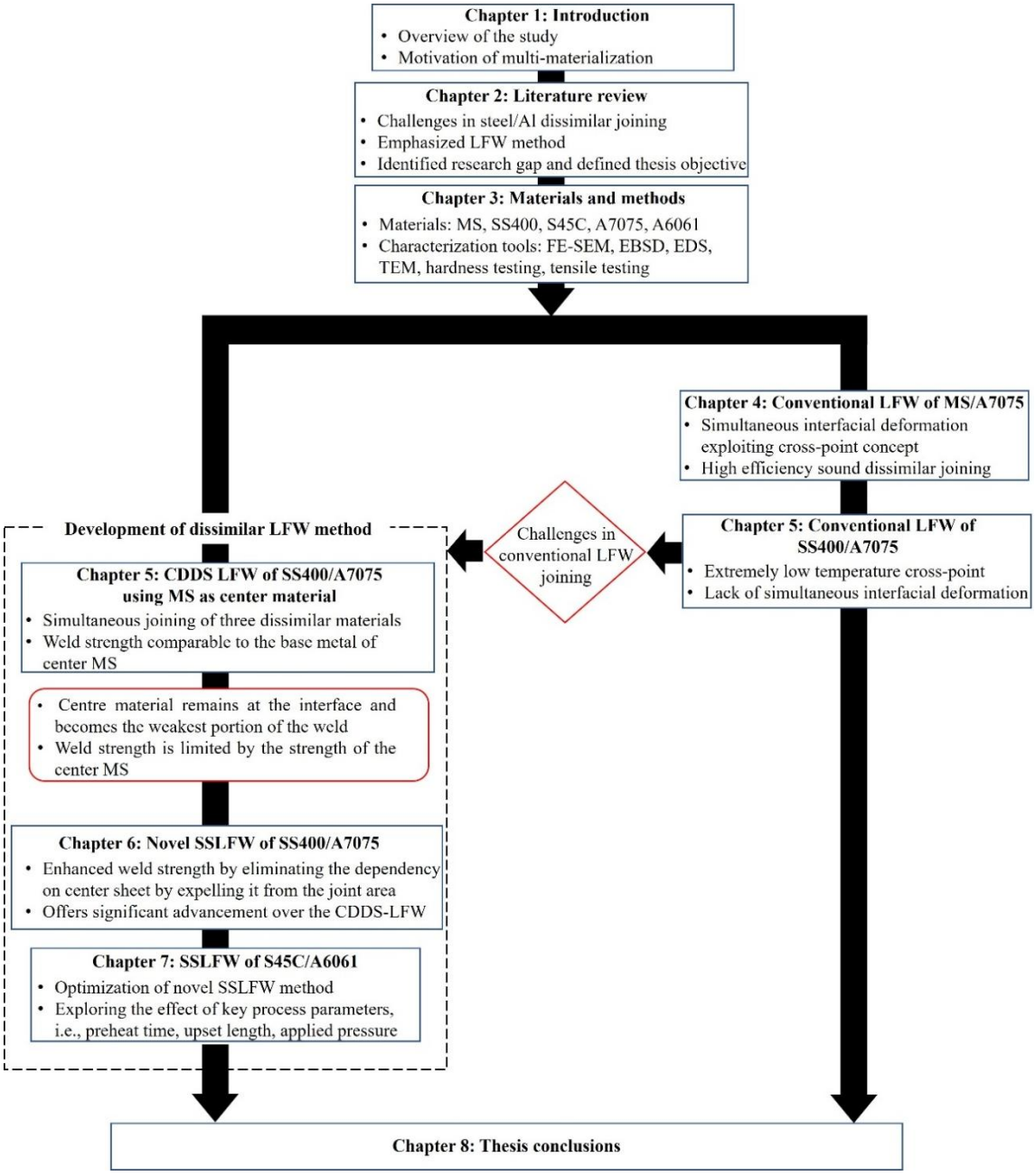

Fig. 1-1 Flowchart of the present study and research progression.

Chapter 2: Literature Review

2.1. Dissimilar joining of steel and Al alloy

The technological advancements in fabrication techniques in modern automotive and aerospace industries are driving the widespread application of dissimilar steel and aluminum joints to produce lightweight vehicles which can be a cornerstone of reducing greenhouse gas emissions from transportation sector. Lightweight structures with superior mechanical properties can be achieved by joining steel and Al-alloys [20]. In addition, Al and steel bimetallic plates are in high demand for a wide range of applications, including petrochemicals, desalination plants, power generation, and other industries where mechanical strength, corrosion resistance, and lightweight design are essential factors [21–23]. Therefore, assembling lightweight structural parts into functional assemblies and obtaining a sound dissimilar joint between steel and Al alloy has become of great importance for today's society and industries. Although the joining of steel and aluminum alloys is highly desirable; however, achieving a sound joint between these materials using conventional fusion welding processes presents significant challenges. The primary issues with conventional fusion welding of aluminum alloy and steel include the formation of hard and brittle IMCs at the joint interface due to high weld heat input [24–28]. Moreover, the melting of the parent materials in fusion welding strategies also leads to the risks of porosity and solidification cracking [29,30]. Dong et al. [31] investigated the fusion-brazing of 5A02 aluminum alloy and Q235 carbon steel and observed very thick IMCs of 15 μm at the joint interface. Yang et al. [32] examined the control of interfacial layer uniformity to butt weld 301 stainless steel and A6061-T6 aluminum using laser-metal inert gas hybrid welding-brazing. Nevertheless, a thick IMC layer (~5.2 μm) was

identified at the weld interface, and the weld fractured within the IMC layer. Zhang et al.[17] welded 1Cr18Ni9Ti stainless steel to 2B50 aluminum alloy, revealing that excessive IMCs severely deteriorated the joining efficiency. These studies demonstrate that the formation of excessive IMCs during the fusion joining processes leads to relatively low joint efficiency, suggesting that the joining should be conducted at low temperatures below the melting point of parent metals to prevent the growth of the IMCs layer. Although adhesive bonding and mechanical fastening also provide alternatives to fusion welding, the operating service conditions and cost may limit the application of these processes. Adhesive bonding, for instance, is unsuitable for high-temperature applications and harsh conditions. Similarly, mechanical fastening, such as bolting or riveting, adds additional weight and often introduces stress concentrations [16,33], making it impractical for applications demanding lightweight structures, such as in aerospace and automotive engineering. Consequently, solid-state welding emerges as a superior technique for joining dissimilar materials while maintaining structural integrity, mechanical performance, and durability in demanding operational environments with reasonable cost. Therefore, to achieve sound dissimilar joining between steel and Al alloys, and to suppress the formation of brittle IMCs and reduce weld heat input, researchers have increasingly turned to solid-state welding methods which can fabricate a joint below the melting point of parent materials [34–39]. Saleh et al. [40] utilized friction stir welding (FSW) method to weld mild steel with A7075-T651 Al alloy, effectively controlled the growth of interfacial IMCs by increasing the welding speed. As a result, 100% joint efficiency with a steel base metal fracture was obtained. Tanaka et al. [41] investigated the relationship between thickness of IMC layer and joint strength in dissimilar FSW of mild steel with various aluminum alloys including A7075-T6 Al alloy, finding that joint strength

improved significantly with the reduction of IMC thickness. Kimura et al. [42] investigated the rotary friction welding of stainless steel and aluminum alloy and obtained a joint without IMC formation at the joint interface. Therefore, these studies revealed that solid-state welding techniques, which are explained in next section 2.2, are capable of producing sound and highly efficient joints between steel and Al alloys with reduced heat input and minimized IMC formation at the dissimilar joint interface of steel and Al alloy.

2.2. Overview of solid-state welding methods

Solid-state welding is a joining process in which two or more workpieces are joined without the presence of a liquid or vapor phase. This process may or may not involve an externally applied load to ensure intimate contact between the faying surfaces, facilitating atomic diffusion and metallurgical bonding [43]. One of the key advantages of solid-state welding is its ability to join metals at temperatures below their respective melting points, thereby mitigating several issues inherent to fusion-based welding methods. These include the formation of brittle (IMCs), segregation of alloying elements, and thermally induced distortions, all of which can adversely affect the mechanical integrity of the joint. The several solid-state welding methods are summarized below:

I. Friction Stir Welding

Friction Stir Welding (FSW) is a solid-state welding method that utilizes frictional heat between the non-consumable rotating tool and parent material to facilitate the material joining. The process was first developed in 1991 at The Welding Institute (TWI), Cambridge, U.K. and has since been widely adopted for welding temperature-sensitive and dissimilar materials. FSW operates using a non-consumable rotating tool that is plunged into the joint interface between two workpieces. As the tool traverses along

the interface, frictional heat and plastic deformation elevate the material temperature, softening it without reaching the melting point. The rotating tool then mechanically mixes the softened material of the two workpieces [40,44,45], as shown in Figure 2-1.

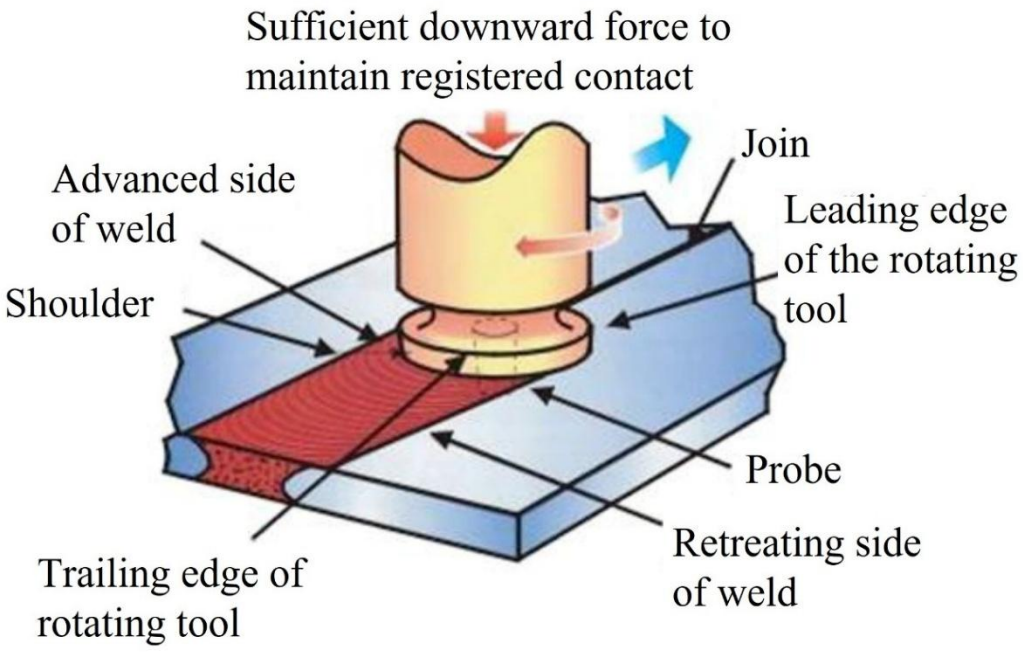

Fig. 2-1 Schematic illustration of friction stir welding process [45].

II. Friction Stir Spot Welding

Friction Stir Spot Welding (FSSW) is a variant of FSW that was jointly developed by Mazda Motor Corporation and Kawasaki Heavy Industries**.** Unlike conventional FSW, where the non-consumable tool moves along the joint line, FSSW does not involve any traverse motion. Instead, the rotating tool is plunged into the overlapping workpieces, generating frictional heat that softens the material and enables localized stirring. This results in the formation of a lap joint, as illustrated in Figure 2-2[46,47].

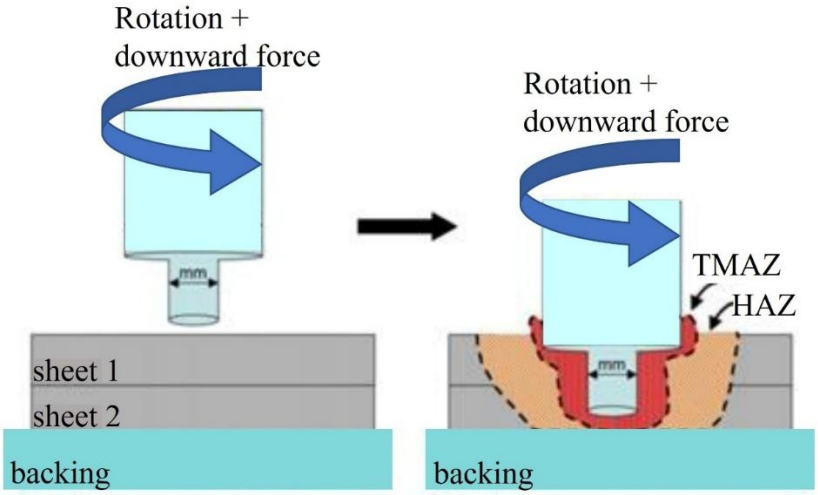

Fig. 2-2 Schematic drawing of friction stir spot welding process [46].

III. Rotary Friction Welding

Rotary Friction Welding (RFW) has been widely utilized in industrial applications since the 1940s. The process involves rotating one cylindrical workpiece about its axis while applying a normal axial force against a stationary counterpart. This combination of rotational motion and compressive force generates frictional heat at the interface, causing localized plasticization of the material which is expelled from the joint eventually. Once free from contaminants, metal-to-metal diffusion occurs resulting in a solid-state joint formation. Due to its operational mechanics, RFW is only applicable to rotationally symmetrical workpieces [42,48,49], as illustrated in Figure 2-3.

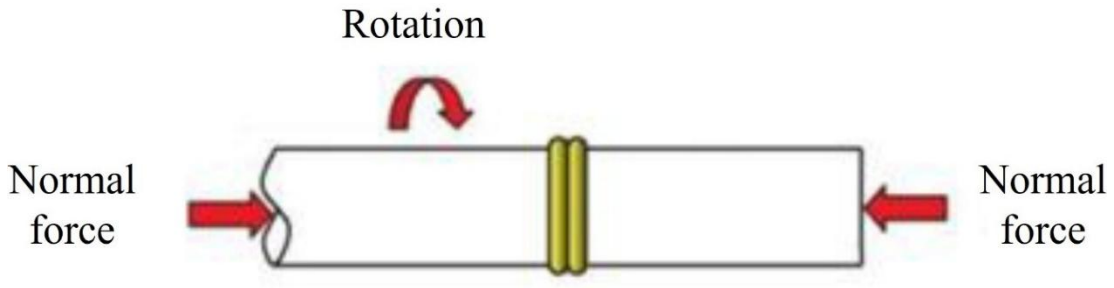

Fig. 2-3 Rotary friction welding process [48].

IV. Orbital Friction Welding

Orbital Friction Welding (OFW) was developed in the 1970s to address the limitations of rotary friction welding, particularly its restriction to rotationally symmetrical workpieces [50]. Unlike RFW, which relies on continuous rotational motion, OFW utilizes an orbital motion**,** enabling the joining of non-circular components. The fundamental principle remains the same, frictional heat is generated at the interface through relative motion between the workpieces, leading to localized plasticization. Once contaminants and oxides are expelled, solid-state joining occurs under axial pressure. An illustration of the process is provided in Figure 2-4.

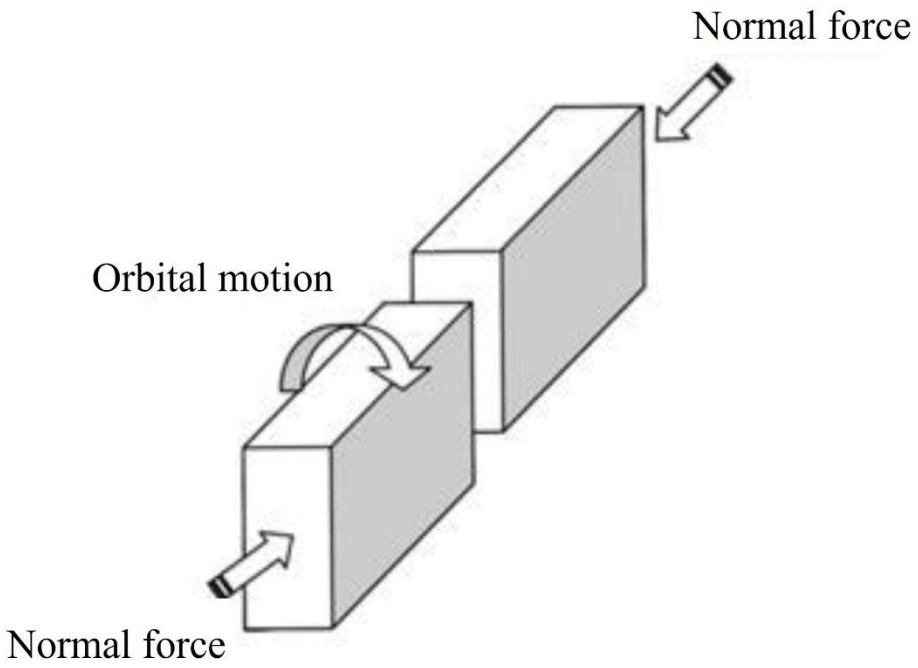

Fig. 2-4 Schematic illustration of orbital friction welding process [48].

2.3. Linear Friction Welding

2.3.1. Background and joining principle of LFW

Linear Friction Welding (LFW) is a solid-state joining method involving a part

reciprocating back and forth in a linear manner under axial applied pressure while another part remains stationary. The friction between the parts generates heat, which, combined with the axial applied pressure, leads to the formation of a plasticized layer at the joint interface as shown in Fig. 2-5. Much of this plasticized material is expelled from the joint region due to the applied pressure and part movement, generating the so-called flash [18]. As a result, the newly exposed metal surfaces make contact and forms a joint. The first patent of LFW process was applied in 1929 by Richter [51]. Although this patent was associated with a vague description, the patent tailored for LFW equipment was officially licensed in 1969 [52]. Following the manufacturing of specialized LFW equipment at The Welding Institute (TWI) in the early 1980s, the development of the LFW technique advanced primarily with a focus on its application in aerospace, particularly with high-temperature strength materials such as titanium and nickel alloys [53–56].

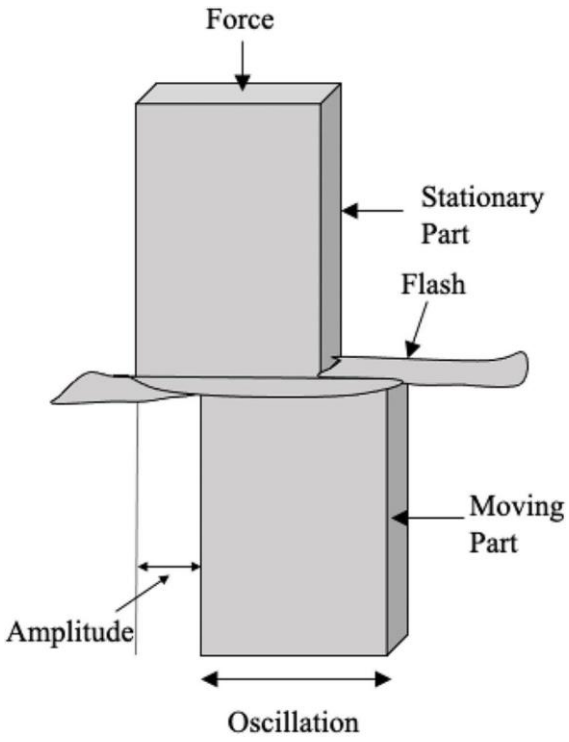

Fig. 2-5 Schematic illustration of linear friction welding method [57].

2.3.2. LFW process phases and input parameters

As discussed in Section 2.3.1, linear friction welding is a solid-state welding process that operates by inducing linear reciprocating oscillation in one workpiece relative to another mating part under a significant compressive force. Although LFW is a single step continuous process, it is typically described as occurring in four distinct phases as follows, which are schematically illustrated in Fig. 2-6 [58–60]:

Phase I: Initial contact phase

In this stage, firstly, a contact is established between the mating workpieces at the interface. Following the contact, the relative reciprocating motion is provided to one mating part with respect to the other under axial applied pressure. Consequently, frictional heat is generated at the weld interface.

Phase II: Transition phase

During the transition phase**,** the material at the weld interface experiences significant softening due to the increased interface temperature caused by frictional heat in phase I. As the temperature increases, the material reaches a plasticized state**,** reducing its resistance to deformation, and when the softened material can no longer sustain the applied compressive force**,** it begins to be expelled outward in the form of flash or burr formation.

Phase III: Equilibrium phase

As heat continues to accumulate, the interface material becomes plasticized, and excessive material is expelled in the form of flash in phase II. The workpieces shorten along the axial direction due to this material loss. During the equilibrium phase, the temperature stabilizes, and uniform plastic deformation occurs at the interface, ensuring proper material mixing and diffusion of atoms between the workpieces.

Phase IV: Deceleration or forge phase

Once sufficient plasticization at the interface has achieved, oscillation is stopped and the workpieces are aligned while a high axial compressive force is maintained or further increased to allow solid state joining followed by cooling to room temperature.

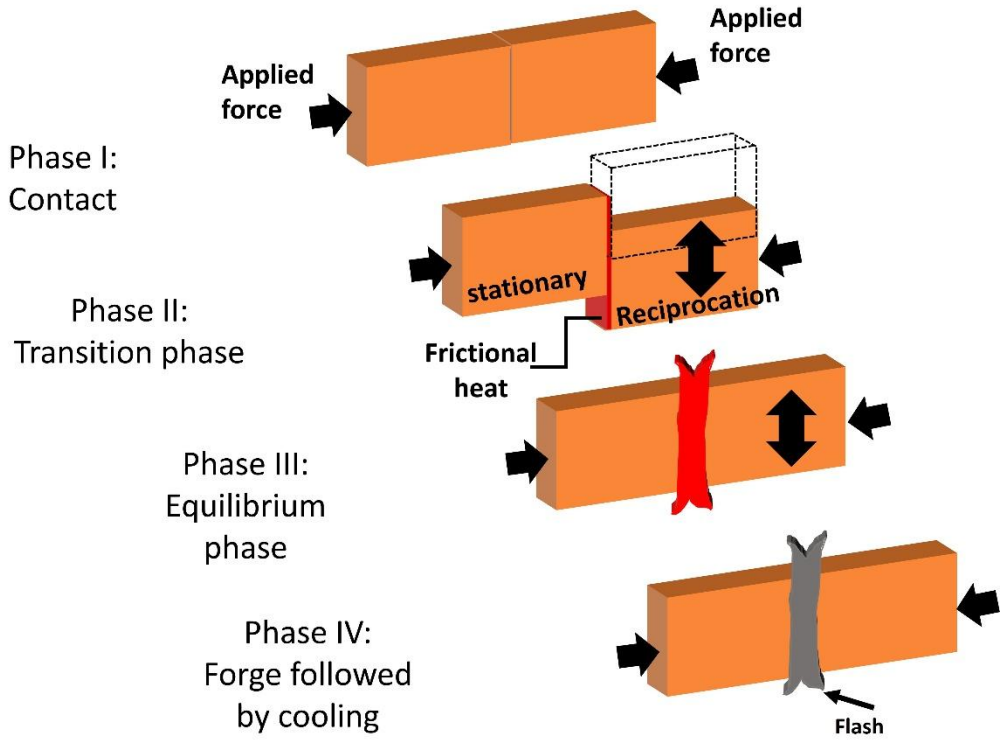

Fig. 2-6 Schematic illustration of various LFW process phases [60].

Process parameters

The important process parameters that affect the weld strength during LFW method are as follows**:**

Linear oscillation frequency: The number of completed oscillatory cycles per second. Typical values are used between 15 Hz and 75 Hz.

Linear oscillation amplitude: The maximum displacement of the oscillating workpiece from its datum point.

Applied pressure: The normal axial force applied to the workpiece during the process.

Ramp-up time: The time taken to ramp-up the oscillation amplitude to the desired value. The Ramp-up time is typically less than a second.

Linear oscillation decay time: Time taken to decay the amplitude and frequency from the processing value to zero.

Total upset: This is the combination of the burn-off distance plus any extra shortening achieved during the forging phase.

2.3.3. Weld features

Figs. 2-7a and b show the appearance of LFW weld of Titanium alloy [55] and nickel-based super alloy [61], respectively. Typically, the weld region is surrounded by the flash in the direction of and perpendicular to the direction of oscillation, which is parallel to the specimen width, Fig. 2-7a. The flash layer consisted of plastically deformed material extruded from the joint interface during the welding process as a result of applied pressure and linear oscillatory motion [62–64].

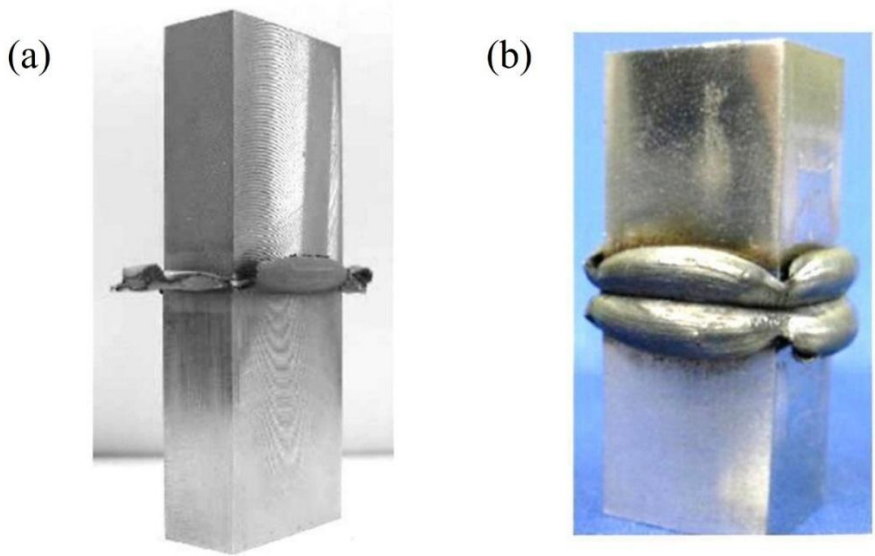

Fig. 2-7 Flash morphology for: (a) Titanium alloy (Ti-6Al-4V) [55] and (b) a Nickel based super alloy (waspaloy) [61].

Additionally, Fig. 2-8 presents the typical weld zone in a Ti-6Al-4V linear friction welded sample. LFW welds have several distinct zones including a weld center zone (WCZ), thermomechanical affected zone (TMAZ), and the parent metal (PM) as reported by Wanjara and Jahazi [55]. The WCZ experiences significant dynamic recrystallization (DRX), where the amounts of heat and plastic strain are the greatest among other regions. The transition zone between the WCZ and PM is called the TMAZ. TMAZ experiences both temperature and plastic deformation during the LFW process. Wanjara et al. [55] found Widmanstätten structures inside highly refined prior-beta grains in the WCZ of Ti-6Al-4V alloy, while elongated α grains with broken particles of intergranular or inter-lamellar β could be observed in the TMAZ as shown in Fig. 2-8b. Vairis et al. [53] investigated linear friction welding of Ti-6Al-4V alloy and determined that the success of the LFW joint is influenced by key parameters, including applied pressure, oscillation frequency, and oscillation amplitude. Additionally, they emphasized that effective flash expulsion is essential for achieving a high-quality joint [53,58]. Further studies on LFW of Ti-6Al-4V, conducted at pressures ranging from 50 to 90 MPa, confirmed the formation of a Widmanstätten microstructure with a refined β-phase in the thermo-mechanically affected zone (TMAZ) of the joint [65]. Choi et al. [66] further examined LFW of Ti-6Al-4V alloy and observed that an increase in applied pressure led to a reduction in joining temperature and successfully achieved low-temperature welding below the β-phase transformation temperature by applying a high pressure of 550 MPa. The resulting joints exhibited ultrafine equiaxed α-grains, with an absence of β-phase, Widmanstätten structure, or softened regions in the TMAZ. These microstructural characteristics suggested that the joints possessed enhanced ductility, toughness and fatigue property [66–68].

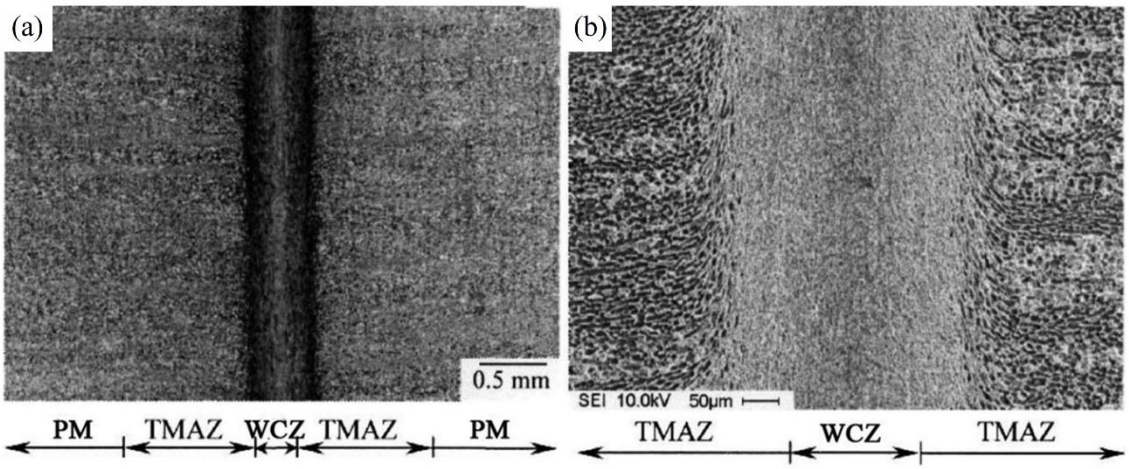

Fig. 2-8 (a) Optical and (b) scanning electron microscope images of a typical weld zone in a Ti-6Al-4V linear friction welded sample [55].

2.3.4. Weld defects

The appropriate welding conditions are necessary for the sufficient and continuous deformation of interface material. The lack of appropriate deformation leads to several weld defects at the interface such as residual oxides, micro-voids etc. as shown in Fig. 2-9a and b in a LFWed Ti-6Al-4V joint [55,69]. Contaminants at the interface, such as oxides and foreign particles, can significantly affect the joint properties of the joint [55,61]. These impurities are also known to reduce the service life of the weld [63], making them a key cause of defects in linear friction welding [48,70]. It is possible that oxides may remain at the interface due to insufficient plastic deformation at the joint interface. The occurrence of un-jointed regions is also possible at the joint interface due to inhomogeneous deformation of materials at the interface during LFW [71]. Addison [72] noticed that fine features of linear friction welds, such as the corners of the workpieces, can contain a small unbonded region; see Fig. 2-9c. Insufficient bonding at the interface may result in welds having poorer mechanical properties. McAndrew et al. [73], using finite element analysis (FEA), showed that the unbonded region at the corners is noticeable at low burn-off values. The unbonded regions can be eliminated with a burn-off increase. According to

McAndrew et al. [74], as the burn-off increases, the heat from the flash and interface conducts into the corners, causing them to soften and plastically deform. This results in the corner material merging with the rest of the interface, forming a joint at the corner and eliminating a potential source of inferior mechanical properties. Apart from this, several researchers suggest that a weld is likely to be free from contaminants if all of the initial contacting interface material is expelled into the flash [55,61,70]. McAndrew et al. [75] and Turner et al. [63] showed that the interface contaminants are increasingly expelled into the flash as the burn-off is increased, as shown in Fig. 2-10. According to Bhamji et al. [70], it is important that the contaminants are expelled from the interface into the flash, as this allows full metal-to-metal material mixing and a sound joint to be formed. Additionally, it is reported that for the same burn-off, contaminants were present [55] at the interface if lower values of frequency and amplitude were used, whereas if higher values were used, the interface was typically free from contaminants. Therefore, interface contaminant removal appears to be critically dependent on the combination of process inputs used as shown in Fig 2-10 b,c,d.

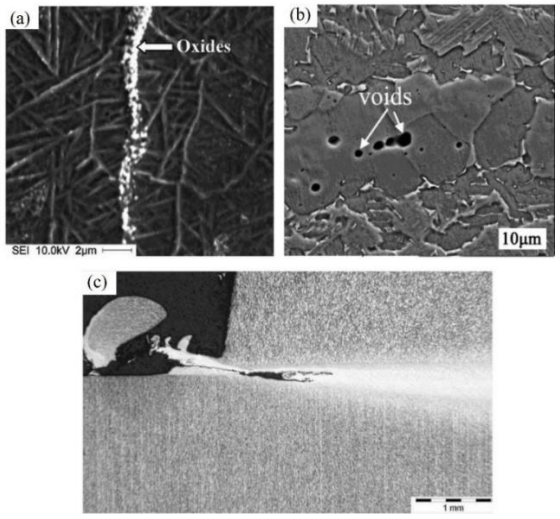

Fig. 2-9 Linear friction weld defects; (a) oxides at the interface of a Ti-6Al-4V weld [55], (b) voids observed in linear friction welds [69], (c) weld interface corner of an experimental 'T' joint linear friction weld showing an unbonded region [72].

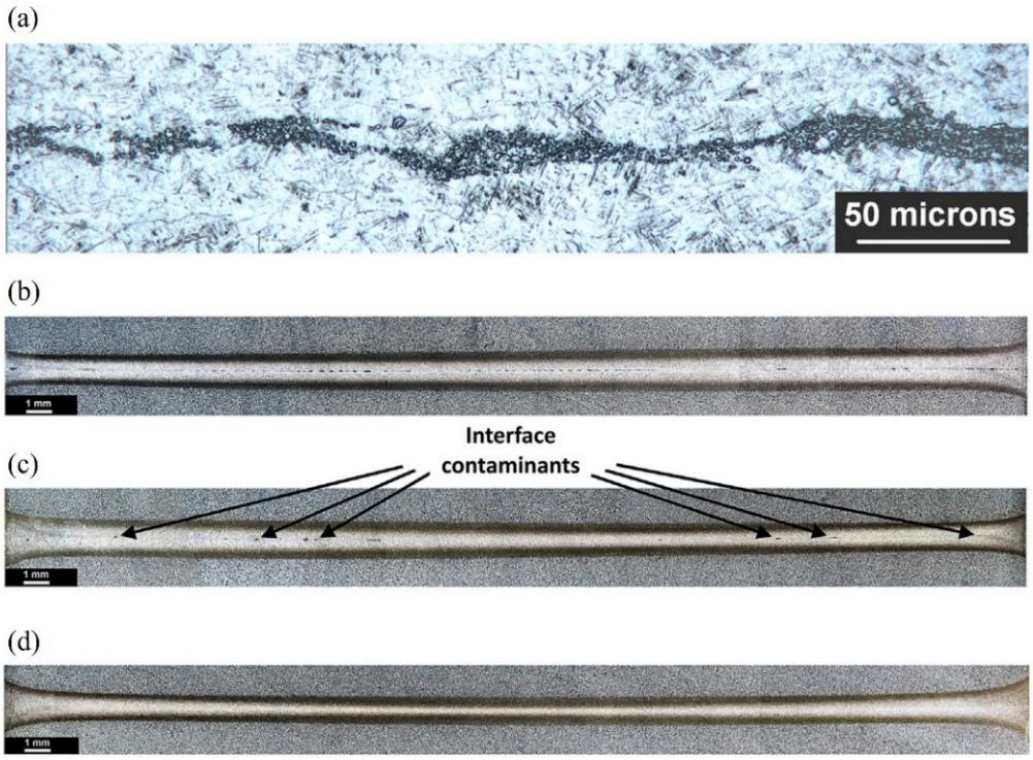

Fig. 2-10 (a) High magnification of the contaminants presents at the weld interface of a Ti-6Al-4V weld, (b) contaminants after 0.5 mm of burn-off, (c) contaminants being expelled toward the edges after 1 mm of burn-off, and (d) no contaminants after 3 mm of burn-off [75].

2.3.5. Advantages of LFW and its industrial applications

The LFW process has been commercially established as a key technology for the fabrication of titanium alloy integrated bladed disks (blisks) in aero-engine applications [70,72,76]. The aerospace industry has increasingly adopted blisk structures, which integrate blades and disks into a single component. Fig. 2-11a shows an example of a blisk manufactured using the LFW process. LFW offers many advantages when manufacturing blisks, for example, conventionally manufactured bladed disk assemblies are reliant on mechanical fixings and dovetail joints to join the blade to the disk, as shown in Fig. 2-11b. LFW allows for the blade to be integrally joined to the disk which significantly reduces the weight of the component [74,77,78] even by as much as 30% [77,78] ; see Fig. 2-11c. In addition to the weight savings, the lack of a mechanical interface between the blades

and the disks eliminates common sources for fretting fatigue crack initiation [78,79], which is often the life-limiting feature of these parts [78]. This may result in extended inspection intervals [79]. Furthermore, linear friction welded blisks also have improved performance (e.g., better aerodynamics), which reduces the operating costs for the end user [63,80,81]. Another alternative to using mechanical fixings is to machine the blisk from a solid forged block. When compared to the LFW process this is a costly exercise due to the amount of waste material generated, particularly for larger blisks [63,79]. Blisks machined from a solid block must comprise of a single material [78]. Therefore, LFW has another advantage of joining disks and blades using different materials. Furthermore, LFW process possesses numerous appealing features such as no welding tool is required for the joining of materials. This characteristic is very useful for the welding of high-melting point materials such as steel, while the wide applicability of friction stir welding (FSW) is still limited by the tool durability for these materials. Extremely short welding time of less than 1 s, as the weld can be achieved within a fraction of second [71], it could be very beneficial to manufacturing industries for mass production and cost saving. The ability to achieve high reproducibility with high-dimensional accuracy of the joint. Furthermore, while the industrial applicability of conventional rotary friction welding is still limited to round-shaped specimens, LFW is adaptable for use with non-axially symmetrical objects as well. Besides, LFW is a self-cleaning welding process [82]. All the process impurities or oxides which could be present at the weld interface are expelled with the generated flash outside the weld interface. Thus, the preparation of the welding joint is minimal, and LFW can be done in open air, and no shielding gas is required. Therefore, LFW stands out as a highly automatable and consistently repeatable process. This is attributed to its sole reliance on a mechanical heat source, ensuring that all energy input is meticulously

controlled through motion and loads. Certainly, through the welding of near-net-shape parts, LFW enables significant mass savings, a decrease in machining costs, and consequently, substantial overall cost savings. In addition, since the joining temperature can be easily controlled by the applied pressure as described in the next section, apart from similar materials joining, LFW is also considered suitable for joining dissimilar materials such as steel and Al alloys that require joining at low temperatures.

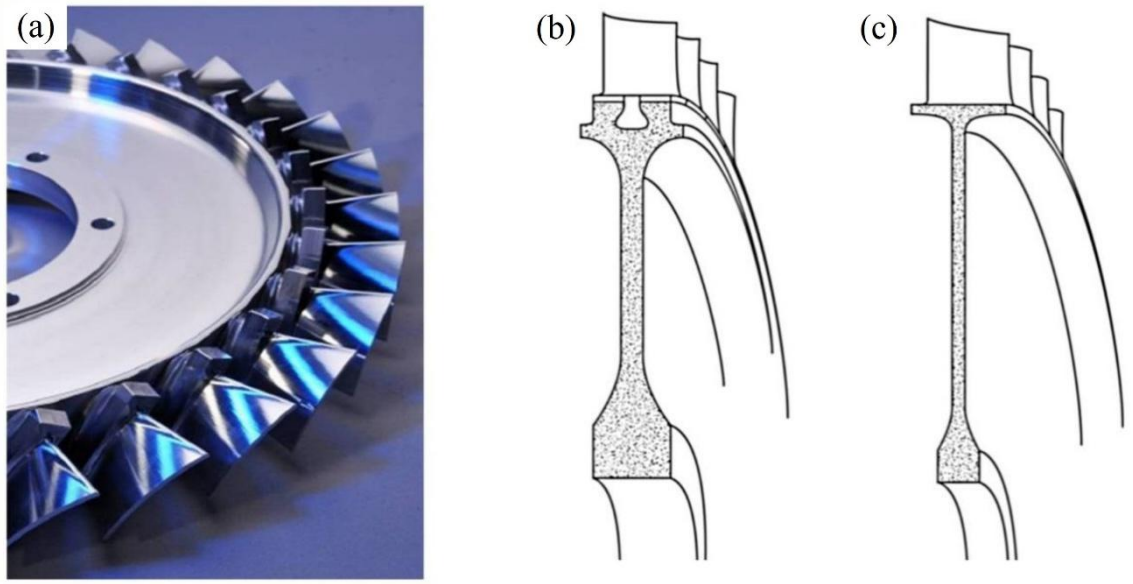

Fig. 2-11 (a) an integrated bladed disk (blisk) manufactured at TWI [83] (b) a conventional bladed disk assembly [63] and (c) a linear friction welded blisk [63].

2.3.6. LFW of Steels

In addition to the more commonly studied aircraft materials, such as titanium alloys and nickel-based superalloys, recent studies have expanded the application of LFW to steel materials [84–92]. Among steel materials, significant research has focused on medium and high carbon steels. Carbon steel finds extensive applications in the automobiles, tools, and dies [84,85,93]. These steels show a great potential to be used as the mainstream structural materials for abundant industrial fields such as railroad and construction industries with

less consumptions on rich metal resources and lower costs on raw materials and steel-making processes. However, the widespread industrial application of carbon steels is significantly hindered by their limited weldability [94,95]. When these steels are welded to form large and complex components using conventional fusion welding techniques the thermal cycles involving cooling process from elevated temperatures (above the phase transformation temperature, A_1) to ambient conditions facilitate the brittle martensitic transformation within the weld zone. This might cause a direct cracking in the welds immediately after welding [95], consequently leading to the deterioration of the joint's mechanical properties. Therefore, solid-state joining methods, which could provide a welding temperature lower than the melting point, even below A_1 point, of parent materials, are strongly demanded for achieving highly reliable welding on carbon steels. The potential to fabricate joints with superior microstructural features through LFW could significantly broaden the range of applications for medium and high carbon steels. For instance, Ma and Li [84,85] investigated the LFW of medium carbon steel S45C, which was martensite-treated by quenching prior to LFW, and analyzed the effect of friction time on flash shape, microstructural evolution, and mechanical properties. Reportedly, a friction time of 3 seconds resulted in a sound LFW joint with superfine ferrite and pearlite structure in the weld center leading to substantial improvements in both strength and ductility when compared to quenched and tempered steel. Fig. 2-12a and b show the appearance of LFW joints fabricated at different friction time of 1.5s and 3.0s, respectively. Evidently, it was confirmed that with increased friction time, the amount of flash was significantly increased.

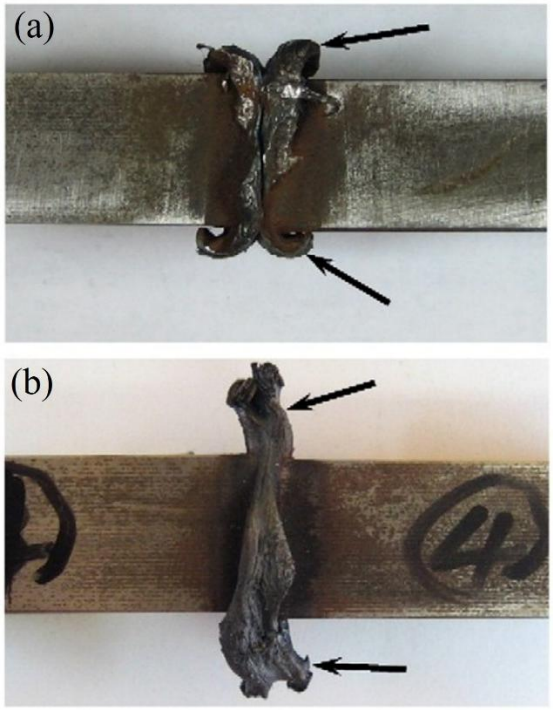

Fig. 2-12 Appearance of linear friction welded S45C steel fabricated under different friction times of (a) 1.5s, and (b) 3s [84].

The weld flash also plays an important role in the fatigue life of LFWed steel joints [90]. Low carbon steel welded by LFW has also shown excellent stress-controlled fatigue results without removing flash, wherein the joints with higher post-oscillation pressure exhibited a higher fatigue life in comparison to the welds with smaller applied pressure [96]. The applied pressure alters the weld toe shape, which affects the crack propagation under cyclic loading. On the other hand, Miao et al. [97], explores the application of low carbon steel LFW in T-joint configuration (as shown in Fig. 2-13) to investigate the effect of welding parameters and achieved a sound joint revealing 100 % joint efficiency across all weld conditions with ductile fracture. LFW was performed using two different configurations. In one configuration, the long side of the rib was parallel to the oscillation direction referred to as long-side oscillation (Fig. 2-13b) and in the other, the long side of the rib was perpendicular to the oscillation direction referred to as short-side oscillation

(Fig. 2-13c). The flash was uniformly ejected on the side perpendicular to the oscillation direction, whereas it was unevenly ejected on the parallel side due to oscillation-induced material flow variations. Since the flash ejection was more homogeneous in the short-side oscillation, see Fig. 2-13c, than in the long-side oscillation in Fig.2-13b, it is suggested that short-side oscillation is more favorable for producing sound LFWed T-joints.

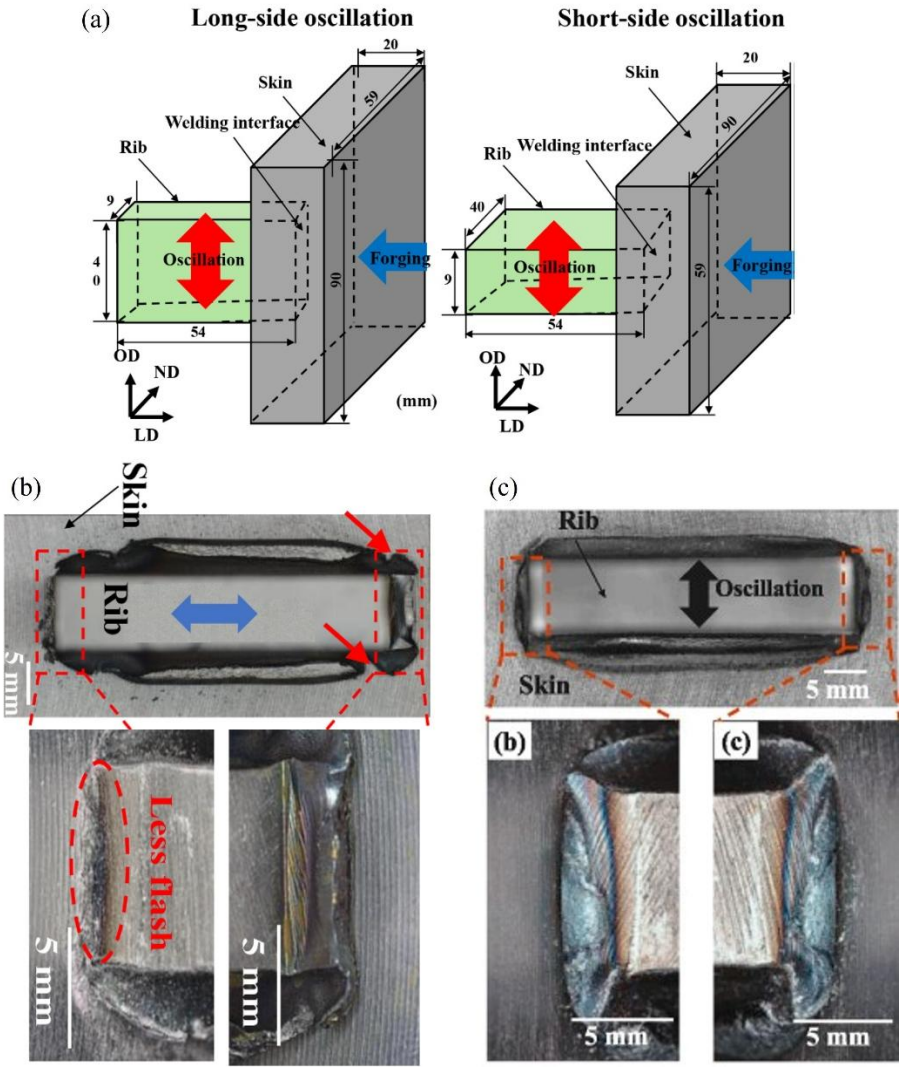

Fig. 2-13 (a) Schematic of LFW process showing two different oscillation methods, and weld toe and flash ejection images of LFWed T-joints for the (b) long-side oscillation method, (c) short-side oscillation method [97].

In addition to experimental studies, several numerical analysis investigations have been conducted on the LFW of medium carbon steel [86–88]. Recently, Shotri et al. [98] developed numerical model for simulating LFW process. They performed numerical and experimental analysis on S45C steel, and successfully achieved a sound joint under controlled interfacial deformation during LFW by integrating experiment and calculation. Apart from this, LFW has been proven capable of joining weathering steels [89,90] and austenitic stainless steels [18,57,99]. Weathering steels are specifically designed with a high phosphorus content to enhance corrosion resistance. However, during conventional fusion welding processes, phosphorus tends to segregate, leading to solidification cracking, which significantly degrades joint properties. Since LFW operates below the melting point, it effectively minimizes phosphorus segregation, thereby mitigating solidification cracking and improving weld integrity. Shimizu et al.[100] analyzed the significance of fracture toughness of linear friction welded joint of SPA-H weathering steel below A_1 and above A_3 transformation temperature. The fracture toughness of both joints, where a crack was located at the joint interface, exhibited a higher value than that of the heat-affected zone of MAG (metal active gas) welds for the same steel. These results indicated that the LFW was more effective for the joining of weathering steel compared with conventional arc welding in terms of fracture toughness. Wang et al.[89] conducted LFW on high-phosphorus weathering steels SMA490AW and SPA-H, evaluating the resulting microstructure, mechanical properties, and fatigue behavior of the welded joints. The fabricated joints demonstrated fatigue and tensile strengths comparable to those of the base material, revealing ductile fracture through base metal with the presence of bainite in the weld region of both materials. As for the LFWed austenitic stainless steel (AISI316L) [18] fine grains were observed in a large thickness area close to the weld line

as shown in Fig. 2-14a. A considerable amount of δ-ferrite was appeared close to the weld line. The amount of δ-ferrite was also inversely proportional to the burn-off rate. These findings highlight the potential of LFW for producing high-quality, defect-free joints in weathering steels and austenitic stainless steel as well, expanding their applicability in structural and engineering applications. The LFW of steels is expected to have a much wider industrial impact in the upcoming years due to its various advantages over fusion welding techniques and steel's long dominating usage in the manufacturing sectors.

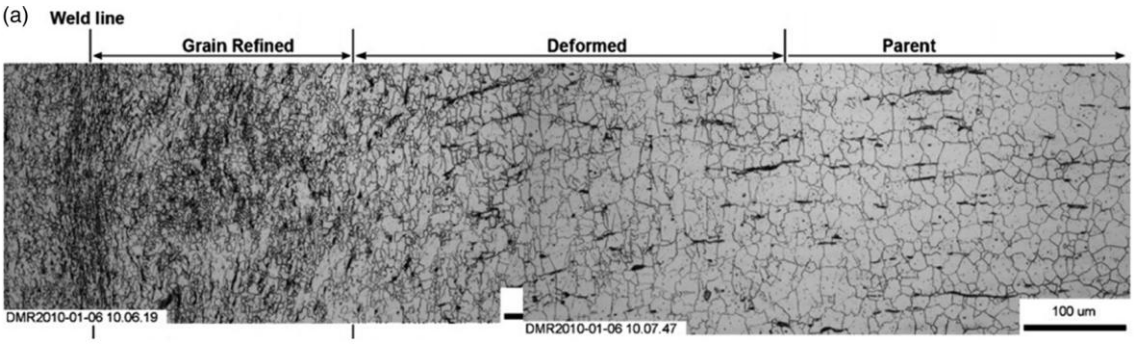

Fig. 2-14 (a) Typical microstructure of a LFWed 316L joint in the as-welded state [18].

2.3.7. Effect of process parameters on LFW joints

The fundamental parameters in LFW include linear oscillation frequency (f), oscillation amplitude (A), upset, and applied pressure (P), which is the axial normal force exerted during the process. Each of these parameters influences the amount of frictional heat generation (q), as expressed by the following equation [18]:

$$q = V_t \times \mu P = 2\pi f A \cos(2\pi f t) \times \mu P \qquad (1)$$

Where V_t represents the oscillation velocity, t is the welding time, and μ denotes the friction coefficient.

One of the key characteristics of LFW is the relationship between applied pressure and joining temperature. It has been observed that an increase in applied pressure leads to a decrease in the joining temperature [66,67,101,102]. Fig. 2-15 illustrates the relationship between applied pressure and interface temperature for Ti-6Al-4V alloy during LFW [66].

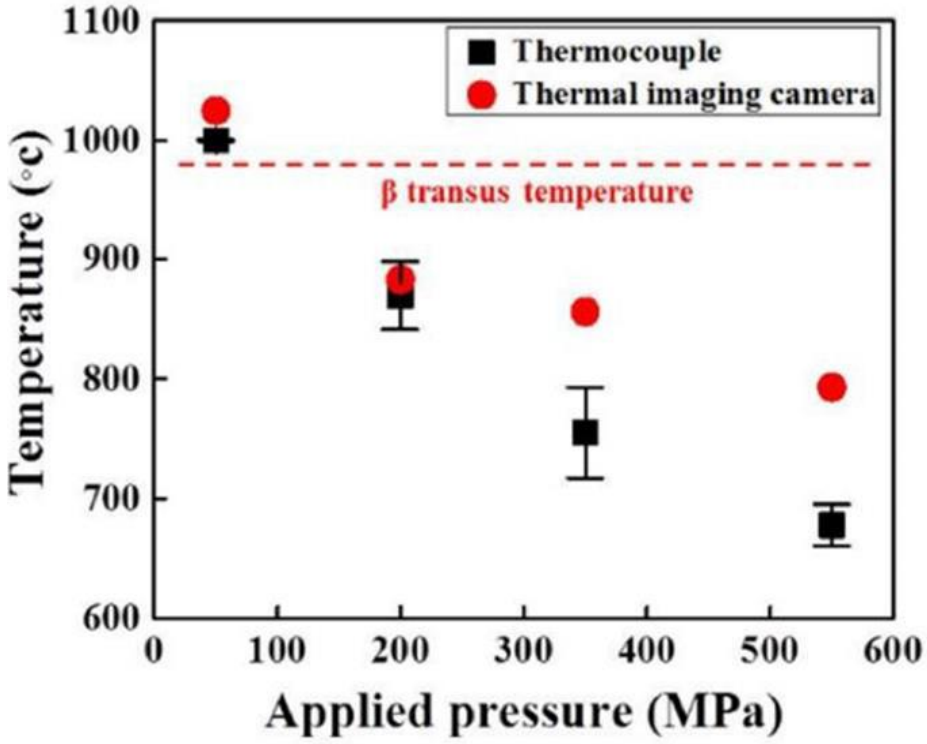

Fig. 2-15 Relationship between applied pressure and welding temperature in LFW of Ti-6Al-4V[66].

showing a decrease in welding temperature with the increase of applied pressure. Further microstructural development during LFW of titanium alloys has also shown that the acicular α structure changed to the ultra-fine α structure at high applied pressures, which has been interpreted as a reduction in the peak welding temperature during LFW. This decrease in temperature was attributed to a large amount of flash expulsion at high pressures, which caused large heat rejection and short welding times [103]. The fact that the welding temperature decreases when using higher applied pressures is also reported by

Romero et al. [104]. However, based on Equation (1), it is expected that an increase in applied pressure *(P)* would result in a higher heat input, leading to a rise in joining temperature. However, experimental observations indicated the opposite trend, where the joining temperature decreases with increasing applied pressure. This phenomenon can be attributed to the expulsion of hot material in the form of flash at relatively low temperature under an increased applied pressure, which significantly reduces heat generation caused by the significant decrease in $\mu(T)$ in Equation (1) due to interface temperature rise [98] and dissipates heat away from the weld interface. As depicted in Fig. 2-6, during LFW, the frictional heat input raises the interface temperature, reducing the deformation resistance of the base material. Once the deformation resistance falls below the applied pressure, material near the weld interface is expelled as flash. This expelled flash no longer undergoes frictional heating and subsequently cools. Once flash formation begins, fresh heated material surface, whose deformation resistance has also dropped below the applied pressure, continues to be expelled as high-temperature flash. Consequently, the interface temperature stabilizes at a relatively constant value. Therefore, when welding is performed under high applied pressure, flash formation initiates at a lower temperature. Explicitly, the material is expelled while the interface still exhibits relatively high deformation resistance. In other words, as the applied pressure increases, the interface temperature during welding; referred to as the joining temperature; remains lower. This principle explains how the joining temperature in LFW is controlled by the applied pressure.

Fig. 2-16 presents the change in the temperature and the corresponding LFW parameters versus time, including the applied pressure and the upset based on the experimental data [101]. The upset evolution can be divided into three stages, as illustrated

in Fig. 2-16. In stage 1, the upset shows almost no change, and the applied pressure which quickly rises to the pre-set value, while the welding temperature increases only to a certain value. In this stage, frictional heat is generated at the weld interface due to the applied pressure and oscillation, but it is not enough to soften the material sufficiently for plastic deformation. The upset then begins to increase gradually in stage 2 because the yield strength (YS) of the interface material decreases below the applied pressure due to the increased temperature, which plastically deforms the interface material. The joining temperature increases throughout this stage. The upset tends to increase at a constant velocity in stage 3, which is called the steady stage. The welding temperature does not continuously increase in this stage, which agrees with the previous simulation studies [87,105]. In this stage, the strength of the interface material decreases to a value lower than the applied pressure, which facilitates a constant-speed interface material ejection as flash without a temperature rise. Based on these results, therefore, the peak welding temperature can be determined as the temperature measured during the steady state under which the strength of the interface material decreases below the applied pressure.

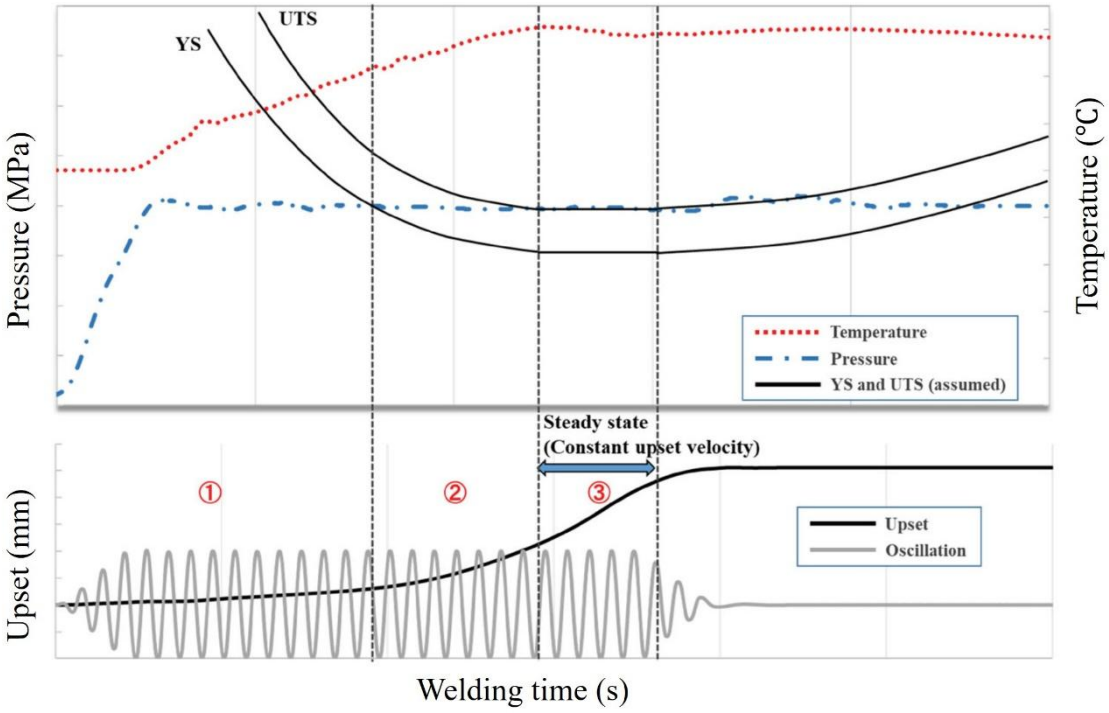

Fig. 2-16 Schematic illustration of temporal evolution of the welding temperature and the corresponding LFW parameters, including applied pressure and upset of the stationary component based on experimental data [101].

2.3.7.1. Control of welding temperature by applied pressure in LFW

As explained in the previous section 2.3.7, during LFW, the flash is expelled once the material's deformation resistance falls below the applied pressure, and the interface temperature becomes stable. As a result, the joining temperature can be uniquely determined by the applied pressure. Therefore, by evaluating the temperature dependence of the deformation resistance of the materials to be joined, it is possible to obtain the desired joining temperature by selecting the appropriate applied pressure. For instance, Fig. 2-17 schematically shows the temperature dependence of the material strength for medium carbon steel S45C. When LFW is performed with an applied pressure of 100 MPa, the temperature rises due to friction. Once the interface temperature reaches nearly 880°C, the material at the interface can no longer withstand the 100 MPa pressure, and

the expulsion of flash begins. As fresh material surface at the interface also reaches 880°C, it is expelled as flash, so the temperature of the material near the joining interface will not exceed the temperature at which flash expulsion starts. Therefore, the maximum temperature at the joint interface, i.e., the joining temperature, is nearly 880°C which is above A_3 point. Similarly, under high applied pressure of 400 MPa during LFW, the joining temperature will be ~580°C, which is below the A_1 temperature as confirmed during LFW of S45C.

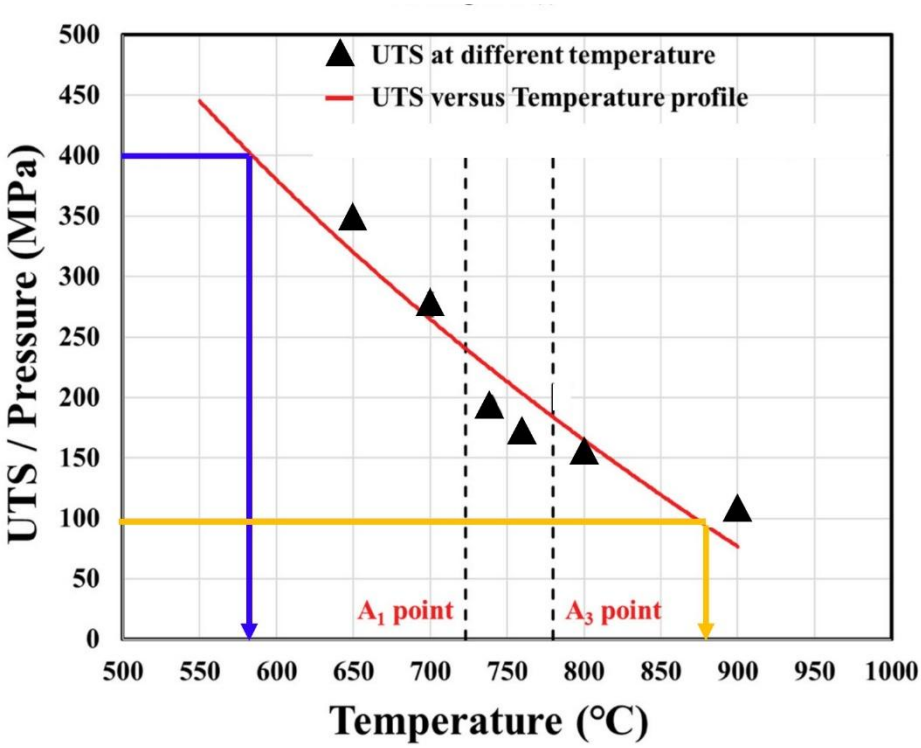

Fig. 2-17 Temperature dependence of the UTS for the S45C and the measured welding temperature at different applied pressures [101].

It is necessary to confirm the correspondence of the welding temperature with the microstructure obtained at each pressure. Kuroiwa et al. [101] successfully controlled the welding temperature below the A_1 point for the first time in low-temperature LFW of medium carbon steel S45C, as shown in Fig. 2-18a. This was achieved by exploiting the relationship between applied pressure and welding temperature illustrated in Fig. 2-17.

The SEM microstructures of the welded joints obtained under different pressures are presented in Fig. 2-18b. When applied pressures of 100 MPa and 200 MPa were exerted during LFW, a martensitic microstructure was observed at the joint interface, whereas at applied pressures of 300 and 400 MPa, a refined microstructure composed of equiaxed ferrite grains and spheroidized cementite was identified. Similarly, Aoki et al. [102] successfully joined medium carbon steel using low-temperature LFW, effectively suppressing martensitic transformation by utilizing a high applied pressure of 300 MPa due to the fact of fabrication of joint below the A_1 temperature. These findings confirm that the welding process occurred at temperatures above the A_3 point and below the A_1 point at an applied pressure of 100 MPa and 300 MPa, respectively, as indicated by the relationship between applied pressure and the temperature dependence of material strength in Fig. 2-17. Therefore, the welding temperature can be controlled by adjusting the applied pressure during the LFW process based on the temperature dependence of the material's strength. Furthermore, Fig. 2-19 shows the hardness distribution of the obtained S45C joints. Under high-temperature conditions (HT) at a low applied pressure, the joining temperature exceeded the A_3 point, leading to the formation of martensite at the weld interface, which resulted in a significant increase in hardness exceeding 600 Hv. However, as the applied pressure increased, hardening was suppressed. When welding was performed under high-pressure and low-temperature conditions (LT), the hardness near the interface was almost identical to that of the base material, resulting in a joint with a uniform hardness distribution. Also, it is noteworthy that no obvious heat-affected soft zone was identified in all the fabricated joints based on the hardness distribution. Such joints, free from mechanical property anomalies, are highly suitable for industrial applications.

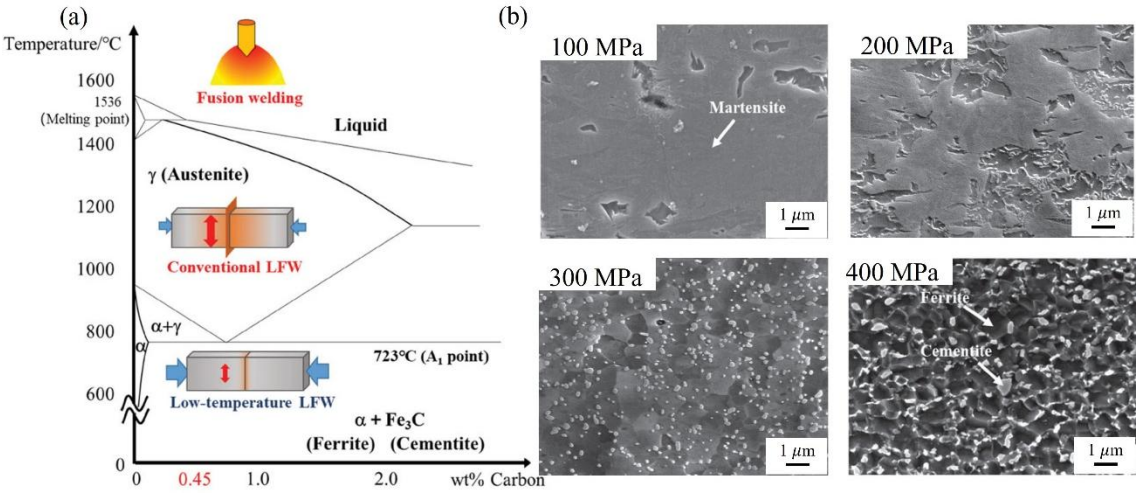

Fig. 2-18 (a) LFW of medium carbon steel (MCS) showing (a) welding temperature of different welding processes presented in Fe-C phase diagram, (b) SEM image of joint interfaces fabricated under different applied pressures [101,102].

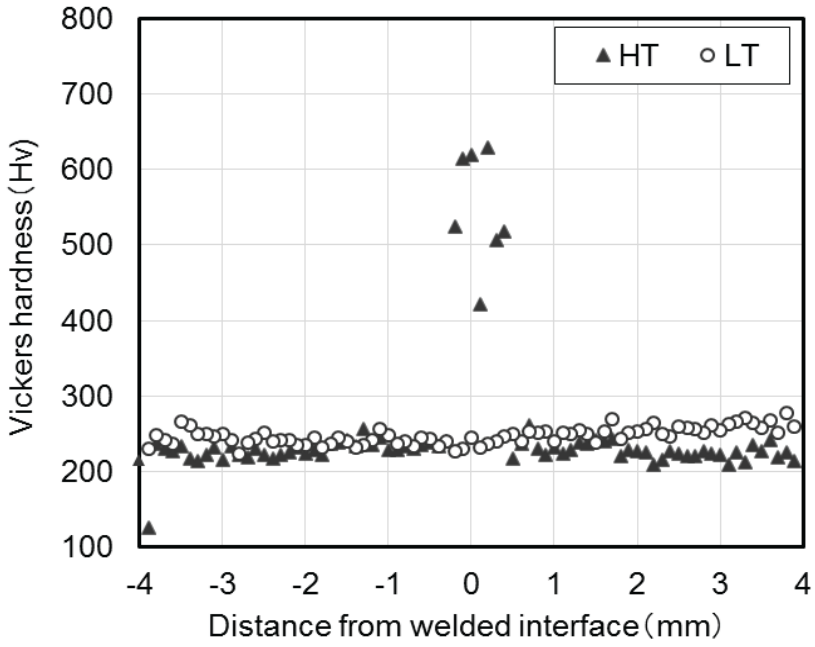

Fig. 2-19 Hardness distribution across the interface of the S45C steel joints during LFW. HT and LT refer to high temperature and low temperature conditions, respectively [102].

2.3.8. LFW of Al alloys

Al-alloys require especial consideration for welding mainly due to the presence

of surface oxide film. Moreover, the welding requirements of bulk and varied shapes in short production cycle leaves very limited alternatives, and the LFW fits very well. Welding of a number of Al-alloys such as AA1070 [106], AA7075 [107], AA5052 [108,109], AA6063 [108,109] and AA2011 [110,111] via LFW has been reported in the literature. However, aluminum alloys, compared to other engineering materials such as titanium alloys, have higher thermal conductivity, which leads to the formation of wide heat-affected zones (HAZ), making it difficult to obtain high-strength joints through LFW. Rotundo et al. [112] conducted LFW on A2024 alloy reinforced with 25% SiC dispersoid particles and obtained defect-free joints. However, the hardness distribution near the joint exhibited a hardness drop of about 10% in the HAZ, and the joint efficiency was approximately 80%. On the other hand, the joining of precipitation-hardened Al alloys, i.e., AA7075 [107] presents significant challenges, primarily due to the high temperatures involved in welding processes. These elevated temperatures with a long cycle time can lead to the coarsening or often full dissolution of the finely dispersed strengthening precipitates. The literature reveals that the size and distribution of these precipitates mainly affect the strength of AA7075 alloy joints [113]. Since the mechanical strength of precipitation-hardened Al alloys heavily depends on the size, distribution, and density of these precipitates, their degradation during welding results in a significant loss of strength and hardness in the weld metal and the heat-affected zone (HAZ) [114]. It is reported for AA7075-T651 welds that $MgZn_2$, main strengthening precipitates, get dissolved in the TMAZ due to elevated temperature during LFW [107]. The softening effect in TMAZ was also observed by Lis et al. [108] during high-frequency (250 Hz) LFW of AA6063-T5. Peak temperature of 320 °C was estimated at the weld interface. Temperatures higher than 200°C start softening in these alloys, and full dissolution of the precipitates may take

place above 400°C. The hardness vs. temperature plot at different applied pressures (Fig. 2-20a) and different friction time (Fig. 2-20b) in AA6063-T5 alloy shows a higher extent of softening with increasing temperature. Thus, it has been reported that applying LFW to precipitation-strengthened aluminum alloys often results in softened regions, which significantly reduce mechanical properties. However, recent studies [115,116] indicated that using low-temperature LFW with pressure control can effectively suppress the formation of these softened zones. Choi et al. [115] conducted LFW on the precipitation-strengthened A6061-T6 alloy and successfully achieved low-temperature joining by applying a high pressure of 240 MPa. No softened regions were observed in the joint area, and as shown in Fig. 2-21, the authors obtained a sound joint with a very flat hardness distribution and strength equivalent to that of the base material. Furthermore, Choi et al. [116] applied a high pressure of 470 MPa during LFW of A7075-T6 alloy, achieving low-temperature joining below 300°C. This resulted in a joint with 100% efficiency and hardness equal to that of the base material. Precipitates containing $MgZn_2$ and Cr were observed near the joint interface, and since the precipitation strengthening was significantly maintained together with grain refinement hardening and dislocation hardening, a high joint efficiency of 100% with base metal fracture was achieved. In addition to precipitation-strengthened aluminum alloys, research on LFW has also been reported for solid-solution strengthened aluminum alloys such as A5052. Choi et al. [117] investigated the effect of applied pressure on the joining temperature in LFW of A5052-H34 and A5083-O alloys. As shown in Fig. 2-22, the joining temperature decreased as the applied pressure increased [117]. Furthermore, in upset control, it was reported that higher applied pressure can enable joining in a shorter time. Additionally, an increase in hardness at the joint interface due to higher applied pressure was reported in both materials, and the formation of softened regions was

suppressed when an applied pressure of 100 MPa or higher was used.

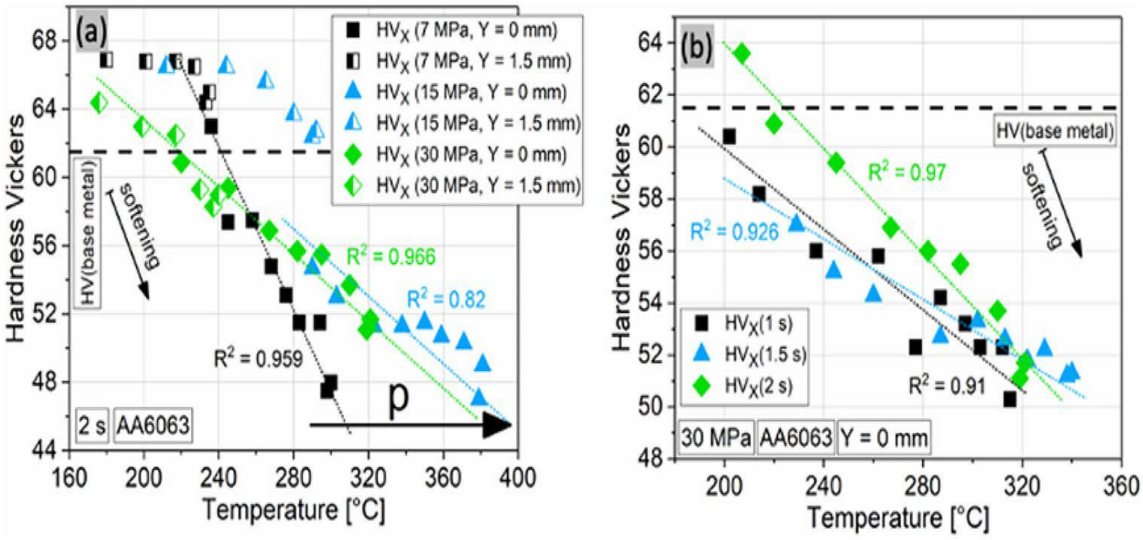

Fig. 2-20 Hardness over effective temperature for AA6063 (a) after 2s friction time under different pressure, and (b) under 30 MPa after different friction time [108].

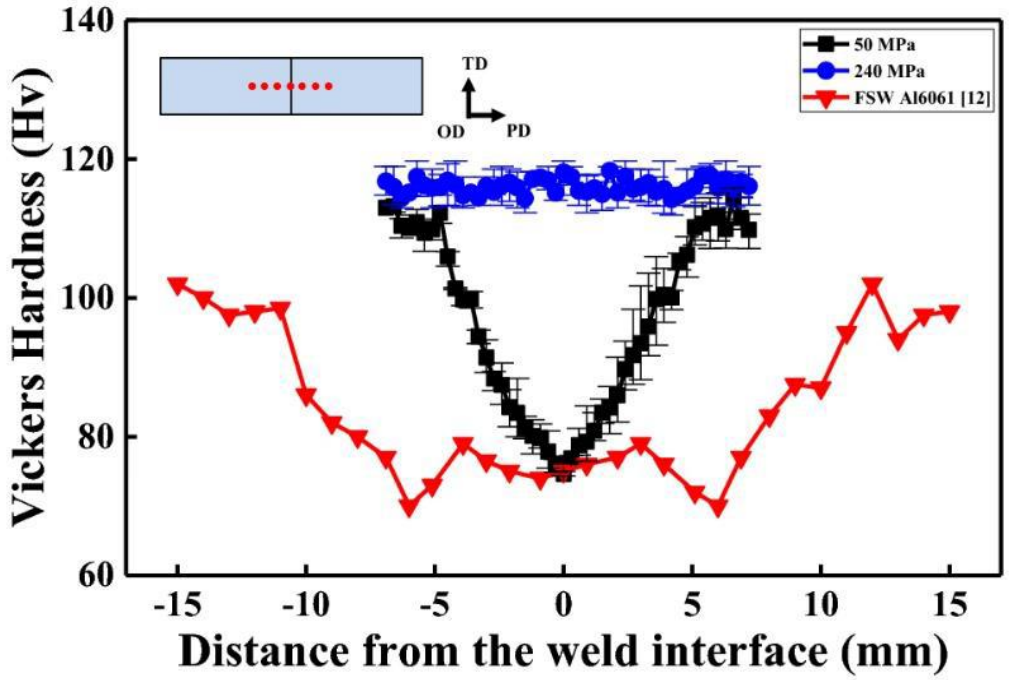

Fig. 2-21 Hardness profiles of Al6061-T6 joints obtained at applied pressures of 50 MPa and 240 MPa and FSW Al6061-T6 joints. TD, OD, and PD stand for transverse direction, oscillation direction, and pressure direction, respectively [115].

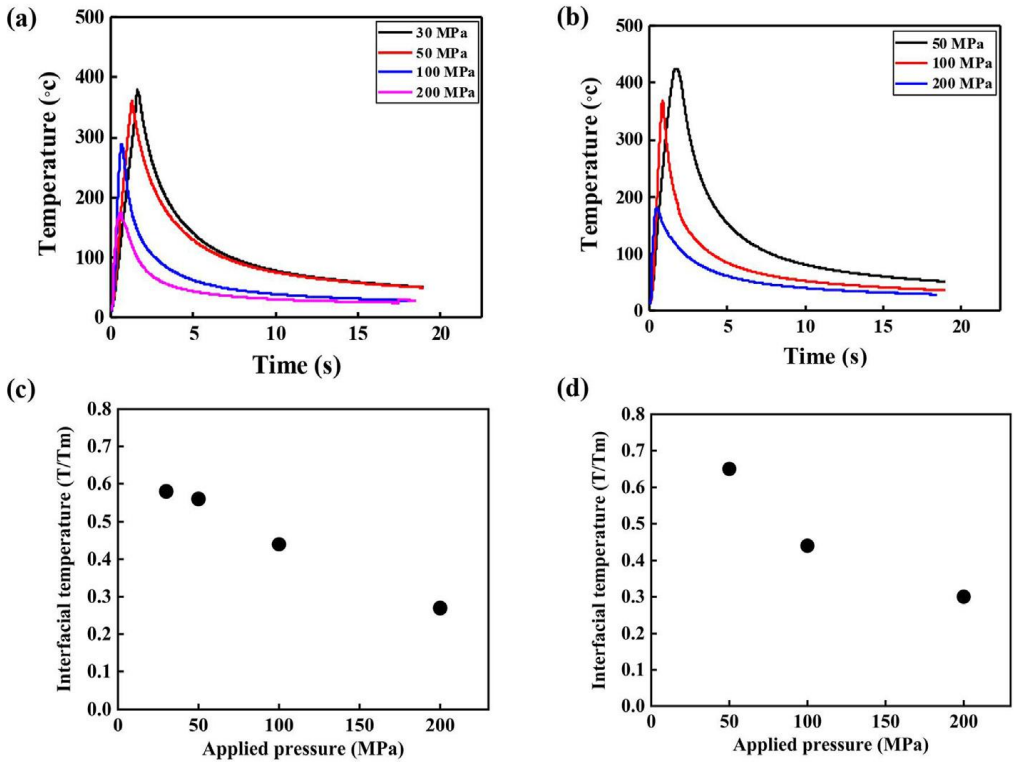

Fig. 2-22 The thermal histories of (a) AA5052-H34 joint and (b) AA5083-O joint and peak interfacial temperature of (c) AA5052-H34 joint and (d) AA5083-O joint [117].

2.3.9. Dissimilar joining of steel and Al alloys using LFW

As aforementioned in section 2.1, the formation of excessive IMCs during conventional fusion welding of steel and aluminum alloys presents a significant challenge, often resulting in low joint efficiency. This issue highlights the necessity of conducting the joining process at temperatures below the melting points of the base materials to prevent the excessive growth of IMC layers. Linear Friction Welding (LFW), being a solid-state welding technique, enables joining to occur below the melting point of the parent metals, thereby effectively suppressing the formation of brittle IMC layers. Matsuda et al. [118] conducted high-frequency LFW on a dissimilar combination of stainless steel SUS304 with A6063-T5 and A5053-O achieving a joint efficiency of 94.9% with respect to A5053-O with the SUS304/A5053-O joint, where a thin IMC layer less than 500 nm was formed at the interface. Additionally, the dissimilar SUS304/A6063-T5 joint

showed a maximum joint efficiency of 89.7% with respect to A6063-T5, with an extremely thin IMC layer of less than 50 nm was observed at the joint interface [118,119]. However, besides the IMC thickness at the dissimilar joint interface, each materials' plastic deformation around the joint has a substantial impact on the weld strength. Typically, in the dissimilar joining of materials using LFW or other friction welding methods, the temperature initially rises to the deformation temperature of the material with lower strength as both materials are simultaneously heated up by frictional heat. This phenomenon leads to the occurrence of deformation only on the parent material having lower strength. Consequently, no plastic deformation occurs toward the stronger material side. This results in rugged surfaces and retained oxides at the joint interface. Therefore, it becomes challenging to obtain a sound dissimilar joint, as previously reported during dissimilar LFW of AA6082 and AA2011 aluminum alloys [120] and during continuous friction welding of cp-titanium and AISI 316L [19]. Kimura et al. [121] conducted an investigation to assess the possibility of direct joining between A7075-T6 aluminum and low carbon steel using the rotary friction welding method. However, it was reported that obtaining a sound joint was difficult due to insufficient plastic deformation characteristics of A7075-T6 during welding. Therefore, it is essential not only to minimize the interface IMC thickness but also to promote simultaneous deformation of dissimilar alloys around the weld interface to obtain a sound dissimilar joint. Simultaneous interfacial deformation of dissimilar alloys during welding is possible through LFW by exploiting a concept of cross-point as exemplified by Liu et al. [122] during dissimilar friction welding. Briefly, if the welding temperature can be controlled to the temperature at which both materials have the same strength, i.e., at the intersection or cross-point of the graph of temperature dependence of strength. By applying pressure corresponding to this cross-point strength,

both materials will be expelled as flash simultaneously, leading to the formation of a high-quality welded interface. This is the aforementioned cross-point concept. Fujii [123] reported the utilization of cross-point concept to obtain sound dissimilar joint between SUS316L and Ti-6Al-4V by optimizing the applied pressure based on the temperature dependence of the material strength of these alloys. This approach is effective in promoting simultaneous interfacial deformation, and high-quality joints can be achieved. Fig. 2-23 schematically illustrates the temperature dependence of the strength of Ti-6Al-4V and SUS316L and its relationship with the applied pressure during dissimilar LFW. As shown in the Fig. 2-23a, at room temperature, Ti-6Al-4V is stronger than SUS316L. However, as the temperature increases, the strength of Ti-6Al-4V rapidly decreases and that of SUS316L much more slowly decreases. As a result, the material strengths of Ti-6Al-4V and SUS316L reversed at room and high temperatures, and the curves expressing temperature dependence behavior of these alloys have an intersection point (cross-point). Therefore, as shown in Fig. 2-23a, when pressure is applied below the cross-point, the temperature increase due to friction causes the strength of Ti-6Al-4V to drop below the applied pressure. Therefore, Ti-6Al-4V is expelled as flash, while SUS316L maintains a higher strength and does not deform. On the other hand, if pressure is applied above the cross-point strength, the flash is only expelled from the SUS316L side, while the Ti-6Al-4V side remains undeformed. The inhomogeneous interfacial deformation of materials during LFW may leave oxides and unbonded areas at the interface, resulting in a poor-quality joint. In contrast, when the weld interface temperature is controlled to the cross-point by adjusting the applied pressure, as shown in Fig. 2-23b, both materials can be simultaneously deformed, effectively removing oxides and impurities from the interface and producing a high-quality dissimilar joint. Therefore, a sound dissimilar joint can be

achieved by exploiting the cross-point concept.

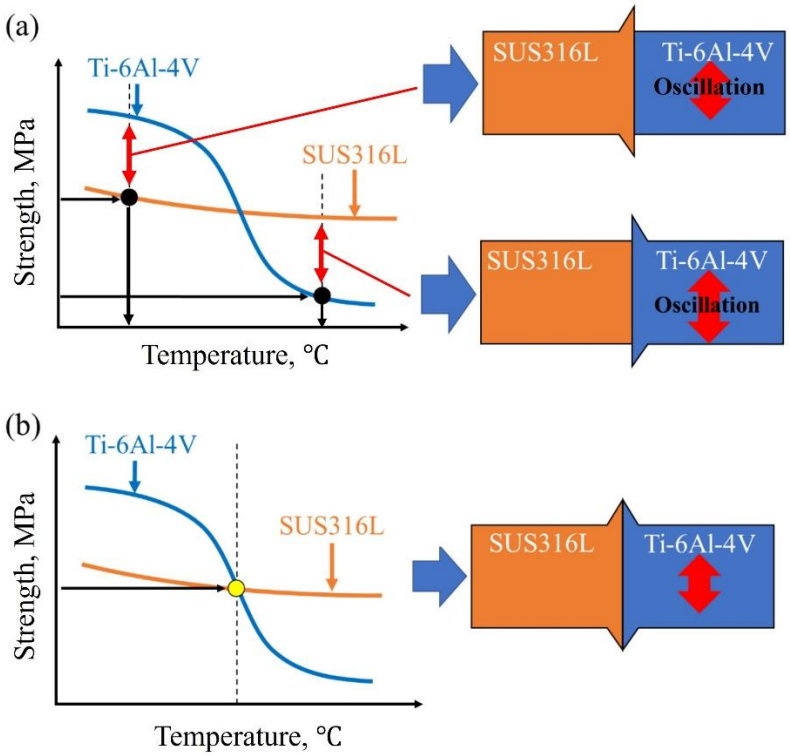

Fig. 2-23 Schematic illustration of temperature dependence of material strength utilizing cross-point concept for LFW of Ti-6Al-4V and SUS316L.

2.4. Center-driven double-sided LFW and its joining concept

As mentioned in the previous section, a sound dissimilar LFW joint can be achieved by exploiting the cross-point concept. However, certain dissimilar combinations of steel and aluminum alloys do not exhibit a cross-point at any temperature, viz., there is no common temperature at which their strengths are comparable. The lack of cross-point existence in the mating materials makes it difficult to simultaneously deform both alloys and its rather challenging to effectively remove the surface oxides during conventional LFW. Fig. 2-24a shows the schematic diagram of the temperature dependence of material strength for aluminum alloy A7075-T6 and carbon steel S45C. In this combination of dissimilar alloys, there is no cross-point on the temperature-dependence of materials strength curves, indicating the absence of a temperature at which both materials exhibit

comparable strength. The absence of cross-points in the strengths of alloys makes it challenging to deform both alloys simultaneously during welding. In other words, A7075-T6 exhibits consistently lower strength than S45C across all temperatures. As a result, A7075-T6 undergoes preferential deformation and is expelled as flash, irrespective of the applied pressure during conventional LFW as illustrated in Fig. 2-24b. Consequently, oxides and unbonded regions may persist at the interface due to the absence of interfacial deformation towards S45C side, making it challenging to obtain a sound dissimilar joint [71]. To address this issue, center-driven double sided LFW method, which is capable to effectively weld three dissimilar materials simultaneously, was utilized. Fig. 2-25 shows the concept of the center-driven double-sided LFW process. Unlike conventional LFW method, center-driven double-sided LFW comprises placing a center material between the two side materials to be joined. Center material is subjected to the linear oscillation motion while all three materials are pressed against each side independently to simultaneously join the center material and the primary materials to be joined.

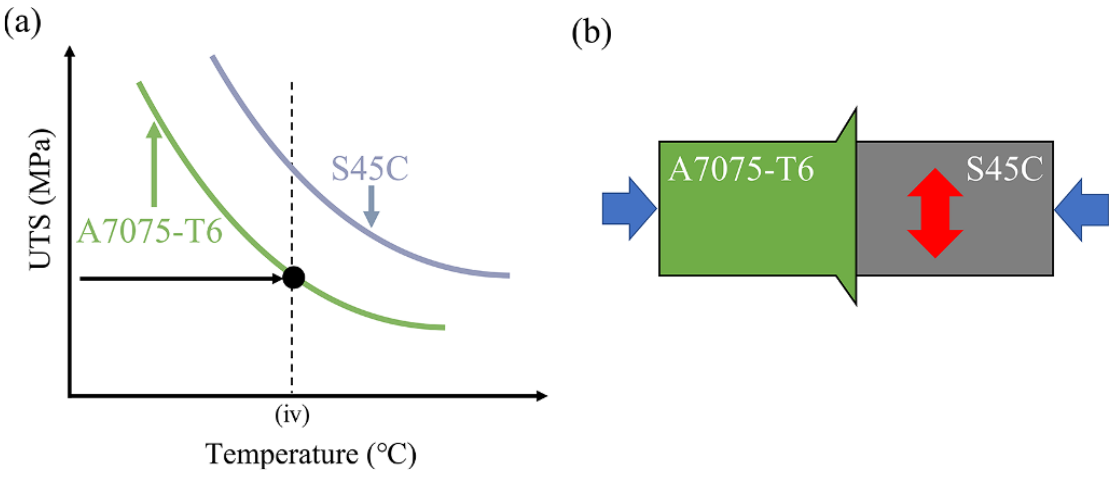

Fig. 2-24 (a) Schematic illustration of the temperature dependence of the material strength of S45C carbon steel and A7075-T6 Al alloy, and (b) a diagram of conventional LFW for S45C and A7075-T6 [71].

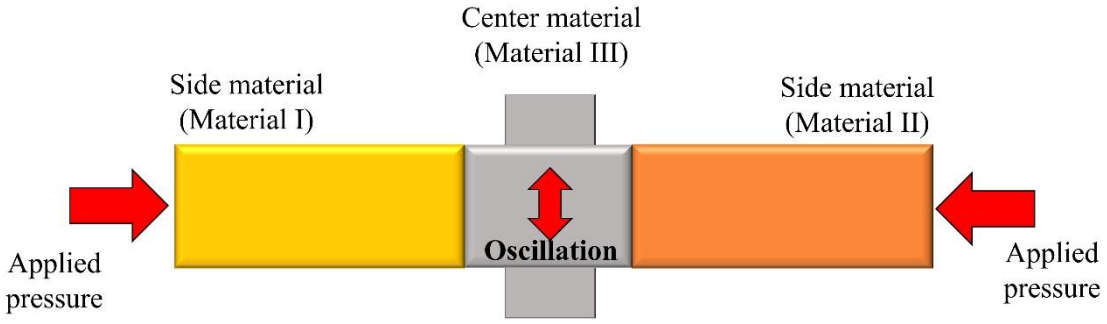

Fig. 2-25 Schematic illustration of joining concept of center-driven double-sided LFW method to simultaneously join three dissimilar materials.

For instance, Ito et al. [71] attempted simultaneous joining S45C carbon steel and A7075 aluminum alloy employing center-driven double sided LFW method using pure Ni as a center material. The temperature dependence of materials' strength and joining principle for pure Ni, S45C, and A7075 is illustrated in Figs. 2-26a and b, respectively. As shown in Fig. 2-26, pure Ni revealed two different temperatures at which the material strength is equal to those of both S45C and A7075-T6 alloy. As a result, the cross-points of each combination of S45C/Ni and Ni/A7075-T6 were achieved simultaneously. Therefore, LFW was successfully achieved by applying a high pressure corresponding to the cross-point strength at the A7075-T6/Ni interface, where both materials were simultaneously deformed at low temperature, and a low pressure at the S45C/Ni interface, where both materials exhibited a simultaneous deformation at high temperature.

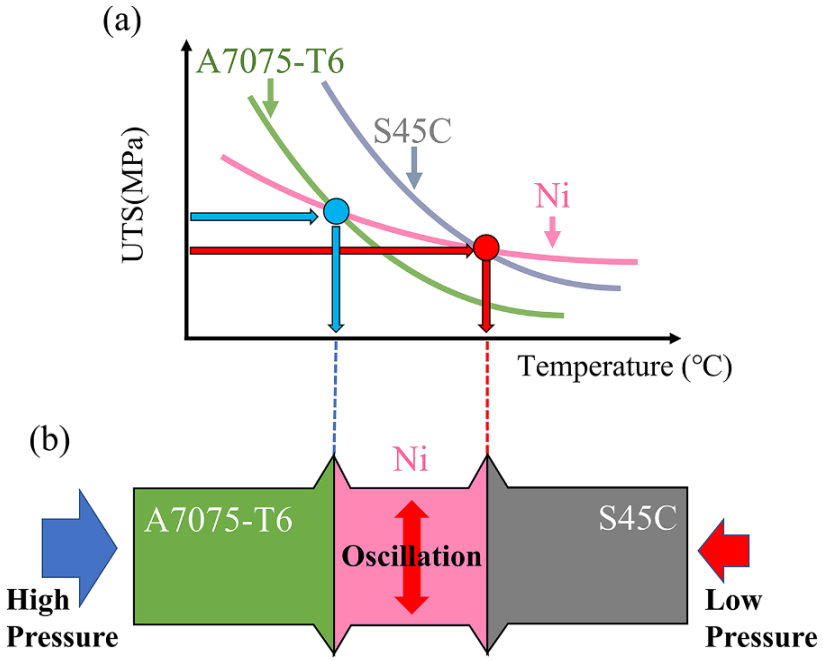

Fig. 2-26 (a) Schematic of the temperature dependence of the material strengths of pure Ni, S45C carbon steel, and A7075-T6 Al alloy and (b) a diagram of center-driven double-sided LFW of A7075-T6, Ni and S45C [71].

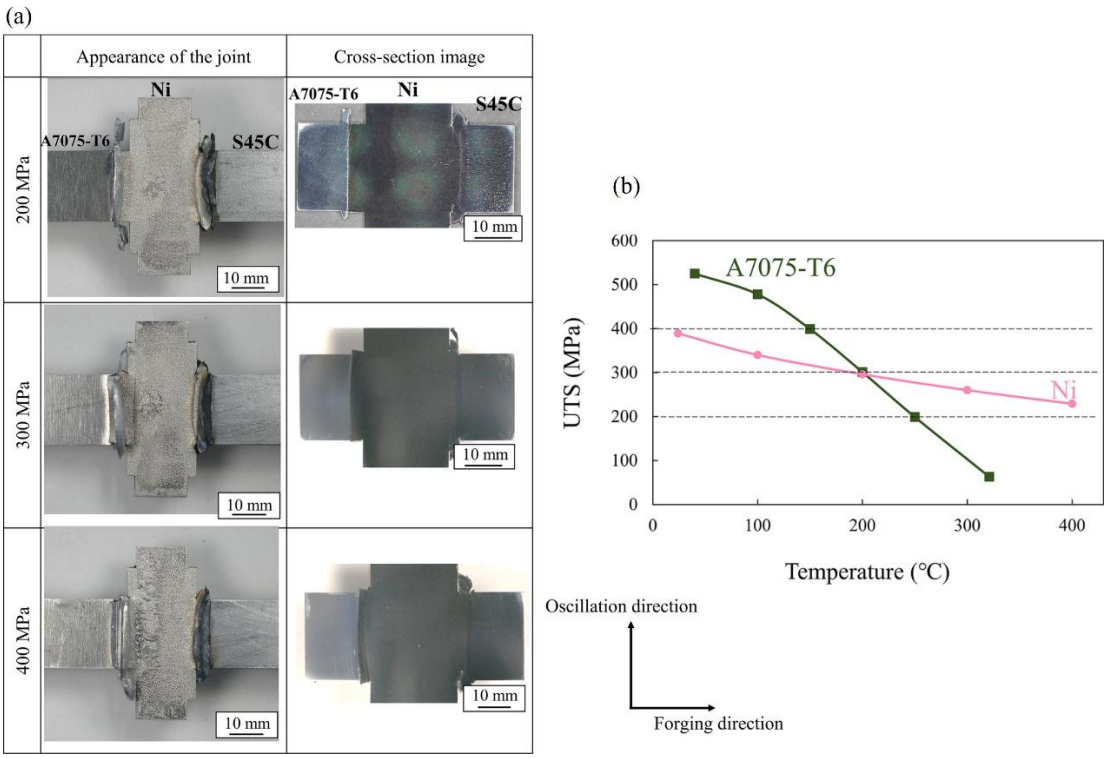

Fig. 2-27 (a) Appearance and cross-sectional macrophotographs of the joints obtained under various applied pressures towards at Ni/A7075 alloy interface, and (b) Temperature dependence

of the material strength for Ni and A7075-T6 alloy [71].

The appearance and cross-sectional macrographs of the welds obtained under different applied pressures are presented in Fig. 2-27a. The simultaneous joining of all three materials was successfully achieved under all LFW conditions, though the interfacial deformation behaviors varied. These variations in interfacial deformation between the mating materials are explained based on the temperature dependence of material strength, as shown in Fig. 2-27b. Reportedly, at 200 MPa, A7075-T6 deformed preferentially and the welding process was completed before pure Ni began to deform. This is because the strength of A7075-T6 dropped below the applied pressure earlier than Ni due to the rise in interface temperature during LFW. Conversely, at 400 MPa, the strength of pure Ni was initially lower than the applied pressure, causing it to deform preferentially, while the A7075-T6 side underwent only slight deformation. At 300 MPa, both pure Ni and A7075-T6 experienced sufficient interfacial deformation because the applied pressure matched the cross-point strength, leading to simultaneous deformation of both alloys. As a result, interfacial oxides and impurities were expelled from the joint interface and the weld produced under 300 MPa revealed peak joint efficiency of 92 % with respect to pure Ni. Concerning the Ni/S45C joint interface, no weld defects were observed at S45C/Ni joint interface. Additionally, martensite was detected in the microstructure of the joint towards S45C, suggesting that joining temperature on the S45C side was increased to A_3 point or higher. Moreover, the peak hardness, 700 Hv, was consistently observed in the vicinity of S45C interface across the entire weld, which can be attributed to the martensitic transformation due to elevated temperature at S45C/Ni interface. Therefore, the center-driven double-sided LFW method can be utilized to simultaneously join three different materials. A sound joint can be achieved even between dissimilar material pairs

that lack a cross-point in their strength vs. temperature curves. This is accomplished by applying different pressures on either side, each corresponding to the cross-point strength relevant to that material pair. However, in all the conditions the produced welds were fractured at Ni/A7075 alloy interface, indicating the ongoing challenges in optimizing this process for dissimilar materials.

2.5. Summary, research gap and thesis objective

As discussed above, certainly, the dissimilar joining of steel and aluminum alloys is indispensable to realize the benefits of multi-materials. Al alloys are considered highly preferred materials for transportation applications owing to their combination of favorable properties, including excellent formability, a high strength-to-weight ratio, and high corrosion resistance. These characteristics make Al alloys particularly well-suited for applications that demand lightweight yet structurally robust components, such as in automotive, aerospace, and railway industries, where reducing overall weight contributes significantly to improved fuel efficiency and reduced environmental impact. Conversely, steel has been recognized as one of the most widely utilized structural materials in both the construction and transportation sectors, primarily due to its high mechanical strength, cost-effectiveness, and well-established manufacturing infrastructure.

Given the complementary properties of Al alloys and steel, obtaining a sound dissimilar joint between steel and Al alloys is essential. As a result, a wide range of studies has been conducted to explore the potential effective techniques for the dissimilar joining of Al alloys and steel, with the aim of enabling multi-material design in high-performance lightweight structures. However, conventional fusion welding techniques lead to the formation of thick and brittle IMCs at the dissimilar joint interface, resulting in a brittle fracture of the joints. Moreover, the beneficial influence of employing solid-state welding

methods in dissimilar joining of steel and Al alloys has been widely acknowledged in various studies to suppress the IMC formation. However, achieving reliable joints presents several challenges, among which precise control of the joining temperature is particularly critical.

In this study, the focus is placed on LFW method**,** a solid-state joining process capable of temperature control through applied pressure, as a promising solution for dissimilar material joining below the melting point of the base materials. Generally, in dissimilar welding of steel and Al alloys using the conventional LFW method, IMC thickness at the joint interface is a key factor. In addition to IMC formation, the plastic deformation characteristics of each material at the dissimilar joint interface also play a crucial role in determining the weld strength, as discussed in detail above. Therefore, it is essential not only to minimize the interface IMC thickness but also to promote simultaneous deformation of dissimilar alloys around the critical weld interface to obtain a sound dissimilar joint.

2.5.1. Research gap

The current chapter reviewed the research progress that has been undertaken so far for achieving reliable joining between steel and Al alloys using solid state welding. Nevertheless, following concerns need to be addressed. These concerns can be summarized in the following wider point of view:

- Although, it is reported that simultaneous interfacial deformation of dissimilar alloys, i.e., steel and Al alloy, during welding is possible by LFW exploiting cross-point concept. However, for certain dissimilar combinations of steel and Al alloys, a temperature at which their temperature-strength curves can possess a cross-point does not exist, owing to the substantial mismatch in their strength levels across the

entire temperature range. Namely, there is no favorable temperature at which the materials' strengths are equal. The absence of cross-point in the strengths of particular Al alloy and steel makes it challenging to deform both materials simultaneously and difficult to effectively remove the surface oxides during conventional LFW. Therefore, in such cases obtaining a sound joint is extremely challenging.

- Despite the efforts made by Ito et al. [71] to achieve a sound dissimilar joint between the dissimilar combination of steel and Al alloy lacking a cross-point in their temperature-strength curves. Although their approach was based on the cross-point concept utilizing CDDS-LFW, the resulting weld exhibited fracture at the interface. This highlights the ongoing challenges to further optimize the process and achieve more efficient dissimilar joints.
- Additionally, since the insert material used during CDDS-LFW is typically the weakest part of the weld, it is possible that even if the interfacial fracture is avoided, the joint strength may still be limited by the strength of the center material. This raises further concerns about the need to develop the process to further enhance joint strength.

2.5.2. Thesis objective

The objective of this thesis is to overcome the challenges of conventional LFW method and to obtain sound dissimilar joint between steel and Al alloys with improved joint strength. The primary objectives are detailed as follows:

- Previous studies on LFW of carbon steel and Al alloys suffers to prevent fracture at the joint interface, primarily due to the formation of brittle intermetallic-compound (IMC) layer and lack of simultaneous interfacial deformation of mating materials during welding. Therefore, in this study, efforts are invested to enhance joint

efficiency and fracture mode of steel and Al alloy dissimilar weld by promoting simultaneous interfacial deformation of mating materials. This was achieved by exploiting cross-point concept of temperature-strength curves, with aim of producing sound dissimilar joint between steel and Al alloys with minimized IMC thickness at the interface.

- To systematically explore the process parameters of center-driven double-sided (CDDS)-LFW and to achieve sound dissimilar joint between steel and Al alloys couple, which have a cross-point at extremely low temperature or lack a cross-point in their temperature-strength curves. The primary objective is to enhance joint efficiency and improve fracture mode while overcoming the inherent challenges of the CDDS-LFW method that previous study has faced.
- To explore strategies for further enhancing joint strength of steel and Al alloy dissimilar weld. Since the joint strength in CDDS-LFW can be limited by the strength of the center material, efforts have been invested to eliminate this dependency and improve overall joint performance. Building upon these efforts, a novel joining method termed as sacrificing-sheet linear friction welding (SSLFW) was developed and utilized to effectively weld dissimilar couples of steel and Al alloys that are particularly difficult to be joined by using conventional LFW. Consequently, SSLFW is expected to offer a promising solution to the limitations faced in CDDS-LFW and holds potential for further improving joint strength in dissimilar material welding.

Chapter 3: Materials and experimental procedure

Throughout the thesis, this chapter presents materials and the main methodologies and techniques employed for the materials preparation, LFW joining equipment, metallurgical and mechanical characterization. Additionally, specified tests; if any, and utilized joining technique will be presented in the related chapters.

3.1. Experimental procedure

3.1.1. Test Materials

In the current study, three different types of steels; JIS SPHC mild steel, JIS SS400 structural carbon steel, JIS S45C medium carbon steel, with significantly different microstructures and mechanical strengths were selected to be joined with two types of precipitation-strengthened Al alloys, viz. JIS A7075-T6 alloy and JIS A6061-T6 alloy. A total of four combinations of dissimilar joints were obtained as follows.

- Direct joining of mild steel and A7075-T6 Al alloy using conventional LFW method.
- Dissimilar joining of SS400 structural carbon steel and A7075-T6 Al alloy using mild steel as a center material, utilizing an innovative center-driven double-sided LFW (CDDS-LFW) method.
- Dissimilar joining of SS400 structural carbon steel and A7075-T6 Al exploiting novel sacrificing-sheet linear friction welding (SSLFW) method.
- Dissimilar joining of S45C medium carbon steel with A6061-T6 Al using novel SSLFW method.

All the base materials were prepared in the desired dimensions as provided in each individual chapter. The chemical compositions (wt. %) and ultimate tensile strength (UTS) of base materials are listed in Table 3-1.

Table 3-1 Chemical compositions (wt%) and UTS of the base materials.

Material	Si	Fe	Cu	Mn	Mg	Cr	Zn	Ti	Al	UTS (MPa)
A7075-T6	0.08	0.19	1.5	0.04	2.2	0.19	5.8	0.03	bal.	589
A6061-T6	0.7	0.34	0.3	0.06	1	0.16	-	-	bal.	320
Material	**C**	**Si**	**Mn**	**P**	**S**	**Fe**	**-**	**-**	**-**	
Mild steel	0.05	0.005	0.24	0.015	0.007	bal.	-	-	-	347
SS400	0.16	0.16	0.67	0.014	0.006	bal.	-	-	-	482
S45C	0.46	0.18	0.66	0.010	0.004	bal.	-	-	-	762

3.1.2. Center-driven double-sided LFW

The specimens were linear friction welded using center-driven double sided LFW (CDDS-LFW) equipment (Model Number; 8AT2020A00, TOYO KOGYO). Fig. 3-1 illustrates the CDDS-LFW setup, shape and placement of the used specimens. The entire apparatus and an internal view of the joining unit are shown in Figs. 3-1a and b, respectively. The joining is accomplished by oscillating the center specimen between two side materials and applying pressure from both sides independently which enables simultaneous joining of the center material and the two side materials as shown in Fig. 3-1c. It is difficult to perform such simultaneous joining of two sides using conventional LFW equipment. Furthermore, as shown in Fig. 3-2, the system is also designed to perform conventional LFW between two components. This is achieved by replacing the workpiece clamping fixture on one side with a special supporting fixture that reinforces the oscillation mechanism's part from the rear, enabling it to withstand the opposing pressure.

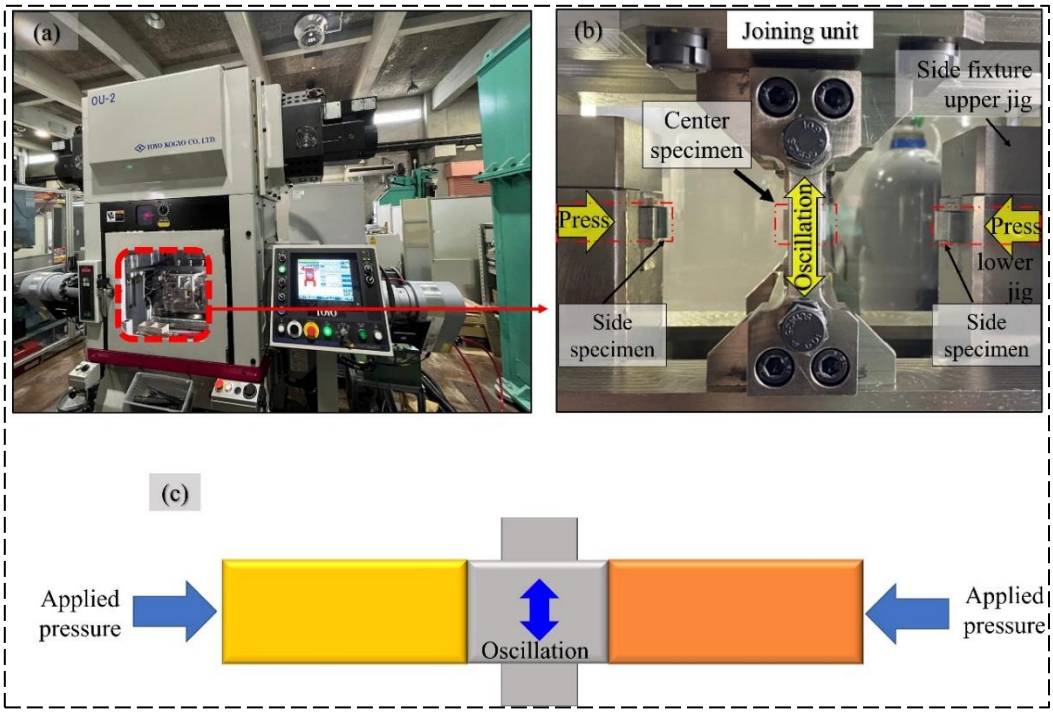

Fig. 3-1 Experimental setup of CDDS-LFW, (a) entire setup, (b) internal view of the joining unit, (c) shape of the used specimens.

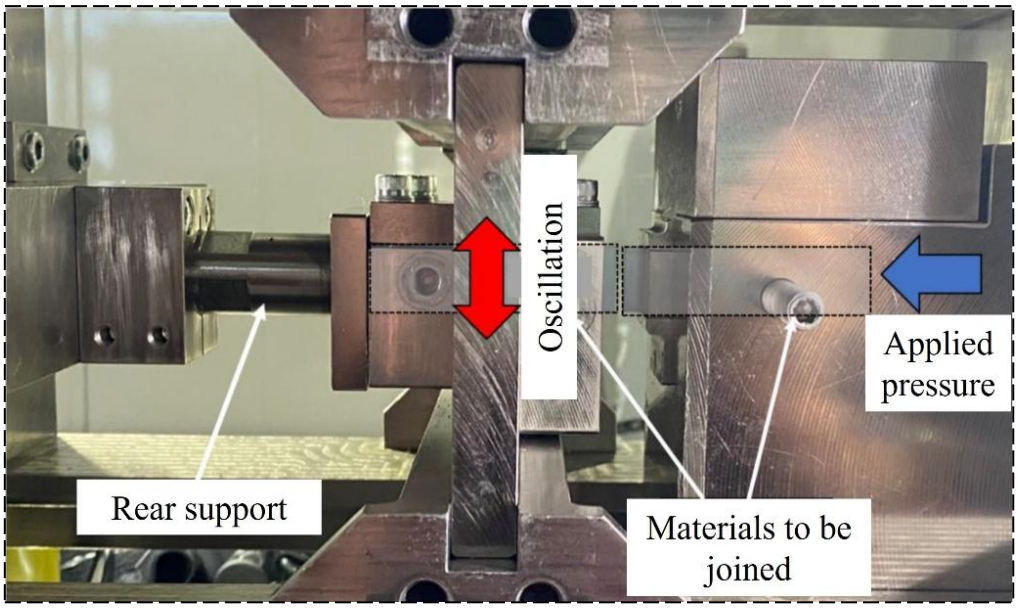

Fig. 3-2 Interior view of the equipment for conventional LFW process.

3.2. Metallographic and mechanical samples preparation

From the obtained joints, specimens for the tensile tests and microstructural observations were cut perpendicular to the joining direction using electric discharge machine (EDM; Sodick AG360L) as shown in Fig. 3-3. Fig. 3-3a shows the schematic illustration of the extracted tensile test specimen with a gauge section of 2 mm thickness, 3 mm wide, and 20 mm long. Additionally, the procedure to extract microstructure and microhardness specimens are illustrated in Fig. 3-3b. The specimens for microstructural observation illustrated in Fig. 3-3b were cut using the same EDM machine and mechanically polished with abrasive papers up to 4000 grit and subsequently polished by 1 μm diamond suspension and oxide polishing suspension (OPS) to observe the joint interface microstructure. The microhardness measurements were also conducted on the same microstructural observation specimens. Furthermore, from the obtained joints, longitudinal cross-sectional specimens containing complete weld interfaces were also extracted and mechanically polished with abrasive papers up to 4000 grit, followed by 1 μm diamond suspension to observe the joint cross-sectional macro-morphology. Additionally, thin foil specimens, with a thickness of 0.1 μm, were sectioned from selected regions of the joints interface using a focused ion beam machine in order to characterize the IMCs formed using a transmission electron microscope.

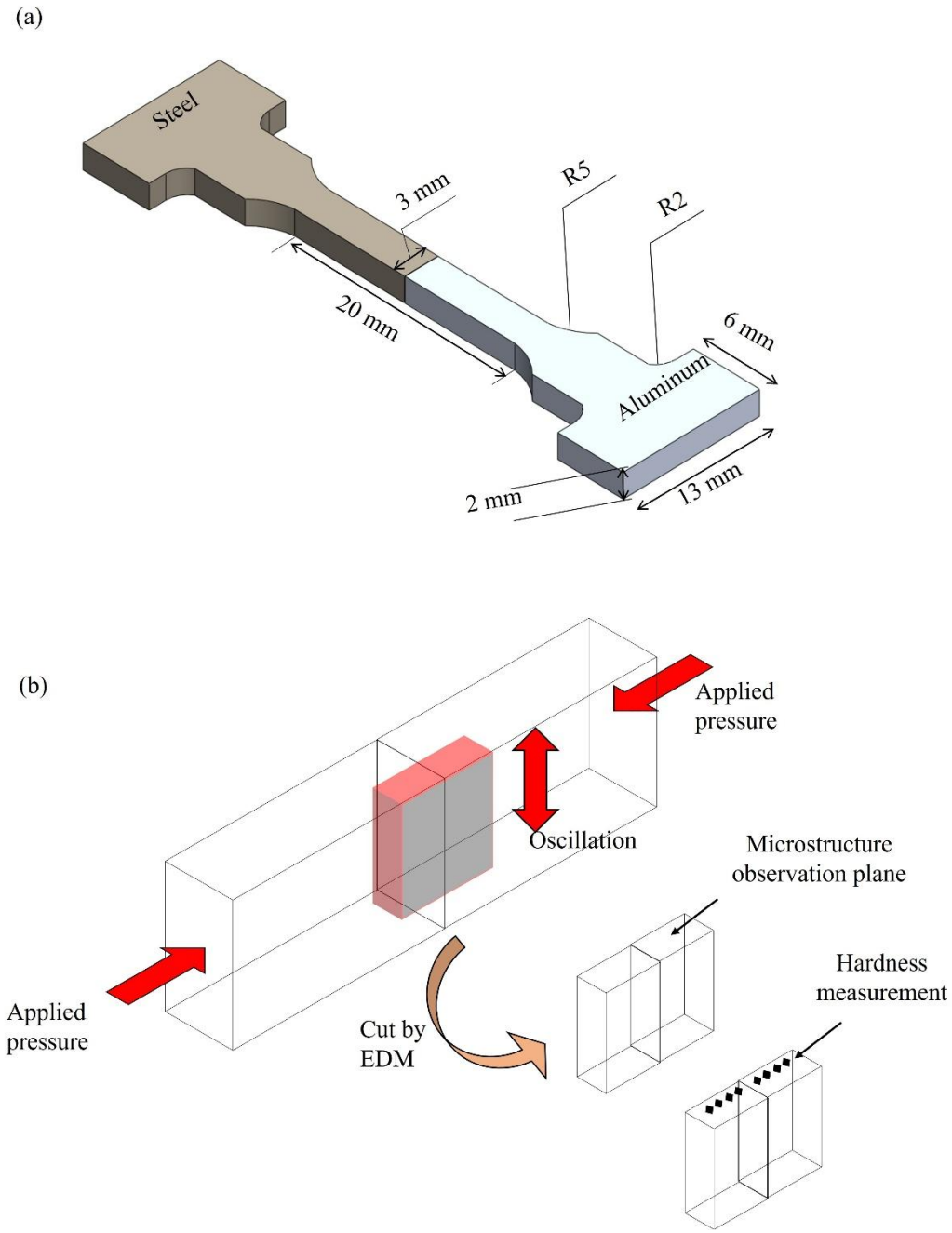

Fig. 3-3 (a) Schematic illustration of tensile test specimen, and (b) microstructural observation and microhardness specimen extracted from the joint interface.

3.3. Tensile tests

To evaluate the joint strength of the produced welds, all the tensile tests were conducted at room temperature. The uniaxial quasi-static tests were carried out by SHIMADZU AGS-X-10 KN universal tensile testing machine at a cross-head speed of 1

mm/min. The samples were prepared perpendicular to the joining interface in the desired dimensions. Moreover, tests were repeated for each joint parameter to confirm the consistency of the results obtained.

3.3.1. High temperature tensile test

High-temperature tensile tests were performed to evaluate the temperature dependence of material strength of the used base metals (BM) using SHIMADZU AGS-X-10 KN. The dimension of tensile specimens for high temperature test were 5 mm gauge length, 2 mm gauge width and 2 mm gauge thickness. High-temperature tests were performed, ranging from room temperature to 900℃ and the tensile strength were recorded corresponding to the tested temperature. Eventually, the temperature dependence of the materials' strength graphs was plotted from the obtained results.

3.4. Microhardness assessment

The Vickers hardness measurement of the obtained welds was conducted across the joint interface using a microhardness tester (FM-800, FUTURE-TECH). The measurements were performed on a straight line perpendicular to the joint interface at an interval of 0.25 mm and under an applied load of 0.98 N for a dwell time of 15 s.

3.5. Scanning electron microscope analysis

A field-emission scanning electron microscope (FE-SEM; JSM-7001FA, JOEL) equipped with energy dispersive X-ray spectroscopy (EDS) was employed to characterize the microstructure of the joint interface and base metal (BM). SEM and EDS analysis was performed on the joint interface, while only SEM was used to observe the macro-morphology of the obtained weld. SEM provided the understanding of the quality of the obtained welds at the joint interfaces, while EDS provided the elemental compositions across the joint interface.

3.6. Electron backscatter diffraction analysis

Electron backscatter diffraction analysis (EBSD) is an SEM-based technique used to obtain detailed crystallographic information about materials. EBSD sample preparation included polishing using oxide polishing suspension (OPS) to obtain the finely polished specimens. The EBSD data were collected at an accelerating voltage of 15 kV with a working distance of 15 mm. The step size during EBSD was set at 0.2 μm with a tilt angle of specimens to be 70°. The obtained EBSD maps were analyzed and processed using the TSL OIM™ software. EBSD was employed to investigate the grain size, structure, and crystallographic orientation within selected regions of the obtained joints.

3.7. Transmission electron microscope analysis

Transmission Electron Microscopy (TEM) is an advanced technique for investigating microstructures and analyzing chemical compositions at the nanoscale. In this study, the TEM (TEM; JEM-2100F JEOL) equipped with an EDS detector was used to further characterize the interfacial IMCs. It is well known that the thickness of IMC layers at dissimilar interfaces can be so small that distinguishing these layers using SEM becomes highly inefficient and difficult. Therefore, detailed TEM analyses were extensively performed on most of the joints produced. However, special sample preparation technique is required to obtain ultra-thin TEM foil specimens (with a thickness of approximately 0.1 μm) prior to conducting the TEM analysis. For this purpose, the focused ion beam machine (FIB; JIB-4500, JEOL) was utilized to extract thin foil specimens from targeted locations of the joint interfaces and detailed characterization of the IMCs were then conducted using TEM.

Chapter 4: Dissimilar linear friction welding of A7075-T6 Al and mild steel

This chapter reports the dissimilar linear friction welding between mild steel and A7075-T6 Al alloy. The joint defects were effectively suppressed, and a sound dissimilar joint was obtained by promoting the simultaneous interfacial deformation of both alloys by exploiting the cross-point concept. The base materials used in this study were JIS SPHC mild steel (hereinafter referred to as steel) and JIS A7075-T6 aluminum alloy (hereinafter referred to as A7075). The content of this chapter is mostly adapted from the published manuscript ‘‘Sound dissimilar linear friction welding of A7075-T6 Al and mild steel by simultaneous interfacial deformation using higher forging speed’’ authored by Furkan Khan, Takuya Miura, Tetsuro Ito, Yoshiaki Morisada, Kohsaku Ushioda, Hidetoshi Fujii, *Journal of Manufacturing Processes,* 2024;109:512-523.

4.1. Introduction

As mentioned in section 2.3.9 of Chapter 2, the formation of excessive IMCs during conventional fusion welding of steel and aluminum alloys presents a significant challenge and often results in poor joint efficiency. This issue highlights the necessity of conducting the joining process at temperatures below the melting points of the base materials to prevent the excessive growth of IMC layers at the interface. LFW, being a solid-state welding technique, enables joining to occur below the melting point of the parent metals, thereby effectively suppressing the formation of brittle IMC layers.

However, besides the IMC thickness at the dissimilar joint interface, each materials’ plastic deformation around the joint has a substantial impact on the weld strength. Typically, in the dissimilar joining of materials using LFW or other friction welding

methods, the temperature initially rises to the deformable temperature of the material with lower strength as both materials are simultaneously heated up by frictional heat, causing deformation to occur only on the alloy side having lower strength. Consequently, no plastic deformation occurs towards the stronger material side, leaving rugged surfaces and oxides at the joint interface. In such cases, it is challenging to obtain a sound dissimilar joint. Therefore, it is essential not only to minimize the interface IMC thickness but also to promote simultaneous deformation of dissimilar alloys around the critical weld interface to obtain a sound dissimilar joint.

The present study aims to attempt linear friction welding of high-strength A7075-T6 Al and mild steel in order to produce a sound dissimilar joint using LFW method. The simultaneous interfacial deformation of both alloys is promoted by exploiting the cross-point concept. This resulted in suppressing the joint defects, leading to excellent dissimilar joining. In addition, the influence of forging speed on joint strength, and the formation of weld defects at the joint interface are investigated. Moreover, it focuses on optimizing the applied pressure by considering the temperature dependence of the material strengths of mild steel and A7075 aluminum alloy.

4.2. Materials and experimental methods

Mild steel and A7075-T6 specimens, each measuring 67 mm x 20 mm x 5 mm, were selected as the primary materials to be welded. The metallographic and mechanical testing of the base metals were performed as described in Chapter 3. The specimens were linear friction welded using center-driven LFW equipment (Model Number; 8AT2020A00, TOYO KOGYO) as shown in Fig. 3-2 in Chapter 3. The joints were fabricated under different applied pressures of 100 MPa and 300 MPa, determined based on the temperature dependence of the UTS of the base metals as discussed later, at the forging

speed of 5 mm/s. Forging speed refers to the pressing speed of materials along the length during LFW process. The oscillation frequency and oscillation upset were kept constant at 50 Hz and 5 mm, respectively. LFW was further conducted keeping an objective applied pressure of 300 MPa with different forging speeds of 5 mm/s, 10 mm/s, and 20 mm/s.

4.3. Results and discussion

4.3.1. Temperature dependence of base metals and relation between applied pressure

Fig. 4-1 shows the temperature dependence behavior of UTS of mild steel and A7075 evaluated by high-temperature tensile test. A7075 is composed of Al-Zn-Mg-Cu system, and its strength is mainly controlled by the presence of strengthening precipitates [113]. In addition, the melting point is about 660℃ (933 K), and the material softens rapidly at about 200℃. In contrast, mild steel is not strengthened by precipitates, so there is almost no reduction in strength at temperatures below 400℃. As a result, the UTS of mild steel and A7075 are reversed at room temperature and high temperature, and the curves expressing the temperature dependence of UTS have an intersection point (cross-point) around 220℃－300 MPa. In the case of 100 MPa applied pressure, according to the temperature dependence, A7075 started to deform when the interface temperature exceeded ～320℃ because the strength of A7075 dropped below the applied pressure (100 MPa). On the other hand, corresponding to ～320℃ strength of steel is maintained quite high as compared to A7075. Therefore, to facilitate deformation towards steel side at this temperature (～320℃), the minimum required applied pressure is ～290 MPa which is moderately higher than 100 MPa. As a result, only A7075 is ejected as flash without interfacial deformation on steel side during burn-off and forge phases. In the case of 300 MPa applied pressure, mild steel and A7075 are expected to deform

simultaneously when the temperature reached to ~220℃. Therefore, the applied pressure of 300 MPa was selected as the optimum one in this study, and the applied pressure of 100 MPa was for comparison.

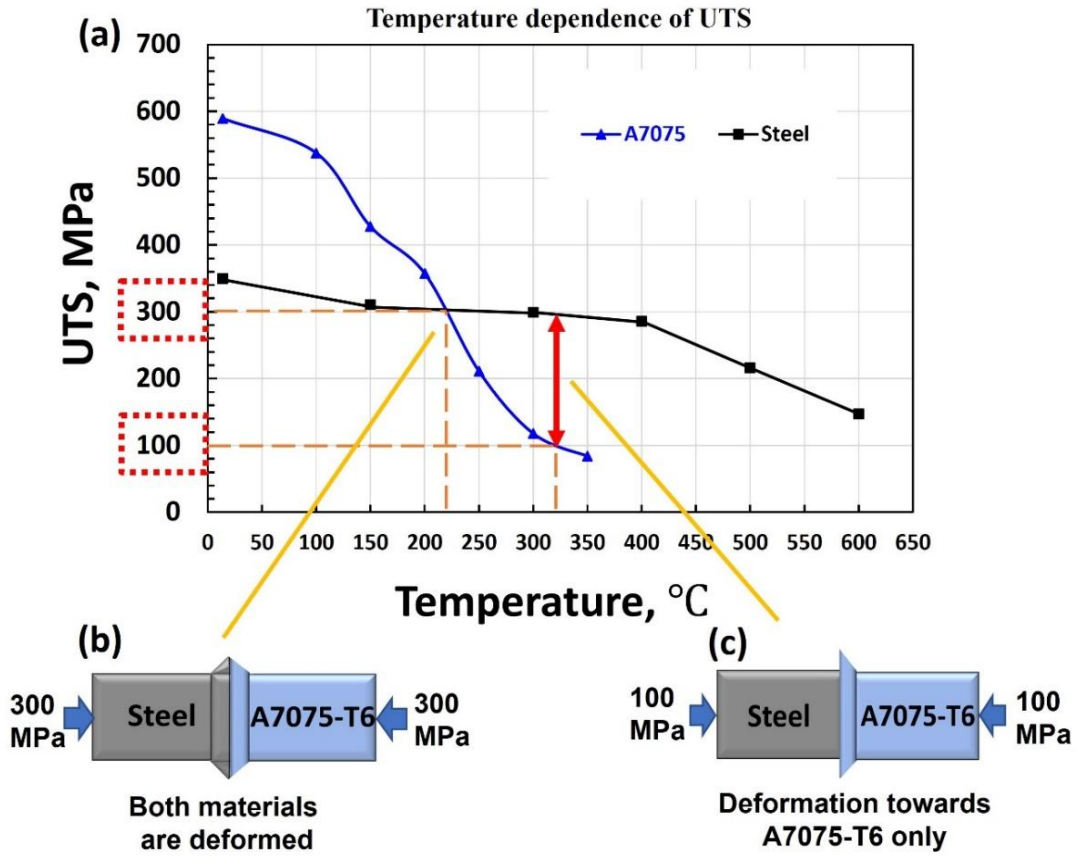

Fig. 4-1 (a) Thermal dependence behavior of ultimate tensile strength of mild steel and A7075, and the schematic illustrations of relationship between applied pressure and materials deformation during LFW at (b) 300 MPa, (c) 100 MPa applied pressure.

4.3.2. Forging speed and its relation to welding time

Figs. 4-2a and b show the graphs of upset stroke, and required welding time, respectively, during the LFW of the joints fabricated at different forging speeds of 5 mm/s, 10 mm/s, and 20 mm/s under an objective applied pressure of 300 MPa. Upset and oscillation frequency were kept constant at 5 mm and 50 Hz, respectively. The welding was completed as soon as the designated upset of 5 mm was achieved as shown in Fig. 4-

2a. The required welding time rapidly decreased as the forging speed increased, Fig. 4-2b. It is observed that the required welding time is lowest at a forging speed of 20 mm/s. Additionally, the weld completion time of 20 mm/s joint is just 0.4 s, whereas the time taken for the joints fabricated at 10 mm/s and 5 mm/s forging speed was observed to be 0.76 s and 1.18 s, respectively. Recently, significant conclusions have been provided to obtain sound welding of A7075 alloys by utilizing the highest possible welding speed in order to reduce the welding time [124], as the faster the welding speed, the less time the weld is in hot cracking range [40,124]. Moreover, it is noteworthy that shortly after the completion of the A7075/steel joining, a noticeable discontinuous cracking sound can be heard, particularly under certain specific joining conditions. This cracking sound is attributed to the thermal contraction experienced during the solid-state cooling of A7075. A7xxx has been recognized as one of the Al alloy series most susceptible to thermal residual stresses[125]. While this cracking sound can be noticeably heard in the weld fabricated at 5 mm/s and 10 mm/s forging speed. In contrast, it was effectively suppressed in joint fabricated at higher forging speed of 20 mm/s.

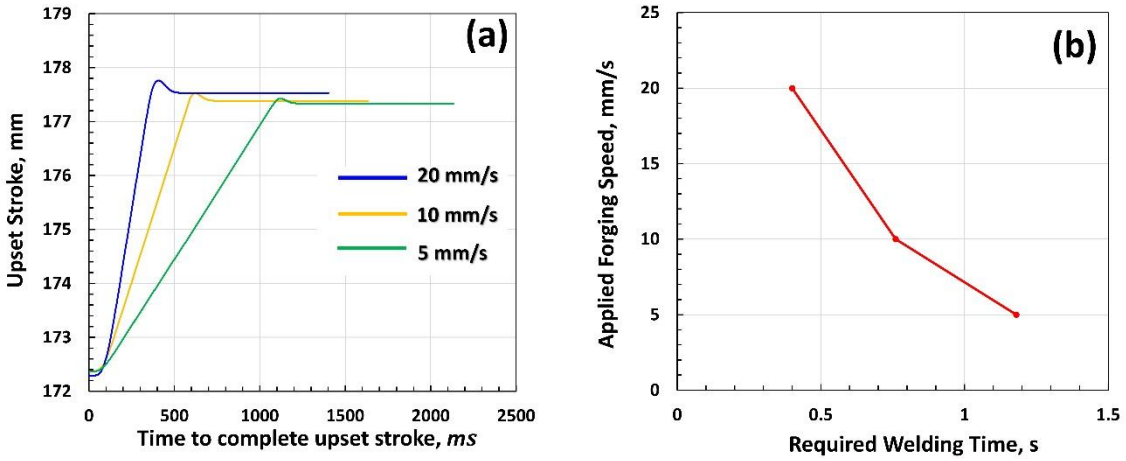

Fig. 4-2 (a) Relationship between upset stroke and time required to complete the upset at different forging speeds of 5 mm/s, 10 mm/s, and 20 mm/s, (b) corresponding required welding time at respective forging speed.

4.3.3. Joint appearance

Figs. 4-3(a-d) show the joint appearance of the welds obtained at different applied pressure of 100 MPa and 300 MPa with forging speeds ranging from 5 mm/s, 10 mm/s, and 20 mm/s, respectively. A7075 consistently displayed significant interfacial deformation during weld fabrication process. The extent of deformation towards steel side is shown by the blue dotted lines in Fig. 4-3(a-d). It is noteworthy that the weld fabricated at an applied pressure of 100 MPa exhibited almost no interfacial deformation towards the faying surface of steel. In contrast, A7075 experienced severe interfacial deformation during welding as shown in Fig. 4-3a. This finding was attributed to the fact of the notable difference in strength between mild steel and A7075 as shown in Fig. 4-1a. Because steel showed no interfacial deformation during welding, it is possible that oxides and rugged surfaces may have persisted at the joining interface [19]. On the other hand, at 300 MPa applied pressure, the deformation mode near the faying surface of mild steel was changed with the increased forging speed. At a forging speed of 5 mm/s and 10 mm/s, steel exhibited gradient deformation in which the deflection gradually decreases with increasing distance from the joint interface as shown in Figs. 4-3b and 4-3c. In contrast, A7075 again exhibits severe interfacial deformation almost same with 100 MPa case. It is noteworthy that at 20 mm/s forging speed, steel experienced significant interfacial deformation that resulted in a uniform ejection of flash perpendicular to the upset direction of specific range of material in the vicinity of the butt interface simultaneously with A7075 without gradual deflection, Fig. 4-3d.

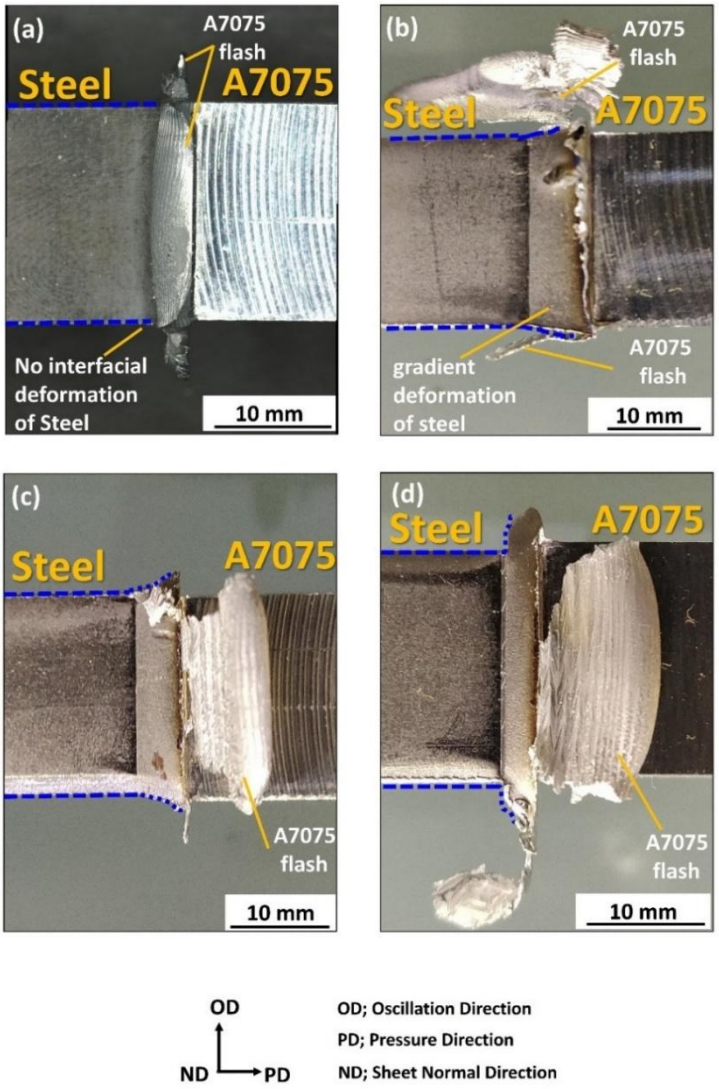

Fig. 1-3 Appearance of longitudinal cross sections of the joints fabricated at an applied pressure of (a)100 MPa with 5 mm/s forging speed, (b) 300 MPa with 5 mm/s forging speed, (c) 300 MPa with 10 mm/s forging speed, (d) 300 MPa with 20 mm/s forging speed.

4.3.4. Joint tensile strength and fractured tensile specimen

Tensile tests were conducted to evaluate the tensile strength of the obtained joints. The testing direction was perpendicular to the direction of the weld line, and the tests were performed at a cross-head speed of 1 mm/min. The tensile specimens were taken as shown in the schematic Fig. 4-4c after removing flash. The weld obtained at 100 MPa exhibited a joint strength of ~92 MPa. The much lower joint strength at an applied pressure of 100 MPa can be attributed to the absence of interfacial deformation towards

faying surface of steel during welding which leads to partial joining of weld interface as discussed later. Whereas the joint fabricated at an applied pressure of 300 MPa under forging speeds of 5 mm/s and 10 mm/s showed a bit improvement in the joint strength and exhibited a tensile strength of ~109.2 MPa and 170.7 MPa as shown in Fig. 4-4a. However, the weld strength is still far below than that of the steel BM (347 MPa). In contrast, joint fabricated at 300 MPa under 20 mm/s revealed an average tensile strength of ~347.1 MPa comparable to that of the steel BM. Additionally, Fig. 4-4b shows the fractured tensile specimens after the tensile test. The fracture location and weld interfaces are denoted by double-sided red and blue arrows, respectively. The joints fabricated at lower forging speeds of 5 mm/s and 10 mm/s exhibited an interfacial fracture. In contrast, the weld produced at a forging speed of 20 mm/s showed a tensile strength equivalent to that of steel BM revealing 100 % joint efficiency with respect to softer steel compared to harder Al alloy and exhibited a base metal fracture towards the steel side.

Fig. 4-5 shows the joint efficiency of dissimilar weld between precipitation-strengthened A7075 and steel weld achieved so far employing friction welding methods such as direct rotary friction welding [35,121,126-128]. The current research is indicated by the red-dotted lines in Fig. 4-5. The weld joints obtained previously suffer from poor joint efficiency and several joint defects such as interface cracking that reached to the weld interface [121]. In the current study, the tensile strength of the joint obtained by using LFW method was equal to the steel base metal, which exhibited 100 % joint efficiency with respect to steel. It is indeed surprising to achieve such a highly efficient dissimilar joint between steel and A7075. To the best of author's knowledge, this is the first time to achieve 100 % joint efficiency of steel and A7075 dissimilar joint employing LFW method and exhibiting a base metal fracture towards steel side.

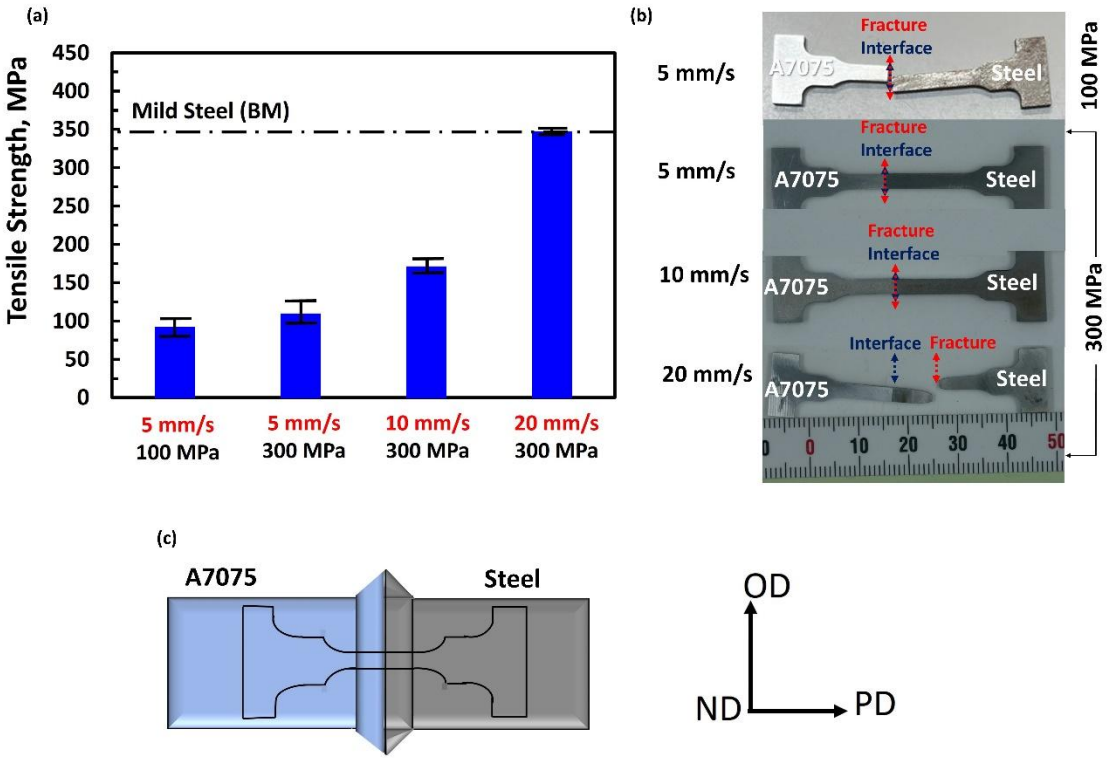

Fig. 4-4 (a) Tensile strength of the obtained joints, (b) fractured tensile specimen of the weld fabricated at different forging speeds and applied pressure, (c) schematic and location of tensile test specimen.

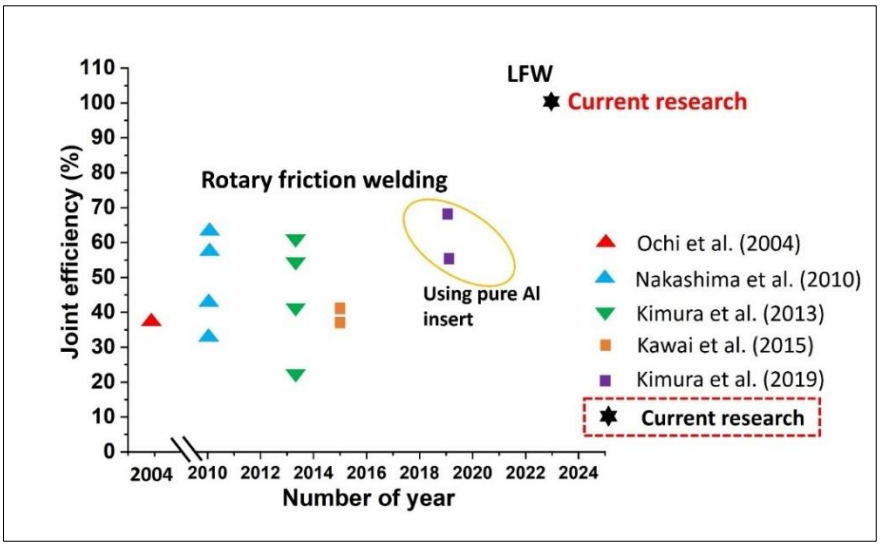

Fig. 4-5 Joint efficiency of dissimilar A7075/steel weld achieved so far using other pressure-controlled solid-state welding method (Rotary Friction Welding). Joint efficiency obtained in the current research is indicated by red-dotted rectangle.

4.3.5. Microhardness distribution

Fig. 4-6a shows the Vickers hardness distribution, as a function of distance from the weld center line, of the obtained joints. The lowest hardness values in each joint were consistently observed towards the steel side, which coincides with the fracture location of the 20 mm/s joint that exhibited the highest strength in the tensile test. Regardless of the forging speed employed, all joints exhibited a notable increase in microhardness near the joint interface towards steel side presumably due to work hardening, because the expected interface temperature of ~320 ℃ is too low for steel to dynamically recrystallize. As a result, deformed, but recovered microstructure in the joint interface toward steel was confirmed as shown in Fig. 4-6b. The peak hardness value of ~211 Hv was observed at a forging speed of 20 mm/s near the joint interface towards steel side. On the other hand, the A7075 BM was in T6 heat-treated condition. It is well known that by T6 heat treatment of A7075 Al alloys, artificially new precipitates form in the microstructure, thereby enhancing strength. However, in the hardness distribution curve towards A7075, all joints exhibited a noticeable decrease in hardness when moving from A7075 base material toward the joint interface, despite the grain refinement caused by dynamic recrystallization as shown in Fig. 4-6c. This reduction indicates the formation of a softening zone near the joint interface. It is primarily due to the dissolution or coarsening of hardening particles under the thermal and mechanical effects of the LFW process. Notably, average hardness value in the softened region was slightly improved at higher forging speed of 20 mm/s compared to 5 mm/s and 10 mm/s. Therefore, it is potentially a positive sign to partially suppress the softened region at comparatively higher forging speed when considering welding A7075 with other types of high-strength steel alloys. It is worth noting that despite the occurrence of softening towards A7075, in case of the

joint fabricated at 300 MPa applied pressure with 20 mm/s forging speed, the fracture was located in the steel base metal because the lowest microhardness in softened region was always maintained above the base metal hardness of steel. This can be attributed to the remained precipitates in softening zone and reprecipitation during cooling process.

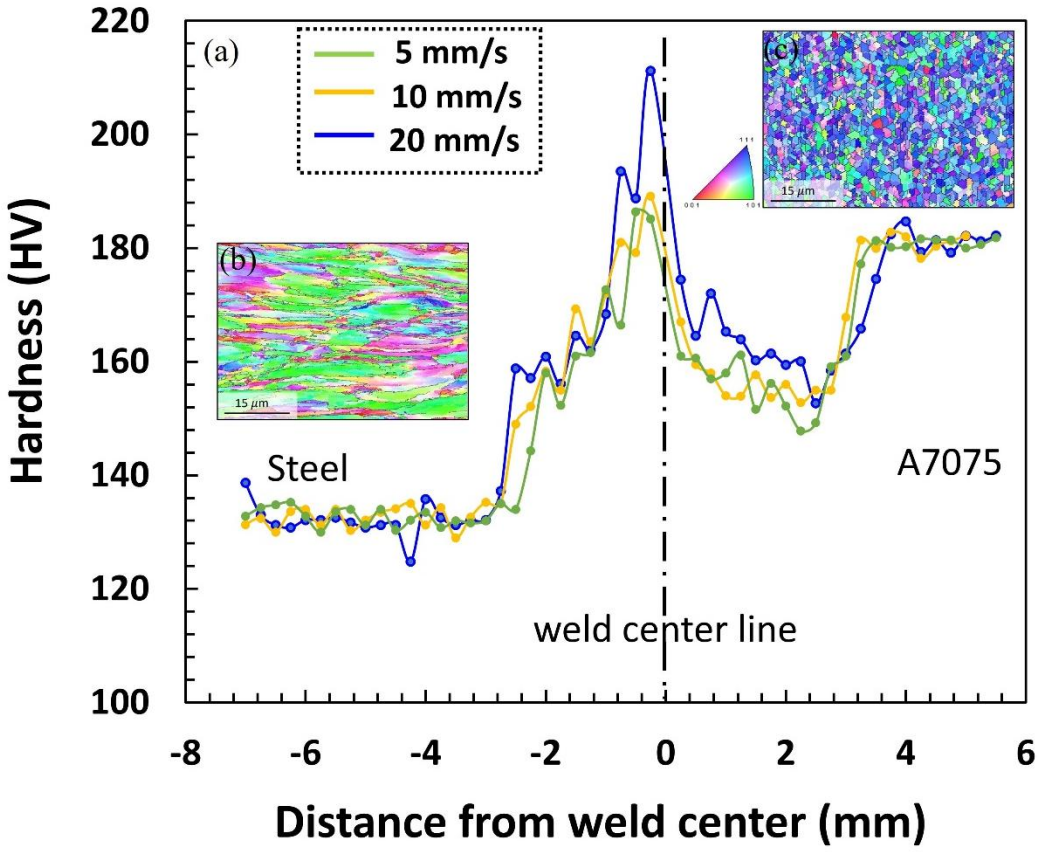

Fig. 4-6 (a) Microhardness distribution across the interfaces of the fabricated joints, electron backscatter diffraction-inverse pole figure (EBSD-IPF) maps near the joint interface towards (b) steel side and (c) A7075 side.

4.3.6. Joint interface macrostructure analysis

Fig. 4-7(a-h) shows the SEM images of the cross-section of fabricated joint interfaces. The presence of any weld defects and un-bonded areas were identified. Fig. 4-7a shows the joint interface fabricated at lower forging speed of 5 mm/s with an applied pressure of 100 MPa. The un-bonded joint interface is indicated by red arrows in Fig. 4-7a. Several un-bonded spots were identified throughout the weld interface including

towards the edge of the weld as shown in Fig. 4-7e. Furthermore, Fig. 4-7(b-d) depicts the interface of the joints fabricated at an applied pressure of 300 MPa under different forging speeds of 5 mm/s, 10 mm/s, and 20 mm/s, respectively. Despite slight deformation of the steel side in appearance, as shown in Figs. 4-3b and c, the butt surfaces are greatly deformed and show uneven shapes, voids and un-bonded areas. These defects, as shown in the red dotted rectangle in Fig 4-7b, are presumably caused by the unevenness of the faying surfaces. Additionally, un-bonded areas were also observed towards the edge of the joint, indicated by a red dotted ellipse. In Fig. 4-7g, the interface line of steel/A7075 weld is indicated by the white arrows. Further, increasing the forging speed to 10 mm/s (Fig. 4-7c), the joint defects were significantly suppressed. The joint was obtained well bonded near the edge of the weld. However, the voids were observed near the center of the weld accompanying to unevenness of butt surface, as shown by the red solid rectangle in Fig. 4-7h. These un-bonded regions would have greatly reduced the joint strength. Further increasing the forging speed to 20 mm/s resulted in complete suppression of voids and cracks, leading to a sound dissimilar joint without any interfacial defects as shown in Fig. 4-7d. Additionally, it is noted that the weld interface fabricated at a comparatively high forging speed of 20 mm/s appears to be quite flat without any uneven segments. This difference in the flatness of the joint interface at low and high forging speeds can be correlated with the difference in the deformation mode on the steel side, as shown in Fig. 4-3, i.e., gradual deformation mode versus uniform flash ejection mode. In the uniform flash ejection mode, the steel and Al alloy simultaneously deform in parallel directions as flash, which is thought to result in the formation of a flat interface. In the gradual deformation mode, the deformation on the steel side is insufficient and uneven with the deformation on the Al side, leading to the formation of interface irregularities and un-

bonded areas. The reasons why the forging speed affects the interface deformation mode will be discussed in section 4.3.7. The presence of un-bonded areas observed in low applied pressure or low forging speed conditions is considered to be the main reason for the significant decrease in tensile strength of the welding interface. Thus, it is clear that the formation of a flat joint interface with uniform flash ejection mode is effective for obtaining sound dissimilar steel/Al LFW joints.

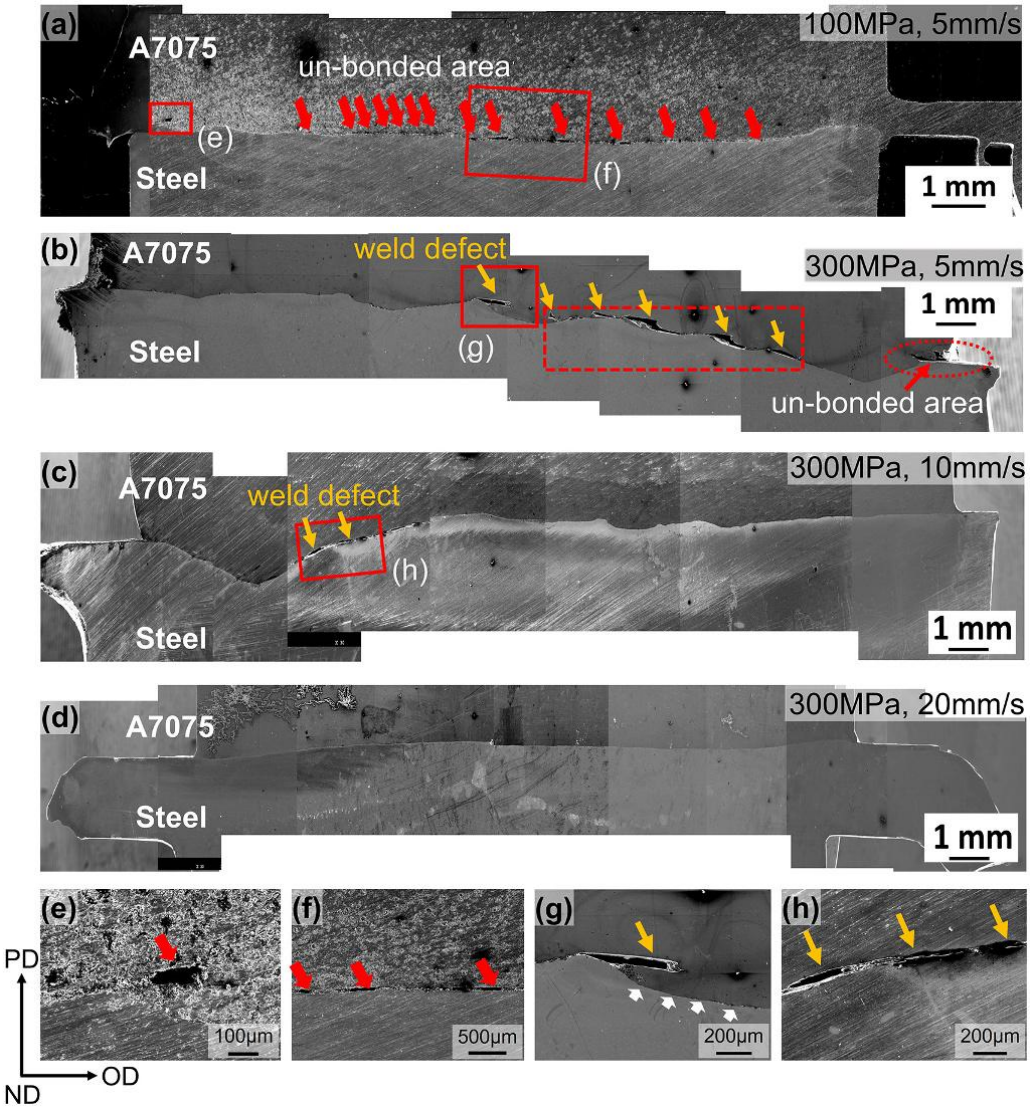

Fig. 4-7 SEM images of the weld interface of the joints fabricated at 100 MPa and 300 MPa applied pressure with different forging speeds of 5 mm/s, 10 mm/s, and 20 mm/s.

4.3.7. TEM analysis of the interface and mechanism for improving bonding strength by increasing forging speed

The mechanism for improving the joining strength by increasing forging speed is discussed in this section. Fig. 4-8 shows the TEM images and corresponding TEM-EDS line analysis of the interfaces of fabricated joints. The formed IMC layers are bordered with solid white lines at all the joint interfaces, as shown in Figs. 4-8(a-i), (b-i), and (c-i). At the lowest forging speed of 5 mm/s, the IMC layer was observed to be thick and irregular in thickness (Fig. 4-8(a-i)). This irregularity in thickness of the IMC layer is thought to correlate with the inhomogeneous deformation of steel that causes unevenness of the bonded interface indicated in Figs. 4-7b. In contrast, relatively uniform layers of IMCs were identified throughout the joint cross-section at forging speeds of 10 mm/s and 20 mm/s as shown in Fig. 4-8(b-i), and (c-i), respectively. Additionally, the average IMC layer thickness was reduced from 132.3 nm to 105.7 nm as the forging speed was increased from 5 mm/s to 10 mm/s as indicated in Figs. 4-8(a-ii) and (b-ii), respectively. With a further increase of forging speed to 20 mm/s, an extremely thin layer of IMC with an average thickness of 34.7 nm was observed at the joint interface, Fig. 4-8(c-ii). It is worth noting that IMC layer experienced a reduction in thickness with the increase in forging speed during LFW. This reduction in IMC layer thickness with increased forging speed can be attributed to the fact that higher forging speed resulted in lower welding heat input due to shorter weld completion time. This is a similar effect of welding speed on IMC thickness, which was reported recently during FSW [40]. Namely, at a forging speed of 20 mm/s during LFW, the interfacial reaction takes place comparatively for a shorter time leading to a relatively thin IMC layer than 5 mm/s and 10 mm/s forging speeds. Yamagishi [129] also obtained sound rapid dissimilar joining between SUS304 and A5083 using extremely short welding time of less than 0.1 s utilizing spot forge welding method.

These results suggest that the high forging speed of 20 mm/s significantly reduced the IMC layer thickness due to the extremely short weld duration of 0.4 s and, thus resulting in the excellent tensile strength of the LFWed joint between mild steel and A7075.

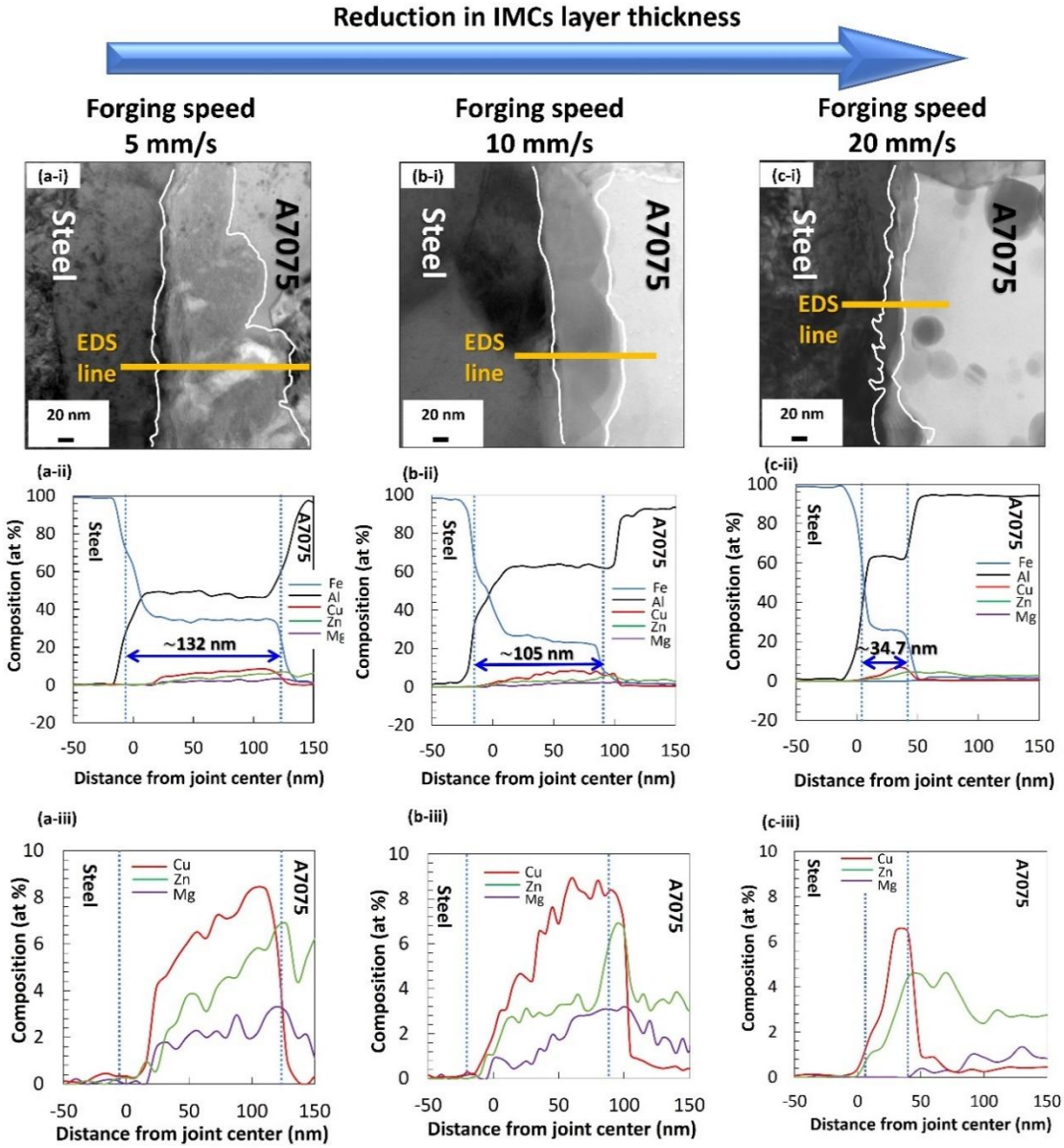

Fig. 4-8 TEM micrographs and EDS line scan results across the interfaces of joints fabricated at 300 MPa applied pressure and different forging speeds of 5 mm/s, 10 mm/s, and 20 mm/s.

Fig. 4-8(a-iii), (b-iii), and (c-iii) illustrate the detailed distribution of Cu, Zn, and Mg across the interfaces of weld produced at forging speeds of 5 mm/s, 10 mm/s, and 20

mm/s, respectively. The concentration of Zn at all the interfaces was observed to increase on moving from the initiation of IMC layer towards A7075 side and revealed peak concentration over 6 at. %, at IMC/A7075 interface, in the joints produced at 5 mm/s and 10 mm/s forging speed. Whereas in the case of joint produced at 20 mm/s, peak concentration of Zn at the IMC/A7075 interface was comparatively reduced and observed to be 4.8 at. %. On the other hand, Mg was only observed in the IMCs of the joints produced at 5 mm/s and 10 mm/s forging speed. Furthermore, similar to Mg and Zn, Cu also concentrated at the A7075/IMC interface with peak Cu concentration ranging from 6.4-8.5 at % in all the joint interfaces which is much higher than Cu concentration in A7075 base metal. It is noteworthy that the interface of the specimen fabricated at forging speed of 20 mm/s exhibits much lower concentration of Cu and Mg as compared with those of specimens fabricated at forging speeds of 5 and 10 mm/s. Liu and Fang [130] conducted a study focusing on the behavior of Zn, Mg, and Cu atoms and calculated the environment-sensitive embedding energies of these elements within the matrix and at the grain boundaries of an A7xxx alloy. The Cu atoms exhibited the highest environment-sensitive embedding energies, followed by Mg, while Zn atoms had the lowest. Notably, an inverse relationship exists between an element's solubility and environment-sensitive embedding energy. Consequently, Cu displayed the lowest solubility within the aluminum matrix compared to Mg and Zn atoms. On the other hand, according to Al-Cu binary phase diagram the solubility of Cu in Al increases with temperature [131]. Also, peak temperature in LFW joint during welding exist at the weld interface. Therefore, it is thought that relatively elevated temperature near the interface contributed to the segregation of Cu at the joints interface. Cu was identified as having the most detrimental effect on the hot cracking sensitivity of Al alloys during welding [132]. Additionally, albeit

to a lesser extent, presence of Mg was identified at the interface in the weld produced at 5 mm/s and 10 mm/s forging speeds. The suppression of segregation of these elements, which has a positive effect against hot cracking sensitivity of Al alloys owing to the short welding time, may also contribute to the higher strength of the weld interface. Recently, almost similar effect of high welding speed, on element segregation, weld cracking, and IMC thickness was observed during FSW[40]. The suppression of hot cracking by increasing the forging speed is in good accordance with the fact that the sound of crack was clearly heard when the forging speed was 5 and 10 mm/s, but was scarcely heard at the forging speed of 20 mm/s. A significant reduction was observed in the IMC layer thickness with increase in the forging speed from 5 mm/s to 20 mm/s. The maximum IMC thickness was observed at the joint interface fabricated at lowest forging speed of 5 mm/s, followed by 10 mm/s and 20 mm/s, respectively. These results suggest that the high forging speed of 20 mm/s significantly reduced the IMC layer thickness and concentration of Cu and Mg at the interface due to the extremely short weld duration of 0.4 s and promoted the simultaneous interfacial deformation of both alloys during LFW without the formation of the voids and cracks at the joint interface, as discussed above, thus resulting in the excellent tensile strength of the LFWed joint between steel and A7075.

4.3.8. TEM analysis of Al alloy and mechanism for the suppression of HAZ softening by increasing forging speed

Since the formation of precipitates plays an important role in the strength of A7075, examination of precipitates is needed in terms of their shape, size and distribution density in the interface region of Al side. Therefore, transmission electron microscope (TEM) analysis was conducted to gain further insights into hardness distribution and the occurrence of the softened region towards A7075. Fig. 4-9(a-c) shows the TEM images

of the A7075 BM and the softened area of the weld fabricated at a forging speed of 20 mm/s and at an applied pressure of 300 MPa. Fig. 4-9a shows the presence of spherical precipitates in A7075 BM as indicated by the black arrows. Based on TEM observation, the precipitates were uniformly distributed, on the order of 60-90 nm in size, throughout the matrix. The magnified image of red dotted region (b) in Fig. 4-9a is shown in Fig. 4-9b, and it revealed a uniform distribution of another very fine precipitates throughout the matrix. Additionally, a narrow precipitate-free zone (PFZ), approximately 30 nm wide, was identified along the grain boundaries. Furthermore, Fig. 4-9c illustrates the TEM image of the softened region of the obtained weld, located 2 mm away from the weld center. In this region, TEM investigation revealed the complete dissolution of very fine precipitates due to the elevated temperatures during LFW. Moreover, the distribution of spherical precipitates, similar to those in the BM, was also observed in the matrix along with rod-shaped precipitates, as indicated by red arrows in Fig. 4-9c. The existence of rod-shaped precipitates indicates that the precipitates within the base metal had undergone partial dissolution due to elevated temperature during LFW, followed by reprecipitation during cooling, a phenomenon consistent with prior research findings [107]. It was thought that the cooling rate was such that the coarser precipitates could nucleate and grow, but the finer ones could not nucleate. In other words, in the range of joining conditions used in this study, the softening in HAZ of A7075 is suppressed by decrease of heat input. This is consistent with the noticeable suppression of HAZ softening of the joint at a forging speed of 20 mm/s, where the required welding time is short and the heat input is small, as shown in Fig. 4-2b.

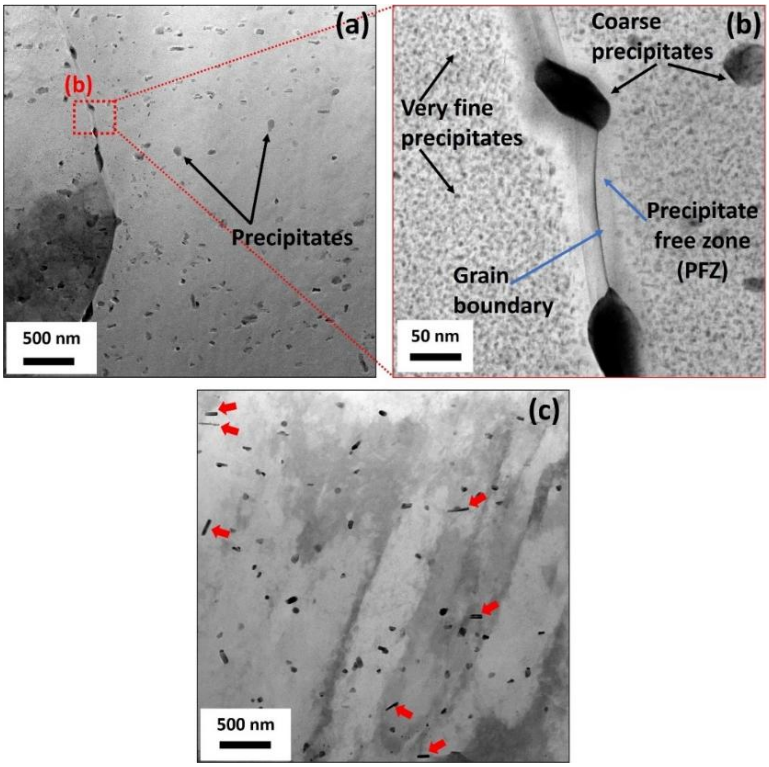

Fig. 4-9 TEM micrographs of (a) A7075 BM, (b) Magnified image of red dotted square in (a), (c) softening zone of weld fabricated at an applied pressure 300 MPa and forging speed of 20 mm/s.

4.4. Conclusion

Sound dissimilar LFW joint between A7075 and mild steel was successfully obtained based on the optimization of applied pressure and forging speed. The influence of the weld parameters on mechanical properties, joint interfacial macrographs, and joint microstructure was investigated. The obtained results are concluded as follows.

(1) An applied pressure of 100 MPa and 5 mm/s forging speed was found effective to facilitate interfacial deformation towards A7075 only, whereas no interfacial deformation towards the faying surface of steel was identified during welding due to the huge difference in the strength between mild steel and A7075.

(2) When the applied pressure was 300 MPa, corresponding to the cross-point strength of both alloys, at lower forging speeds of 5 mm/s and 10 mm/s, faying surface of steel experienced gradient deformation. Therefore, obtained welds exhibited poor

joint strength due to the formation of uneven joint interface, which leads to occurrence of several weld defects and un-bonded regions at the joint interface.

(3) Higher forging speed of 20 mm/s was found effective to completely suppress the joint defects by promoting simultaneous interfacial deformation of both alloys during welding, which led to a sound joint with quite flat joint interface without any interfacial un-bonded areas.

(4) IMC layer thickness was observed to be reduced with the increase in forging speed. At an applied forging speed of 20 mm/s, extremely thin layer of IMC, with an average thickness of 34.7 nm, was identified at the joint interface. Furthermore, the enrichment of Cu and Mg in the interface was also suppressed. Higher forging speed reduced the required welding time and duration of heat, which eventually reduced the heat input during welding. Therefore, the simultaneous interface plastic deformation of both alloys without the formation of voids and cracks became possible.

(5) Weld fabricated at an applied pressure of 300 MPa and 20 mm/s forging speed revealed excellent joint strength exhibiting 100 % joint efficiency with respect to steel. The fracture was located in the base metal region of steel.

Chapter 5: Center-driven double-sided LFW of SS400 steel and A7075 Al alloy using mild steel as center material

In Chapter 4, sound dissimilar direct LFW of mild steel and A7075 Al alloy was reported using a conventional LFW method. Where the joint strength was comparable to that of mild steel base metal and fracture was located in the base metal region of steel. Therefore, in this chapter a comparatively stronger steel, i.e., SS400 structural carbon steel, was selected to join with A7075 in order to achieve a stronger joint utilizing the innovative center-driven double-sided LFW (CDDS-LFW) method. The content of this chapter is majorly drawn from the published manuscript ‘‘Dissimilar joining of A7075 aluminum and SS400 steel utilizing center-driven double-sided linear friction welding using mild steel as a center material: Processing, mechanical and microstructure characterization’’ authored by Furkan Khan, Takuya Miura, Yoshiaki Morisada, Kohsaku Ushioda, Hidetoshi Fujii, *Journal of Manufacturing Processes,* 2025;139:67-80.

5.1. Introduction

Achieving simultaneous interfacial deformation of the mating materials during LFW is essential to form fresh surfaces and to obtain sound dissimilar joints. LFW is capable of facilitating simultaneous interfacial deformation of alloys by exploiting cross-point concept as clarified in Chapter 4. The primary objective of the present study is to obtain sound dissimilar joining between SS400 steel (hereinafter referred to as SS400) and A7075-T6 aluminum alloy (hereinafter referred to as A7075). Conventional direct LFW of SS400 and A7075 was proven challenging because of the absence of interfacial plastic deformation towards SS400 during joining process, which adversely affected the joint

strength. Therefore, CDDS-LFW is employed to effectively weld SS400 and A7075, with mild steel (hereinafter referred to as MS) used as the center material. Differing from conventional LFW method, CDDS-LFW is capable of simultaneously joining three different materials. In CDDS-LFW, oscillation mechanism is given in the center with two sides having the independent pressurization mechanism. The joining is accomplished by oscillating the center material between two side materials and applying pressure independently from each side. The applied pressures on each side were determined based on the cross-point concept after analyzing the thermal dependence behaviors of materials' strengths in order to promote the simultaneous interfacial deformation. Additionally, in this study, the mechanical and microstructure investigations were conducted at the center and edge of the obtained joints, as only a few studies have explored the microstructure and mechanical properties at the edges of LFW joints.

5.2. Materials and experimental methods

SS400 and A7075 specimens, each measuring 67 mm x 20 mm x 5 mm, were selected as the primary materials to be welded. MS was chosen as the center material. Chemical compositions (wt.%) and UTS of these base metals are shown in Table 3-1 in Chapter 3. Fig. 5-1 shows the microstructures of the base materials utilized in this study. Fig. 5-1a illustrates the microstructure of MS, showing a composition of ferrite and cementite. Meanwhile, the microstructure of SS400, depicted in Fig. 5-1b, consists of ferrite and pearlite. Microstructure of A7075 is depicted in Fig. 5-1c.

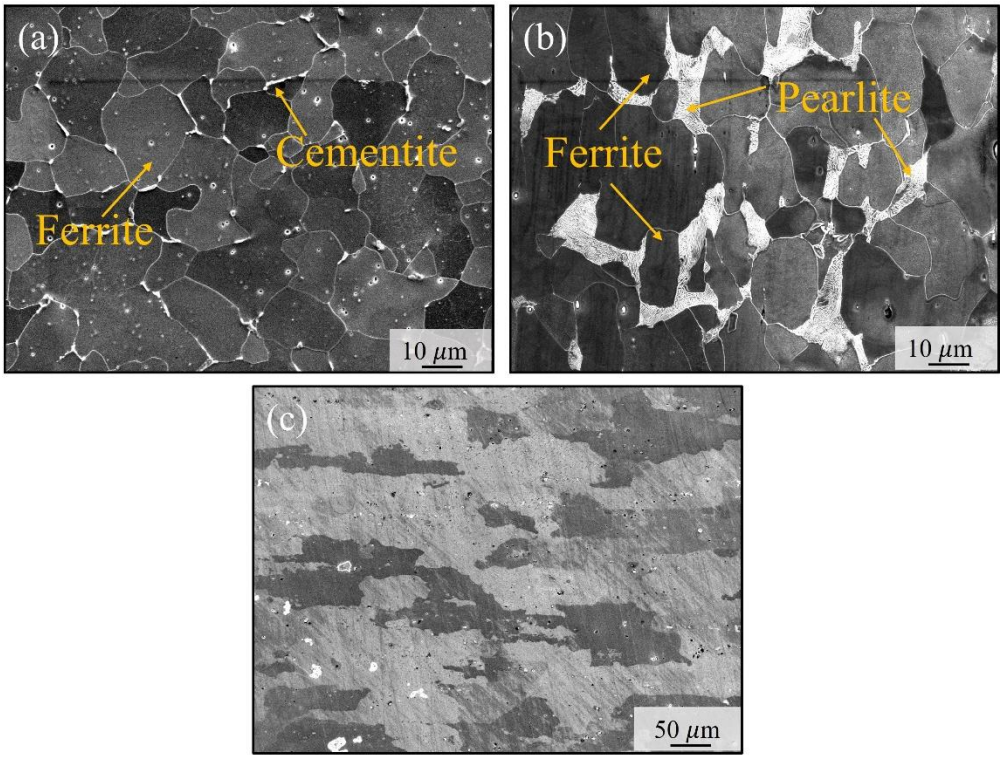

Fig. 5-1 Microstructure of base materials, (a) MS, (b) SS400, (c) A7075 alloy.

CDDS-LFW equipment (8AT2020A00, TOYO KOGYO) was utilized to fabricate the joints. Firstly, direct joining was performed between SS400/A7075 alloy at an applied pressure of 470 MPa with an upset value of 5 mm using a conventional LFW method. The reason for choosing an applied pressure of 470 MPa is explained in Section 5.3.2. Thereafter, CDDS-LFW for SS400/A7075 joint using MS as a center material was performed exploiting different applied pressures of 50 MPa and 300 MPa towards SS400 and A7075 side, respectively. The reason for selecting these values of applied pressures will also be given in Section 5.3.2. MS was selected as the center material because temperature dependent strengths of MS and A7075 possess cross-point, and MS also has a temperature at which material strength is almost equal to SS400. Additionally, the center material was cross-shaped to prevent lateral displacement caused by differences in the applied pressure on the left and right sides. The amplitude and oscillation frequency were

kept constant at 2 mm and 50 Hz, respectively, with an upset value of 5 mm on each side and an objective forging speed of 20 mm/s. The obtained weld consisted of two weld interfaces, SS400/MS and MS/A7075. It is worth mentioning that three replicates were produced under the identical welding conditions to ensure the consistency and repeatability of the LFW joint. During CDDS-LFW, thermal histories of weld were recorded by attaching a K-type thermocouple on the workpiece surfaces on both sides as illustrated later. The thermocouples were attached at the points on the specimen surface 3 mm far from the initial butt interface towards A7075, as A7075 was observed to be shortened by 3 mm during welding, and 1.5 mm towards SS400 as similarly SS400 was observed to be shorten by 1.5 mm during welding. Additionally, all the metallographic sample preparation and mechanical testing were performed as described in Chapter 3, except for the CDDS-LFW tensile specimen, which was extracted with a gauge section 40 mm long, 4 mm wide, and 2 mm thick.

5.3. Experimental setup and joining concept of CDDS-LFW

5.3.1. Experimental setup and joining process of CDDS-LFW

CDDS-LFW was utilized to overcome the challenges of welding dissimilar materials such as SS400 and A7075. Fig. 5-2 illustrates the CDDS-LFW setup, placement of specimens, shape and dimensions of the used specimens. The entire apparatus and an internal view of the joining unit are shown in Figs. 5-2a and b, respectively. The joining is accomplished by oscillating the center specimen between two side materials and applying pressure from both sides as shown in Fig. 5-2c. It is difficult to perform such simultaneous joining of two sides using conventional LFW equipment. Therefore, in this study, we have utilized novel joining equipment (8AT2020A00, Toyo Kogyo) with an oscillation mechanism in the center and pressurizing mechanisms on both sides.

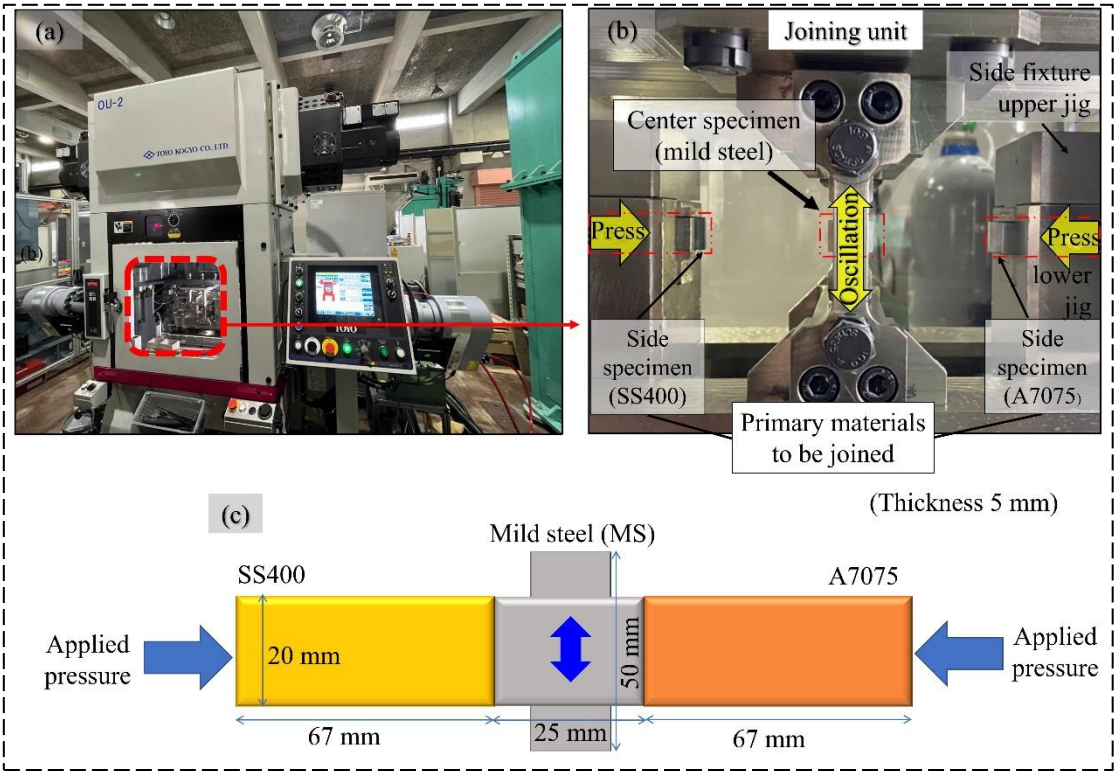

Fig. 5-2 Experimental setup of CDDS-LFW, (a) entire setup, (b) internal view of joining unit, (c) dimensions of the used specimens.

Fig. 5-3 explains the joining process of the CDDS-LFW method. CDDS-LFW typically comprises four phases. Initially, both side materials are brought in contact with the center material, stage 1 or contact phase in Fig. 5-3a. Further, during stage 2 or the conditioning phase in Fig. 5-3b, the center material is subjected to the oscillation motion at a preset oscillation frequency while both the side specimens are pressed against each side. Frictional heat is generated at both weld interfaces due to the relative frictional motion between all three specimens under an applied pressure. The generated frictional heat and load cause the materials to plasticize and deform at both interfaces. Furthermore, the combined effects of the applied load and specimen oscillation cause a significant amount of plasticized material to be expelled as flash from the weld interface during the burn-off phase (Fig. 5-3c) and the forge phase (Fig. 5-3d). This expulsion of material

helps remove surface oxides and impurities from the interface, exposing fresh metal surfaces and facilitating the formation of a strong joint. Additionally, the placement of K-type thermocouple on the workpiece surfaces on both sides is illustrated in Figs. 5-3a and d before and after completion of joining, respectively.

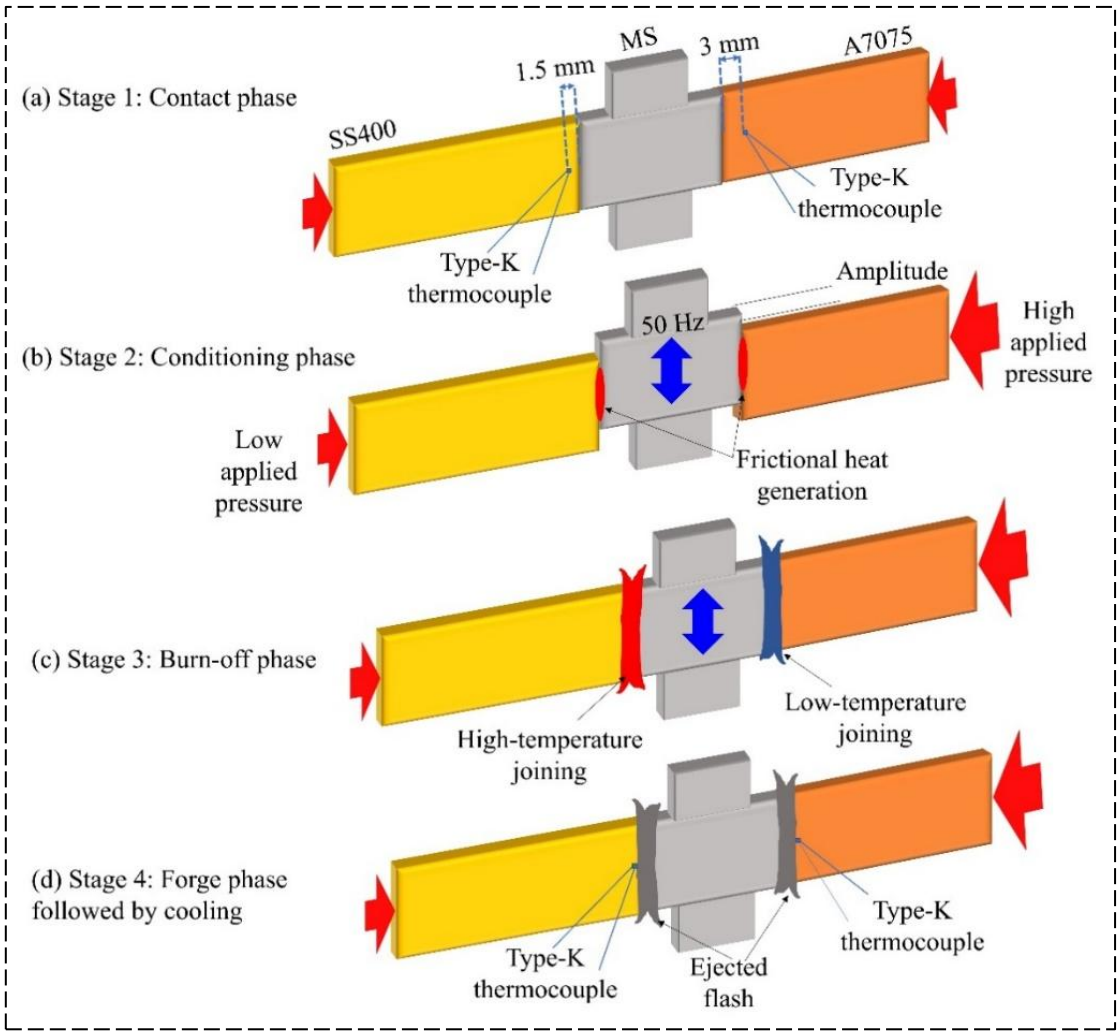

Fig. 5-3 Joining concept of CDDS-LFW method, (a) stage 1: contact phase, (b) stage 2: conditioning phase, (c) stage 3: burn-off phase, (d) stage 4: forge phase; and placement of K-type thermocouple for temperature measurement (a) before, and (d) after welding.

5.3.2. Cross-point concept in dissimilar LFW

Fig. 5-4 presents the temperature dependence of ultimate tensile strength (UTS) of A7075, SS400, and MS evaluated by conducting high-temperature tensile tests at several

temperatures starting from room temperature. The UTS of A7075 stands highest at 589 MPa at room temperature, followed by SS400 and MS exhibiting 482 MPa and 347 MPa, respectively. A7075 alloy is composed of Al-Zn-Mg-Cu, and its strength is primarily determined by the existence of finely dispersed strengthening precipitates[113]. Additionally, the alloy softens rapidly at about 200℃, resulting in a sharp decrease in UTS with an increase in temperature. On the other hand, UTS of MS and SS400 much more slowly decreases. As a result, the material strengths of A7075 and steels reversed at room temperature and high temperatures, and the curves expressing temperature dependence behavior of UTS for A7075 and MS have an intersection point (cross-point) around ~225℃ −300 MPa. Therefore, MS/A7075 were expected to deform simultaneously when the interface temperature exceeded the critical deformation temperature of 225℃ under an applied pressure of 300 MPa. On the other hand, MS and SS400 have almost equal strength of 50 MPa at ~780℃. Accordingly, SS400/MS were expected to deform simultaneously when the welding temperature exceeded the critical deformation temperature of 780℃. Therefore, a pressure of 300 MPa was applied at MS/A7075 interface, while 50 MPa was applied towards MS/SS400 to deform simultaneously as demonstrated in stage 3 in Fig. 5-3c.

It is noteworthy that the temperature dependence of strengths curves for SS400 and A7075 shows a cross-point at ~120℃ −470 MPa as indicated by the black dashed arrow in Fig. 5-4, suggesting the possibility of direct joining of SS400/A7075 using the conventional LFW method. Therefore, considering the possibility of direct joining between SS400 and A7075, conventional LFW was performed under an applied pressure of 470 MPa, which corresponds to the cross-point strength of both materials.

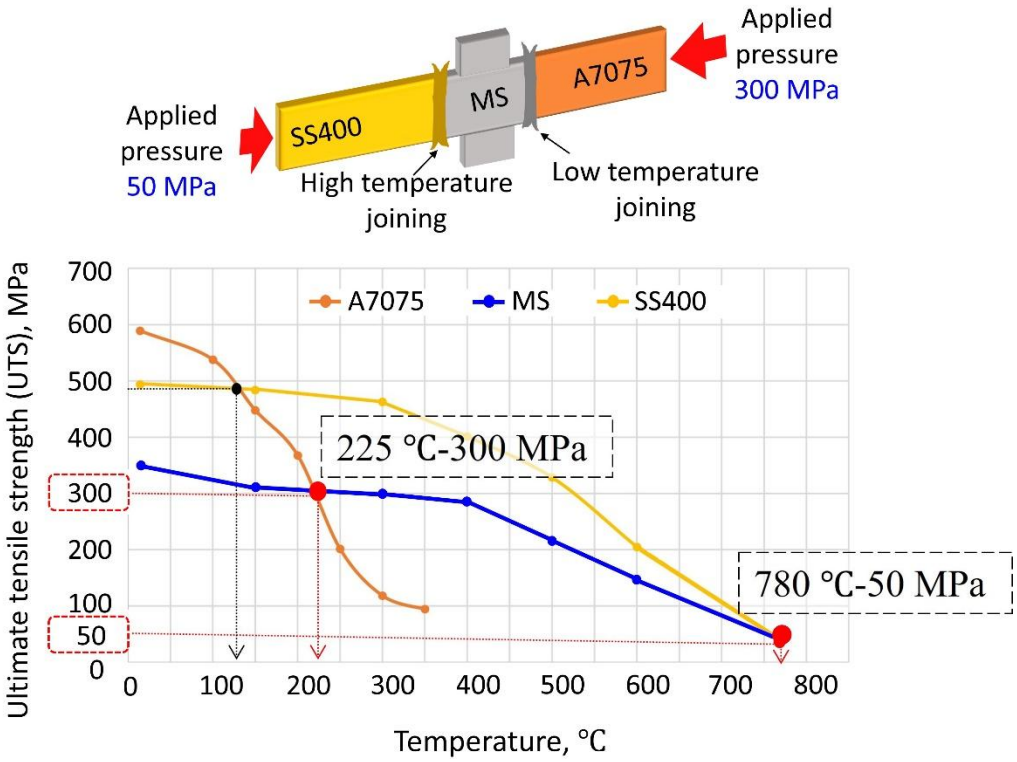

Fig. 5-4 Temperature dependence of UTS of SS400, MS, and A7075 alloys.

5.4. Results and discussion

5.4.1. Direct joining of SS400/A7075 using conventional LFW method

Fig. 5-5a shows the appearance of SS400/A7075 conventional LFW joint fabricated at an applied pressure of 470 MPa. During LFW, only A7075 was preferentially deformed, and no interfacial deformation occurred towards SS400. Therefore, burrs were not ejected from SS400 and impurities and oxides might have remained at the interface, leading to the occurrence of several un-jointed regions. Fig. 5-5b shows the fractured tensile specimen after tensile testing. The joint obtained using the conventional LFW method suffers from poor tensile strength and exhibited an average tensile strength of ~77.6 MPa with negligible elongation. Moreover, the joint revealed an interfacial fracture, as shown in Fig. 5-5b. The poor joint strength of conventional LFW may be attributed to the lack of interfacial deformation towards SS400, as poor interfacial plastic deformation can lead

to poor weld performance due to insufficient flash ejection.

The joint interface was thoroughly examined to detect any un-joined spots or weld defects. Figure 5-6 displays the SEM images of the SS400/A7075 joint interface. Figs. 5-6b and c represent the magnified SEM images of the solid-black rectangles in Fig. 5-6a. The un-jointed interface is indicated by red arrows in Figs. 5-6a, b, and c. SEM investigation revealed the presence of several un-jointed spots along the joint interface, including at the edge and near the center of joint. These un-jointed spots were presumably caused due to absence of interfacial deformation towards SS400 which might have persisted the impurities and oxides at the joining interface. The occurrence of these un-jointed areas greatly influenced the joining strength of the weld, making it extremely difficult to obtain a sound joint [71]. Therefore, these results confirm that, despite having a cross-point in the temperature-dependent strengths, it is extremely difficult to obtain a sound joint between SS400 and A7075 by using the conventional LFW method. The difficulty arise due to the cross-point which exists at a very low temperature of ~120°C. The strength of SS400 at 120 ℃ was quite enough to resist deformation and the temperature dependence of it is very small in this temperature range. Therefore, the formation of IMC was presumed to be extremely difficult.

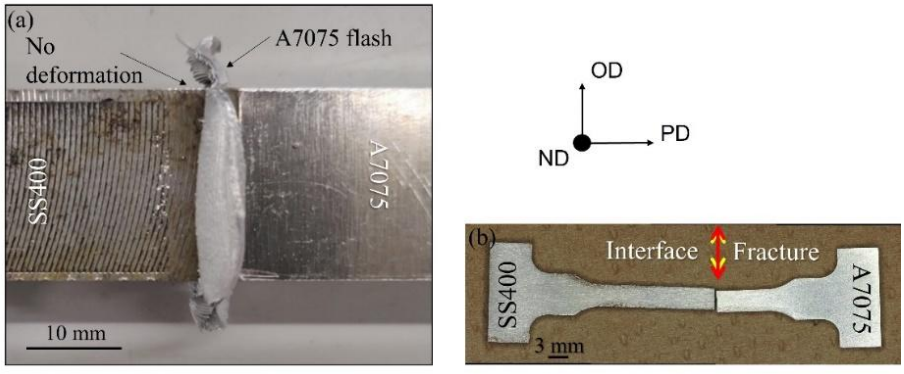

Fig. 5-5 (a) Joint appearance of SS400/A7075 using conventional LFW method, (b) fractured tensile specimen.

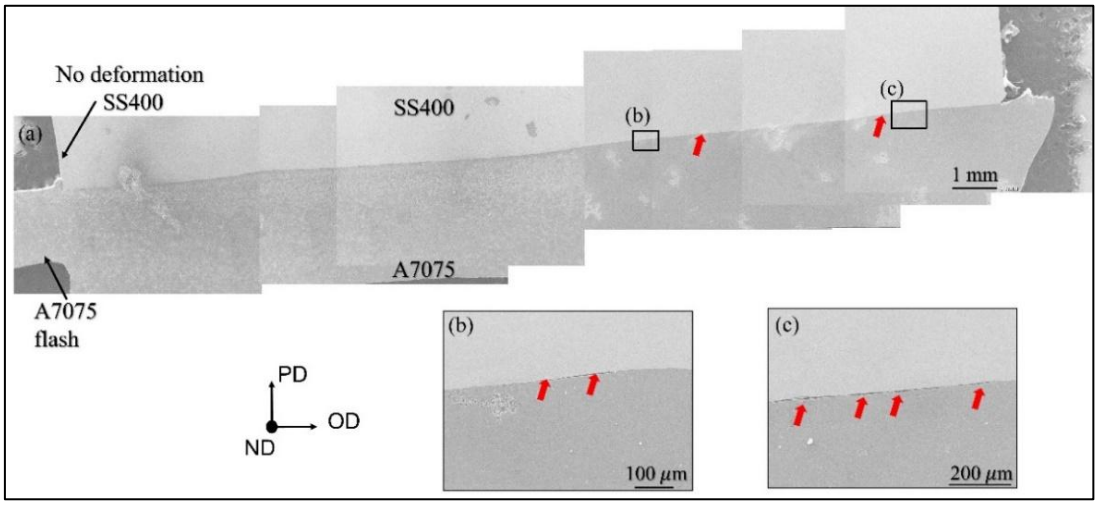

Fig. 5-6 (a) SEM macrograph of the SS400/A7075 weld interface, (b) and (c) magnified images of the solid-black rectangles in Fig. 5-6a.

5.4.2. CDDS-LFW of SS400/A7075 by using mild steel as center material

5.4.2.1. Weld appearance and thermal history of weld interfaces

Fig. 5-7 shows the appearance of the weld fabricated by using CDDS-LFW. Both weld interfaces, SS400/MS and MS/A7075, were severely deformed but generated different types of flash during welding. The dashed red rectangles b and c in Fig. 5-7a show the higher magnification images of SS400/MS and MS/A7075 weld interfaces as shown in Figs. 5-7b and c, respectively. The flash ejected from SS400 and MS are indicated by yellow and blue arrows, respectively. SS400 and MS both had undergone significant plastic deformation, forming ample amount of curled flash at the SS400/MS interface. On the other hand, A7075 was identified as generating a high amount of chip-like flash at the MS/A7075 interface, as indicated by white arrow together with the severely deformed MS as indicated by blue arrow in Fig. 5-7c. The differences in the flash morphology and deformation behavior of the materials at each weld interface can be well explained by the applied pressure, control of interface temperature and instinct properties of the materials. Sound joining was obtained by applying 300 MPa at MS/A7075 interface, and 50 MPa at MS/SS400 interface, corresponding to the respective

cross-point strength of materials. As a result, the flash simultaneously ejected at both the weld interfaces, facilitating a sound joining of all three materials.

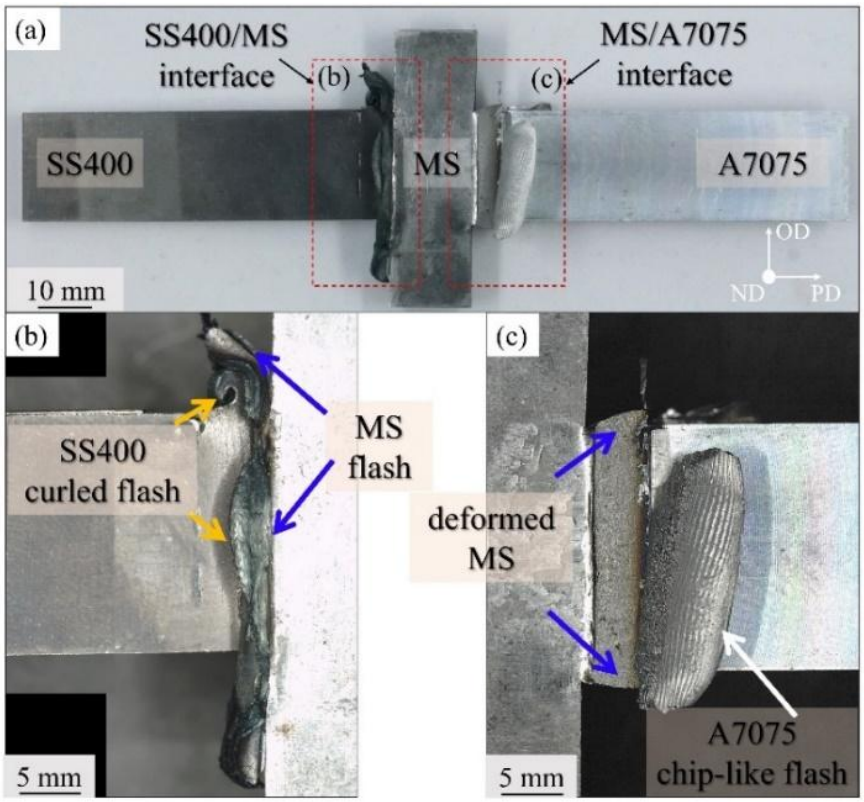

Fig. 5-7 Appearance of weld, (a) entire weld; higher magnification image of, (b) SS400/MS joint interface, (c) MS/A7075 joint interface.

Fig. 5-8 shows the weld thermal histories of SS400/MS and MS/A7075 interfaces. Evidently, the interface temperature increased rapidly at the very initial stage of CDDS-LFW. The temperature rapidly rose from room temperature to the peak temperature at both interfaces. Afterwards, the process of continuous cooling led to the temperature dropping to the ambient. At both the interfaces, there were obvious differences in the peak temperatures. The peak welding temperature at SS400/MS interface was recorded 842℃. On the other hand, the peak temperature at MS/A7075 was observed to be 321℃.

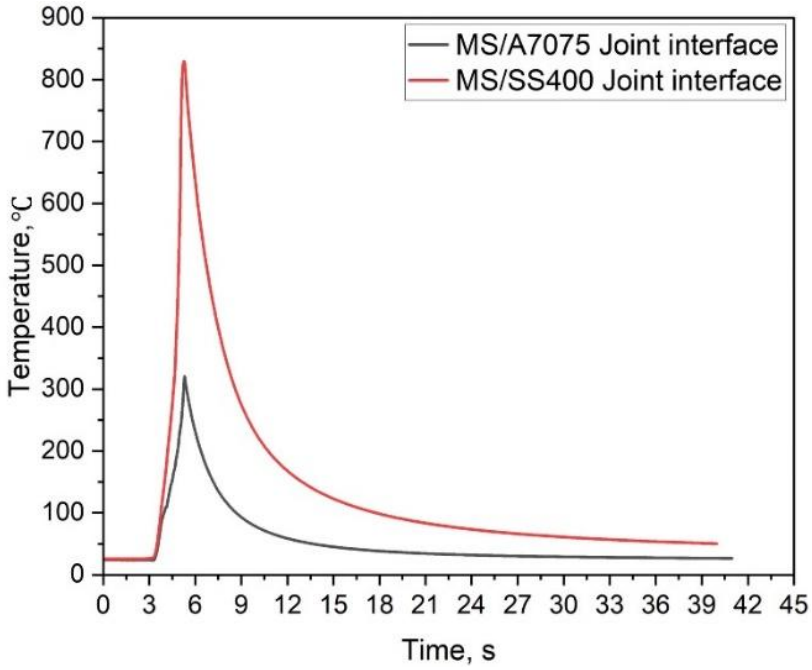

Fig. 5-8 Weld thermal history during CDDS-LFW at (a) SS400/MS joint interface, (b) MS/A7075 joint interface.

5.4.2.2. Mechanical performance of the CDDS-LFW weld

Joint tensile strength

To evaluate the joint strength of the fabricated welds, tensile tests were conducted at room temperature. The tests were performed both at the center and edge locations of the produced welds as shown in Fig. 5-9d. Fig. 5-9b compared the joint strength of the present study with the previously obtained dissimilar joints using solid state joining methods. Fig. 5-9a shows the stress-strain bar graph of the obtained welds at center and edge locations and compared with MS base metal. The joint revealed an average tensile strength of ~347.5 MPa and ~346.8 MPa with good ductility at the center and edge of the weld, respectively, revealing 100 % joint efficiency with respect to MS. Fig. 5-9c shows the fractured tensile specimen containing both the joint interfaces i.e., MS/SS400 and MS/A7075. The obtained weld exhibited a ductile fracture with necking in the base metal region of MS, far away from both the joint interfaces. The excellent joint strength of the weld can be attributed to the sufficient flash ejection and simultaneous interfacial

deformation of the mating materials during welding. The dissimilar weld joints of A7075 alloys with SS400 or other carbon steel alloy obtained by conventional LFW method and any other pressure-controlled solid state welding methods such as rotary friction welding (RFW), suffer from low tensile strength due to inhomogeneous interfacial deformation and cracks [121] and existence of thick and brittle IMC at the interface [35, 136]. Additionally, efforts were made to enhance the joint strength between carbon steel and A7075 by incorporating a pure aluminum (Al) interlayer during rotary friction welding [126]. However, the maximum joint strength achieved was approximately ~311 MPa which was still far from the base metal strength, and the joint strength began to decline when the applied pressure exceeded a certain value [126]. In contrast, the tensile strength of joints produced by the CDDS-LFW method was comparable to that of the base metal, and to the best of the author's knowledge, the present study revealed the highest joint strength of ~347.5 MPa so far concerning the joining of SS400 steel with any Al base alloy compared to other solid state joining methods. Also, as mentioned earlier, the produced weld revealed 100 % joint efficiency with respect to MS, and ~72 % and ~59 % with respect to SS400 and A7075 alloy, respectively. Although, in the present study, the joint efficiency is 100 % concerning MS, the joint strength is limited to the strength of the center material, i.e., strength of MS base metal. Therefore, the authors believe that a stronger joint may be obtained by systematically choosing a stronger center material.

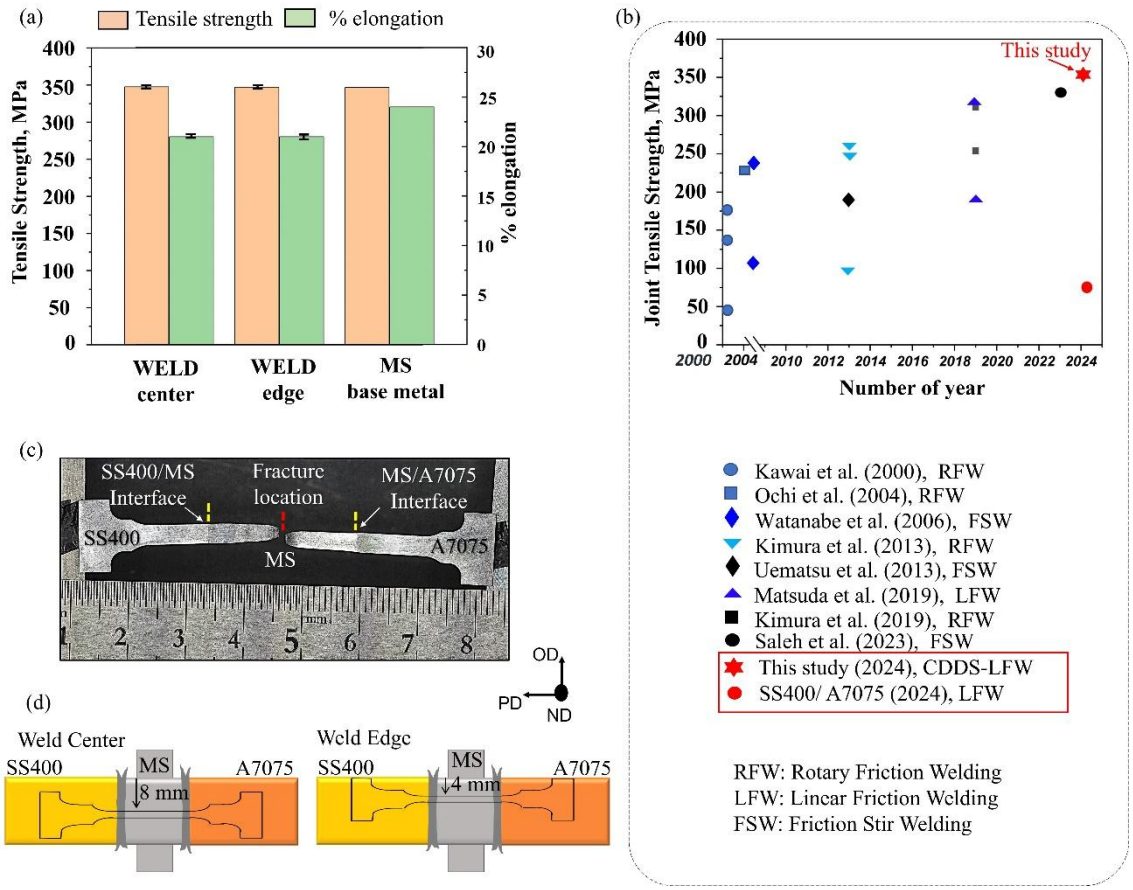

Fig. 5-9 (a) Tensile strength and % elongation of the dissimilar A7075/SS400 joint and MS base metal as a reference, (b) joint strength of steel/aluminum dissimilar welds achieved previously using other solid-state joining methods, (c) fractured tensile specimen showing fracture location at MS base metal, (d) schematic of the location of tensile test specimen.

Vickers Microhardness

Fig. 5-10 shows the Vickers microhardness distribution of the produced weld as a function of distance from the A7075/MS joint interface. Hardness measurements were performed both at the center location and 1 mm deep from the edge of the weld. Fig. 5-10b shows the macrograph of the hardness specimen. Apart from this, Figs. 5-10c and d shows TEM micrographs of A7075 BM and at a distance of 0.1 mm from the MS/A7075 joint interface towards A7075. The average hardness values of the base SS400, MS, and A7075 materials were 165 Hv, 120 Hv, and 182 Hv, respectively. Across the entire weld, the highest hardness was observed towards SS400 side near the SS400/MS joint interface.

The significant increase in hardness at SS400/MS interface can be attributed to the grain refinement by dynamic recrystallization during LFW together with the presence of martensite, transformed from austenite during cooling after LFW due to elevated temperature towards SS400/MS interface.

On the other hand, concerning microhardness distribution at the MS/A7075 joint interface, the hardness was observed to be rapidly increased near the joint interface towards the MS side with a peak hardness value of 191 Hv and 186 Hv at the center and edge locations, respectively. In contrast, on the A7075 alloy side, which is strengthened by the strengthening precipitates [113], the hardness experienced a sudden drop near the joint interface regardless of the measurement location. This resulted in a notable mismatch in hardness distribution at the MS/A7075 interface, characterized by a significant increase in hardness towards the MS side and a sudden drop towards the A7075 side. The significant increase in hardness towards MS can be attributed to the severe plastic deformation together with intense frictional heating near the joint interface during LFW, which leads to significantly reduced grain size with higher dislocation density near the joint interface, as depicted later in Fig. 5-14 (b-i), contributing in hardness. On the other hand, the sudden drop in hardness towards A7075 can be well explained by the TEM micrographs in Figs. 5-10c and d. The BM of A7075 was observed to be composed of very fine strengthening precipitates in addition to the larger precipitates, see Fig. 5-10c. Whereas, near the joint interface, scarce coarser precipitates were found in the softening region of A7075 but the very fine strengthening precipitates were not evident from TEM, see Fig. 5-10d, as the peak temperature may have exceeded the solvus temperature of these precipitates leading to dissolution of very fine precipitates. Hence, dissolution of very fine precipitates near the interface and growth of larger precipitates

due to the elevated temperature during welding led to a sudden drop of microhardness in this region. It is known that a significant hardness mismatch can cause stress concentration at the interface making it prone to crack initiation and propagation during loading. However, during tensile testing the fracture was located in the base metal region of MS far from the joint interface. This behavior is attributed to the presence of an extremely thin IMC layer at the MS/A7075 joint interface (as shown later in Fig. 5-15). The extremely thin IMC layer enhances the joint's integrity, making it sound and preferred for industrial applications.

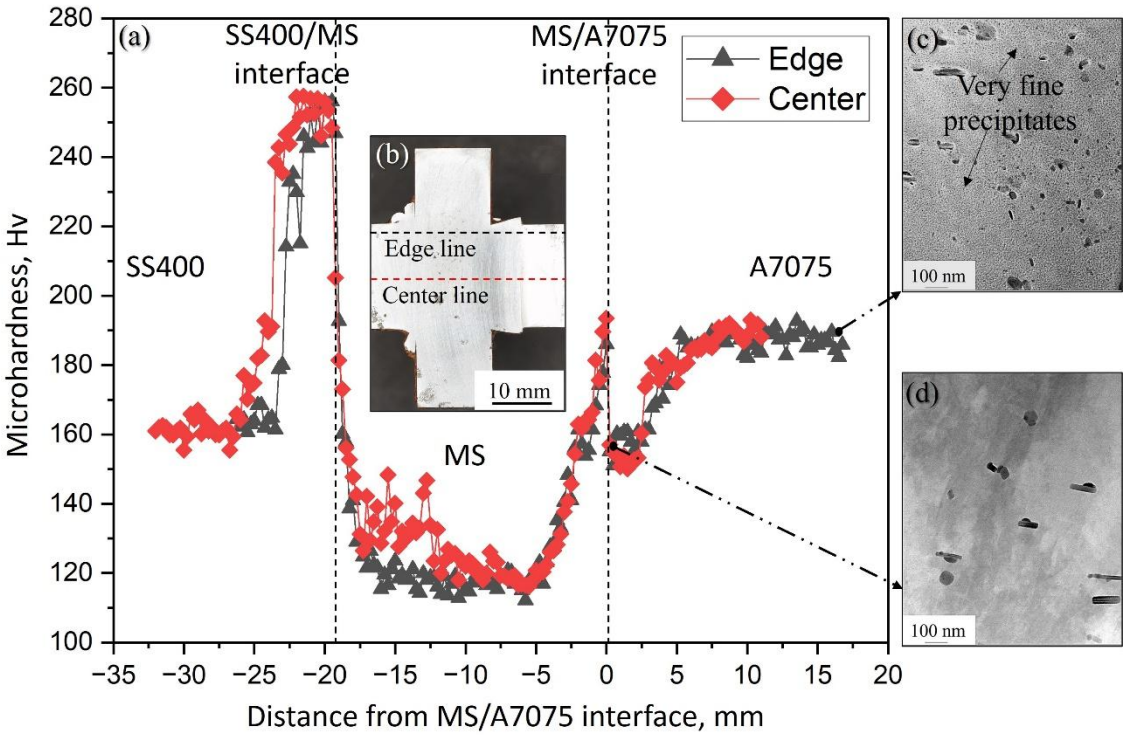

Fig. 5-10 (a) Microhardness distribution at the center and edge of the weld, (b) microhardness specimen, and TEM micrographs of (c) A7075 BM, (d) 0.1 mm from MS/A7075 interface towards A7075.

5.4.2.3. Macrostructure and Microstructure characterization

Figs. 5-11a and b show the cross-sectional SEM macrographs of the SS400/MS and MS/A7075 joint interfaces, respectively. Both the joint interfaces were investigated

thoroughly in order to identify the presence of any un-jointed spots and weld defects. Towards the SS400/MS interface, the flash was ejected from both MS and SS400 as indicated by black arrows. Figs. 5-11(a-ii) and (a-iii) show the magnified SEM images at the center and edge of the weld, respectively. No weld defects and un-jointed spots were identified throughout the weld interface, indicating a sound joining between MS and SS400. On the other hand, the interface SEM macrostructure of MS/A7075 is shown in Fig. 5-11(b-i). Additionally, Figs. 5-11(b-ii) and (b-iii) show the magnified SEM images towards MS/A7075 interface at the center and edge of the weld, respectively. SEM observation at MS/A7075 interface revealed the absence of any un-jointed spots throughout the joint interface, and the materials were observed to be soundly welded.

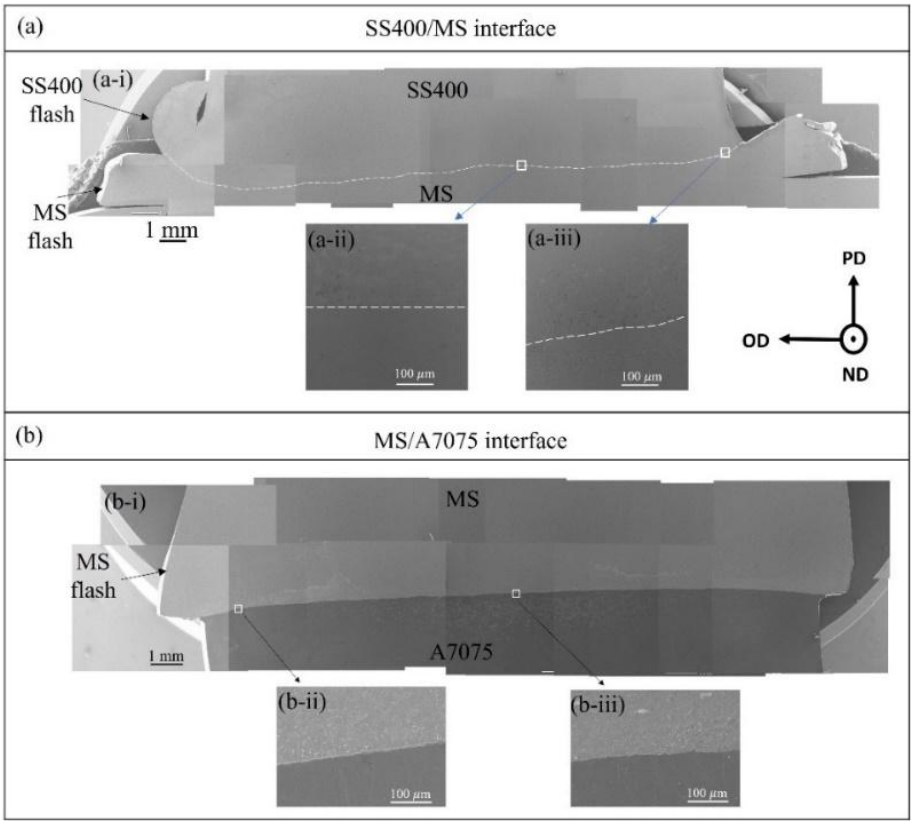

Fig. 5-11 Macrostructure of (a) SS400/MS joint interface, (b) MS/A7075 joint interface.

SS400/MS dissimilar steel joint interface

Figs. 5-12(a-d) show the typical SEM microstructure of the SS400/MS dissimilar steel weld interface of the fabricated joint. Microstructure examinations were performed at the weld zone (WZ) and thermo-mechanically affected zone (TMAZ) towards SS400 and MS side. Additionally, SEM-EBSD analysis was performed at the joint interface for deeper investigation of microstructure evolution as shown in Figs. 5-13a and b which are inverse pole figure (IPF) and image quality (IQ) maps, respectively. High angle grain boundaries (HAGBs), having misorientation angle $\theta > 15°$, are represented by blue lines, while low angle grain boundaries (LAGBs), $2° \leq \theta \leq 15°$, are represented by red lines. Additionally, Figs. 5-13(c-e) display the misorientation distribution for boundaries consisting of the HAGBs and the LAGBs in TMAZ of SS400, WZ, and TMAZ of MS, respectively. The macroscopic view of WZ and TMAZ of the SS400/MS joint interface is shown in Fig. 5-12a. Large plastic strains develop at the TMAZ of both sides as the streamlined structure in Fig. 5-12a. Moreover, as shown in Fig. 5-12b, the WZ dominantly consists of extremely fine equiaxed grains due to the occurrence of possible dynamic recrystallization of ferrite during welding process, but the slight fraction of fine martensite with smooth dark contrast is confirmed due to the martensitic transformation during cooling. The IPF map in Fig. 5-13a confirms the occurrence of dynamic recrystallization at the weld zone resulting in extremely fine grains with an average grain size of 0.9 μm. It is evident from the analysis that the proportion of HAGBs at WZ is significantly increased due to dynamic recrystallization. Further away from the weld zone there was a region towards SS400 and MS sides where the fraction of LAGBs were significantly higher than HAGBs. In this region, the average grain size was observed to be 4.8 μm and 2 μm towards MS and SS400 in Fig. 5-13b, respectively, which is higher than the grain

size in WZ. The areas of recovered structure as in Fig. 5-13b and partly transformed

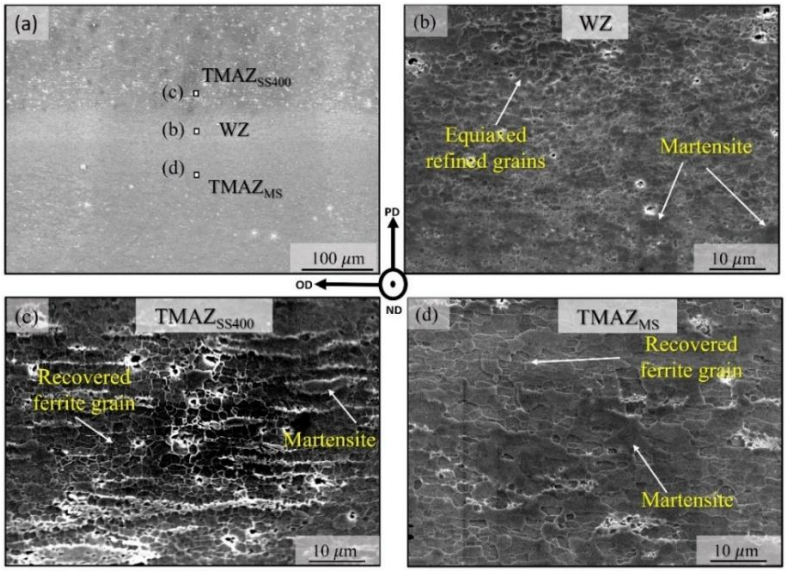

Fig. 5-12 Microstructure evolution at SS400/MS joint interface; (a) macroscopic morphology of interface (b) WZ region, (c) $TMAZ_{SS400}$, (d) $TMAZ_{MS}$ side.

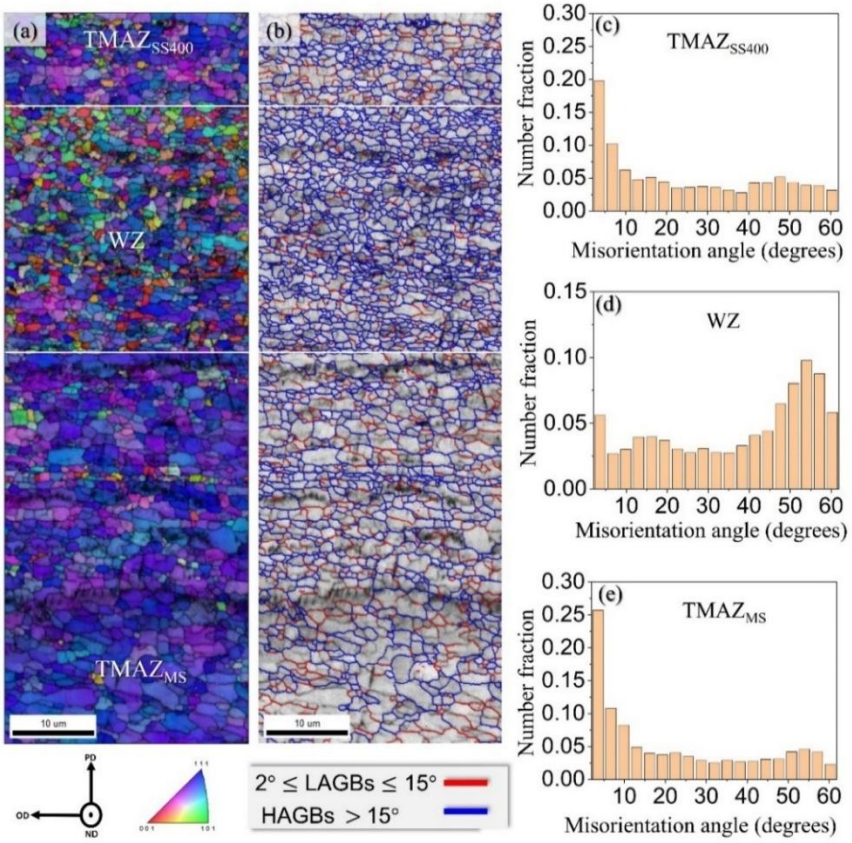

Fig. 5-13 (a) EBSD IPF map and (b) image quality map of SS400/MS joint interface; misorientation angle distribution of (c) $TMAZ_{SS400}$, (d) WZ, (e) $TMAZ_{MS}$.

structure as in Figs. 5-12c and d are collectively observed, commonly termed as the TMAZ region. The SEM micrographs of TMAZ regions towards SS400 and MS are shown in Figs. 5-12c and d, respectively. TMAZ is subjected to comparatively lesser heat as compared to the WZ. Therefore, incomplete recrystallization, but intensive recovery together with partial martensitic transformation proceeds in the TMAZ. Consequently, mostly recovered and partially martensitic transformed structures with smooth dark contrast were observed in the TMAZ region of SS400 and MS.

Microstructural evolution at MS/A7075 dissimilar metal joint interface

To study the microstructure evolution at the MS/A7075 weld interface, the grain morphologies at 0.1 mm and 2 mm from weld interface along with base metal were analyzed towards both MS and A7075 alloy. The locations of the EBSD examination are illustrated in Fig. 5-14a. Figs. 5-14b and c show the EBSD inverse pole figure maps as a function of distance from the joint interface on either side of the weld line. The base metals of MS and A7075 were mainly composed of coarse grains with an average grain size of 22.1 μm and 54.3 μm as shown in Figs. 14(b-iii) and (c-iii), respectively. Additionally, the microstructure towards A7075 in the heat affected zone (HAZ) and base material (BM) presents a negligible difference in terms of grain size. The average grain size in HAZ region of A7075 was observed to be ~55 μm. In HAZ, the heating and cooling cycles during LFW caused a negligible increase in the grain size. This observation is consistent with the prior studies during LFW of A7075-T6 [116]. Despite the negligible grain growth in the HAZ, microhardness distribution shows a notable reduction in the HAZ of A7075 as compared to BM hardness as shown in Fig. 5-10a. This reduction in hardness is likely due to partial dissolution and coarsening of the strengthening precipitates of A7075 in HAZ during welding. Fig. 5-14(b-ii) represents the EBSD maps at a distance

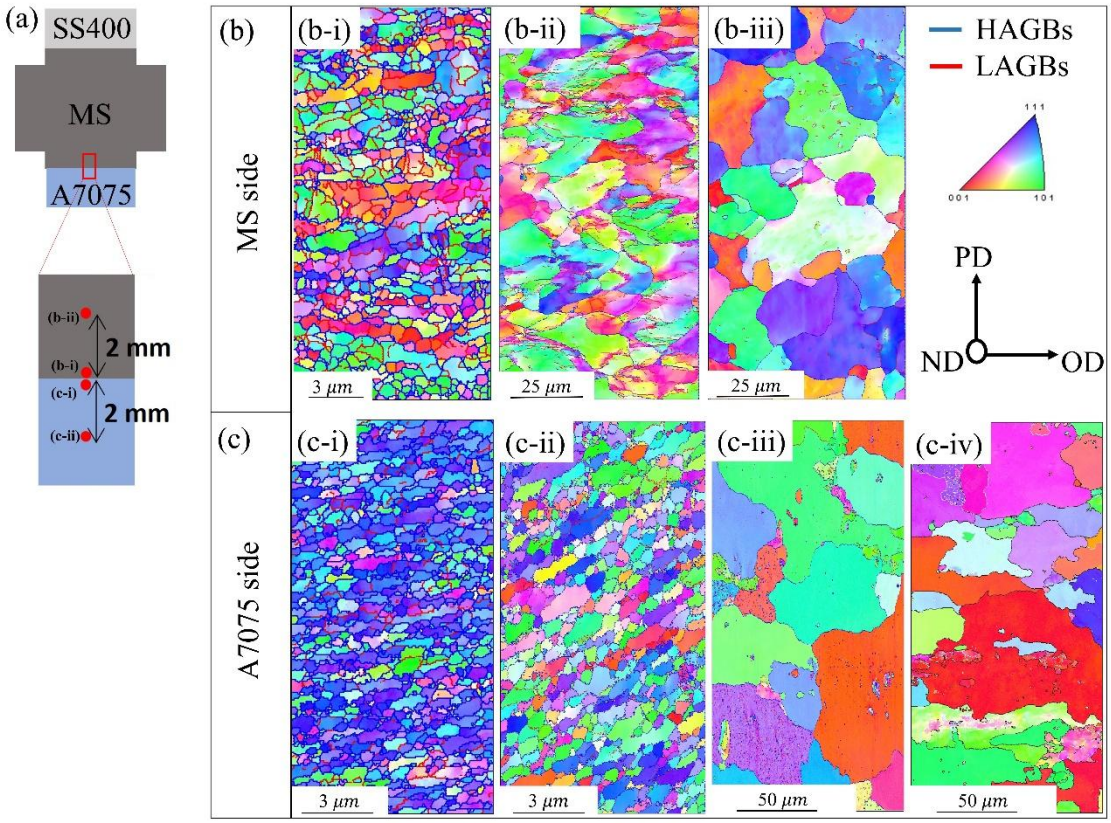

Fig. 5-14 Microstructure evolution at MS/A7075 joint interface; (a) location of EBSD examination at; (b-i) 0.1 mm away from interface towards MS, (b-ii) 2 mm away from joint interface towards MS, (b-iii) MS base metal, (c-i) 0.1 mm away from interface towards A7075, (c-ii) 2 mm away from joint interface towards A7075, (c-iii) A7075 HAZ, (c-iv) A7075 base metal.

of 2 mm from the weld interface towards MS, where the grains were still coarse but slightly elongated in the shear direction during welding. The average grain size was 14.8 μm, slightly smaller than that of the MS base metal. Moreover, at a distance of 2 mm towards A7075 in Fig. 5-14(c-ii), the grain sizes were significantly reduced with an average grain size of 1.7 μm. The grains were similarly observed to be elongated in shear direction as well. The microstructure at 0.1 mm distance from the weld interface was a large number of extremely fine grains on either side of weld interface line, as shown in Figs. 5-14(b-i) and (c-i). Refinement of the grains was related to the dynamic recrystallization in A7075 and dynamic recovery in MS caused by severe plastic

deformation during LFW. During the welding process, the initial grains at the contact surfaces were expelled as flash and new surfaces were formed with reduced size due to the friction cycles causing severe plastic deformation and heating. In comparison to the SS400/MS interface in Fig. 5-13a, where grain refinement took place due to dynamic recrystallization, at MS/A7075 interface, the grain refinement towards MS side was driven by dynamic recovery as shown in Fig. 5-14(b-i) due to low interface temperature of about 321℃. Additionally, there was noticeable difference in the grain size of MS in TMAZ region. Finer grains were observed in TMAZ region of MS towards the SS400/MS interface compared to TMAZ region of MS towards MS/A7075 interface.

On the other hand, the TEM investigation at MS/A7075 joint interface revealed the presence of an extremely thin and uniform IMC layer having a thickness of ~37 nm at the center and ~28 nm near the edge of the fabricated joint as shown in Figs. 5-15a and b, respectively, along with the corresponding TEM-EDS line scan analysis. The formation of an extremely thin IMC layer can be attributed to the joint fabrication processing. As the joint was fabricated using the LFW method, which comprises the expulsion of the interface material during each cycle of LFW. Therefore, after each LFW cycle, fresh surfaces of the materials were formed, which might have reduced the growth of the IMC layer. Moreover, the welding temperature at the MS/A7075 interface was reduced by an applied pressure of 300 MPa, leading to a lower interface temperature, which probably affected the growth of the IMC layer thickness. The detailed investigation on minimizing the IMC thickness at MS/A7075 interface and achieving a sound joint by applying a pressure of 300 MPa is provided in our previous study in Chapter 4. Therefore, the formation of extremely thin and uniform IMC layers at the center and edge locations corresponds to the uniform mechanical properties throughout the MS/A7075 joint

interface.

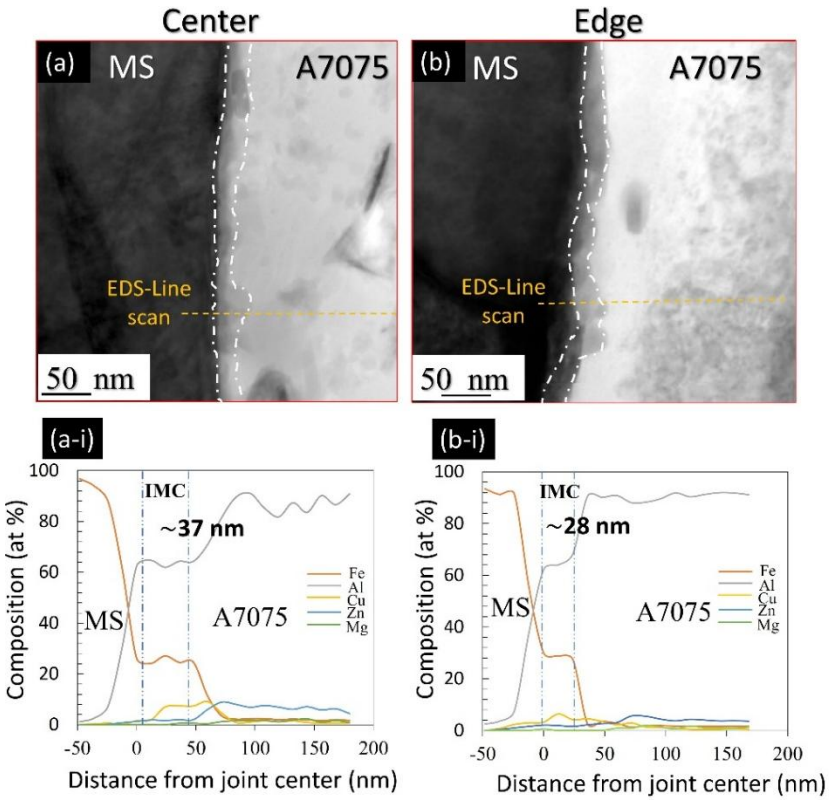

Fig. 5-15 TEM analysis of MS/A7075 joint interface at (a) center, (b) 1 mm deep from the edge of the weld, and corresponding TEM-EDS line scan at (a-i) center, (b-i) edge of the weld.

5.5. Conclusions

A sound dissimilar joint between SS400 and A7075 Al alloy was successfully obtained using Center-Driven Double-Sided linear friction welding method utilizing mild steel as a center material. The mechanical and microstructure investigations were performed at the center and edge locations of the obtained weld. The key conclusions of the study are as follows.

(1) Conventional direct linear friction welding between SS400/A7075 was difficult due to the absence of interfacial deformation towards SS400 during welding, which led to several un-jointed regions throughout the joint interface and eventually resulted in a poor joint strength of 77.6 MPa exhibiting an interfacial fracture.

(2) The CDDS-LFW promoted the simultaneous interfacial deformation of the mating materials at both MS/A7075 and MS/SS400 interfaces by exploiting the cross-point concept. Interface temperatures were controlled by changing the applied pressures towards SS400 and A7075 sides.

(3) The obtained joint exhibited a superior tensile strength of ~347.5 MPa compared to the past investigations of SS400 with any Al alloy joints, revealing 100 % joint efficiency concerning MS, and the fracture took place in the base metal region of mild steel, away from both the joint interface, i.e., SS400/MS and MS/A7075.

(4) SEM observation confirmed the absence of un-jointed regions and weld defects throughout the joint interfaces, ensuring a sound joining. Microstructure evolution through EBSD analysis revealed the extremely fine-grained microstructure near the joint interface region compared to coarse grain base metal regions.

(5) TEM investigation on MS/A7075 interface revealed the presence of extremely thin uniform IMC layer with a thickness of ~37 nm and ~28 nm at the center and edge of the weld. Obviously, no IMC was observed at the SS400/MS interface.

(6) The microstructure and mechanical properties, such as tensile strength and microhardness, were comparable and consistent at the center and edge of the weld, exhibiting the reliability and integrity of the fabricated weld.

Although, the joint efficiency in the present study reaches 100 % concerning MS base metal, the joint strength is inherently limited by the strength of center material, i.e., MS base metal itself. Therefore, the authors believe that a stronger joint may be obtained by systematically choosing a stronger center material and/or employing alternative strategies to fabricate high-quality dissimilar weld with enhanced joint strength.

Chapter 6: Novel sacrificing-sheet linear friction welding method for dissimilar joining of SS400 steel and A7075 alloy

Although in Chapter 5, a sound dissimilar joint was obtained between SS400 steel and A7075 Al alloy using mild steel as a center material by employing center-driven double-sided (CDDS)-LFW equipment. However, weld strength was inherently limited by the strength of center mild steel, where fracture took place in the base metal region of center mild steel. It indicated the ongoing challenges to further improve the joint strength of SS400/A7075 dissimilar joint. Also, it raises further concerns about the need to develop the process to enhance the joint strength and remove the dependence of weld strength on the strength of center material. Therefore, in this chapter, a novel joining method, called sacrificing-sheet linear friction welding (SSLFW) exploiting the CDDS-LFW equipment, was developed and utilized to further enhance the joint strength of SS400 steel and A7075 Al alloy. Much of the content in this chapter is adapted from the published article ‘‘Novel sacrificing-sheet linear friction welding method to fabricate sound dissimilar joint between steel and aluminum alloy’’ authored by Furkan Khan, Takuya Miura, Yoshiaki Morisada, Kohsaku Ushioda, Hidetoshi Fujii, in *Science and Technology of Welding and Joining, first published online 2025*.

6.1. Introduction

In the present Chapter, a novel joining method, called sacrificing-sheet linear friction welding (SSLFW), is proposed to obtain a sound dissimilar joint between SS400 steel (hereinafter referred to as SS400) and A7075-T6 Al alloy (hereinafter referred to as A7075). SSLFW involves placing a center sheet between the two side materials to be

joined. The center sheet is subjected to linear oscillating motion while side materials are pressed against it. The thermomechanical effect from each side leads to the expulsion of center sheet from joining interface, enabling direct joining between the side materials. Moreover, unlike CDDS-LFW, where the weld strength was limited by the strength of the center material, SSLFW employs a sacrificial center sheet made of the same material as one of the base metals, thereby eliminating this dependency. Consequently, SSLFW is expected to offer a promising solution to the limitations faced in CDDS-LFW and holds potential for further improving joint strength in dissimilar material welding.

As demonstrated in Chapter 5, despite the presence of a cross-point in the temperature dependence of material strength, achieving a sound joint between SS400 and A7075 remains challenging when using the conventional LFW method. Reportedly, the difficulty arise due to the cross-point exists at a very low temperature of ～120℃. The strength of SS400 at 120℃ is high enough to resist deformation, and the temperature dependence of it is very small in this temperature range, keeping the strength of SS400 almost equal to room temperature strength. While the strength of the A7075 alloy is mainly determined by its strengthening precipitates, and its dependence on temperature is more significant compared to SS400. As a result, the conventional LFW of SS400 and A7075 led to the preferential deformation of A7075 only, and no interfacial deformation occurred towards SS400 side. Therefore, burrs were not ejected from SS400, lacking the formation of a fresh joining interface towards SS400. Absence of interfacial plastic deformation in any of the two materials during friction welding can lead to the retention of impurities and oxides at the joining interface together with difficulty in proper material intermixing[120]. This, in turn, resulted in the formation of unjointed regions along the weld line, which can significantly compromise the overall joint integrity[71]. The similar issue

was documented by Akbarimousavi et al.[19] during dissimilar friction welding of cp-titanium and AISI316L stainless steel, highlighting the persistence of oxides at the weld center which resulted in a decreased joint strength. This occurred because the stainless steel does not deform and flash only consisted of titanium material due to the fact that base metal strength dependence on temperature of titanium is more significant than stainless steel.

Therefore, SSLFW is utilized to solve this difficulty and is expected to achieve simultaneous interfacial plastic deformation of dissimilar mating materials during welding. This is because SSLFW introduces a center sheet and establish a preheating stage that frictionally heats only stronger material side for a certain period of time to soften it prior to the pressurization towards softer material side. In this novel method of SSLFW, using SS400 sheet as a center material, frictional preheating of SS400 was performed without any external heating source in order to soften SS400 steel prior to the pressurization towards the A7075 alloy. So, SSLFW may be considered as a method utilizing pre-heating the stronger material prior to the start of welding process to achieve simultaneous deformation. Additionally, as the heat required for plastic deformation and oxide layer removal is generated intrinsically through interfacial friction between SS400 and center sheet of SS400. This eliminates the dependence on external thermal energy, thereby reducing process complexity and minimizing energy consumption.

6.2. Materials and experimental methods

6.2.1. Experimental setup and joining concept of SSLFW

SSLFW was employed to address the difficulties of joining dissimilar materials such as SS400 steel and A7075 Al alloy. Figs. 6-1a and 6-1b display the whole equipment and an internal view of the joining unit, respectively. Fig. 6-1c illustrates the SSLFW setup,

placement of specimens, and shape of the used specimens. Unlike to the conventional LFW method, SSLFW comprises placing a center sheet between the two side materials to be joined. The center sheet is subjected to the linear oscillating motion while the side materials are pressed against it, leading to the expulsion of the center sheet, enabling direct joining between the side materials. The detailed joining process of SSLFW is explained in the following paragraph and illustrated in Fig. 6-2.

SSLFW comprises five typical stages to achieve a joint. First, the materials to be joined are brought into contact with the center sheet (stage 1) as shown in Fig. 6-2a. The center sheet is subjected to the oscillation motion at preset oscillation frequency and preheating of steel specimen is performed for a certain preheat duration by applying a preheating pressure *P1*, causing steel specimen to soften before the pressurization towards Al alloy (stage 2), Fig. 6-2b. It is noteworthy that no pressurization is applied towards Al alloy side during preheating phase, keeping the strength of Al alloy high enough. After the preheating time is reached, pressure *P2* is applied towards Al alloy side. The increased thermo-mechanical effect from each side leads to the expulsion of the center sheet around the joining area, enabling the direct contact of side materials (stage 3). The center sheet is preferentially expelled around the central region first, during sacrificing phase-I, Fig 6-2c, due to intensive frictional heating from each side and severe plastic deformation, followed by pull-out of any remaining sheet around the edge, during sacrificing phase-II as shown in Fig. 6-2d (stage 4). It is worth noting that as soon as the center sheet is expelled and direct contact is achieved, the pressure becomes equal each side as *P2*. Once the desired upset is reached, the oscillation is discontinued to complete the joining during forge phase (stage 5) followed by cooling. The material expulsion effectively removes surface oxides and impurities at the interface due to self-cleaning nature of LFW[82],

revealing fresh metal surfaces and enabling the formation of a sound joint.

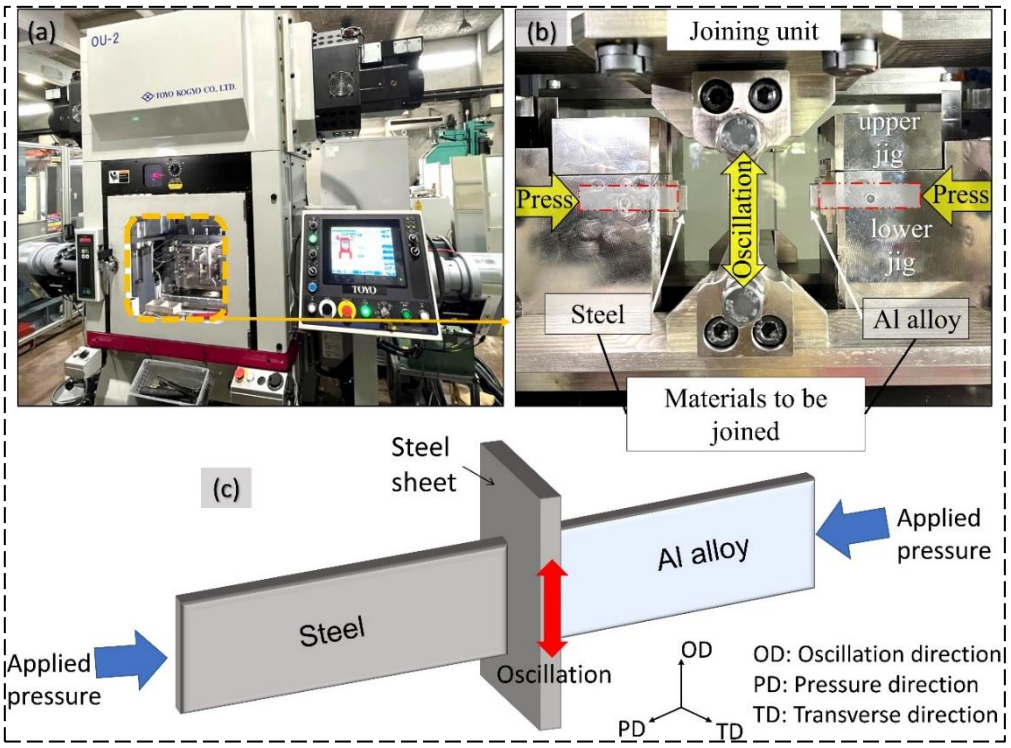

Fig. 6-1 Experimental setup of SSLFW, (a) entire setup, (b) internal view of joining unit, (c) shape and placement of the used specimens.

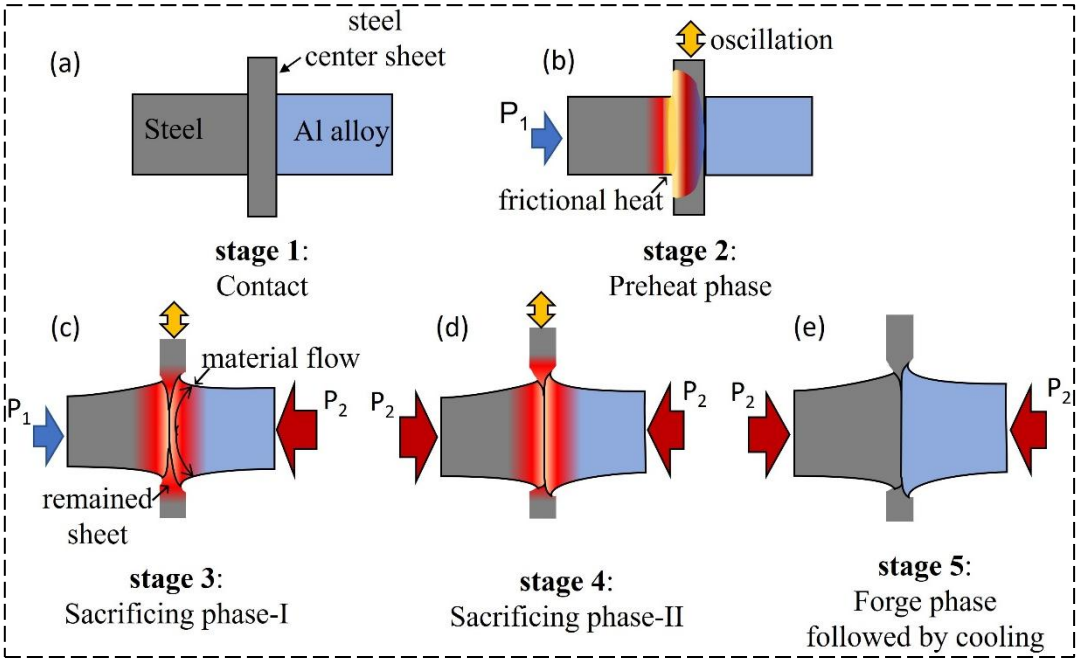

Fig. 6-2 Conceptual schematics of SSLFW method depicting five typical stages as (a) stage 1:

contact phase, (b) stage 2: preheat phase, (c) stage 3: sacrificing phase-I, (d) stage 4: sacrificing phase-II (e) stage 5: forge phase followed by cooling.

6.2.2. Materials and processing parameters

SS400 and A7075 specimens, each measuring 80 mm^{PD} x 20 mm^{OD} x 5 mm^{TD}, were selected as the primary materials to be joined, where PD, OD and TD stand for the pressure, oscillation and transverse directions (Fig. 6-1c). A 2 mm-thick rectangular sheet (25 mm x 40 mm) made of SS400 was used as a center sheet with the independent applied pressures towards SS400 and A7075 sides. Chemical compositions (wt.%) and UTS of these base metals are shown in Table 3-1 in Chapter 3.

Center-driven double-sided (CDDS)-LFW equipment (8AT2020A00, TOYO KOGYO) was utilized to fabricate the dissimilar joints by SSLFW. Preheating of SS400 side was performed by applying a pressure of 75 MPa (*P1*) for different preheating times of 0s (no preheating), 0.5s, 1s, and 1.5s. Once the preheating time reached the set value, an objective pressure of 300 MPa (*P2*) was applied towards A7075 at a forging speed 20 mm/s (forging speed refers to the pressing speed of materials along the length during SSLFW). The applied pressures were selected based on the temperature dependence behavior of material strength. Fig. 6-3 shows the temperature dependence behavior of UTS of A7075 and SS400. Temperature dependence graphs suggest that both A7075 and SS400 are expected to plastically deform when the temperature exceeded 225℃ and 525℃, respectively, under an applied pressure of 300 MPa (*P2*) as indicated by red arrows in Fig. 6-3a. Temperature above 225℃ is assumed to be obtained by preheating and friction heating towards A7075, while the temperature above 525℃ can be obtained due to thermal conduction from the SS400/SS400 interface having nearly ～714℃ at a preheating pressure of 75 MPa (*P1*). Fig. 6-3b shows the schematic illustration of conventional LFW between SS400 and A7075 under an applied pressure of 470 MPa

corresponding to the cross-point strength. The results showed preferential deformation of A7075 while SS400 remained undeformed during welding, as confirmed in Chapter 5. While Fig. 6-3c illustrated SSLFW process showing a preheating phase to soften SS400 prior to the pressurization towards Al side. Furthermore, keeping the preheating time constant at 1.5s, the forging speed towards A7075 was further varied to 30 mm/s, 40 mm/s, and 50 mm/s. The reason for increasing the forging speed towards A7075 will be discussed later. The burn-off length towards each side was kept constant at 3 mm with constant amplitude and oscillation frequency of 2 mm and 50 Hz, respectively. Furthermore, all the metallographic sample preparation and mechanical testing were performed as described in Chapter 3. Additionally, post-welding; artificial aging heat treatment was carried out for 10h at 120℃ for the joint fabricated at 50 mm/s forging speed.

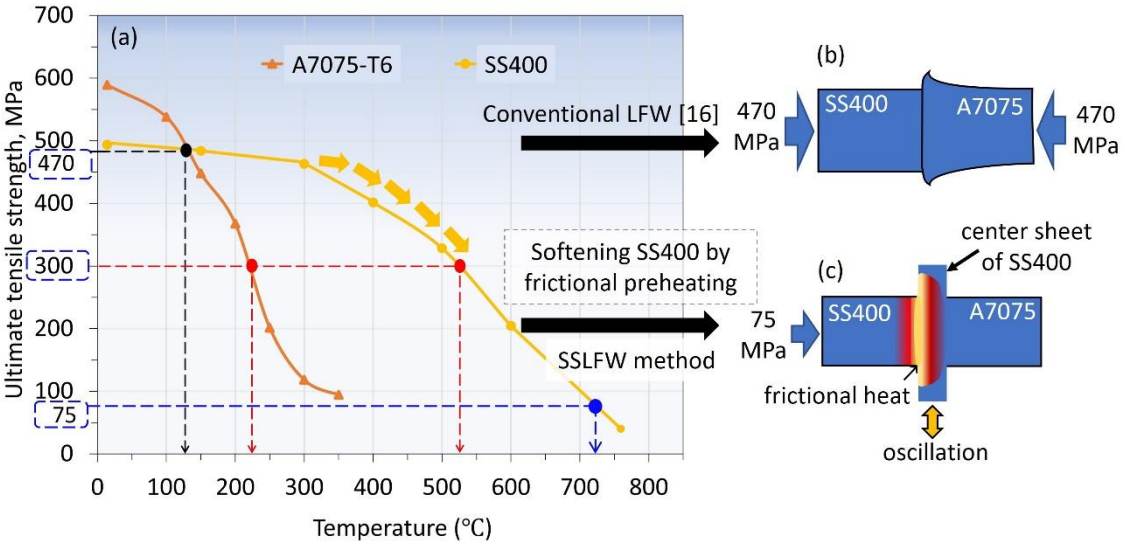

Fig. 6-3 (a) Temperature dependence of UTS of A7075 and SS400, (b) schematic illustration of conventional LFW between SS400/A7075, (c) schematic illustration of SSLFW showing preheating of SS400 to soften it prior to the pressurization towards A7075.

6.3. Results and discussion

6.3.1. Effect of pre-heating time

Figs. 6-4(a-d) show the joint appearance of the fabricated welds at various pre-heating times ranging from 0s (without preheating) to 1.5s, respectively. The objective of preheating was to soften the SS400 specimen prior to the pressurization towards A7075 during welding. The applied forging speed towards SS400 was 0.5 mm/s during the preheating phase and altered to 20 mm/s after completion of the preheat duration. It is worth to be noted that no pressurization was applied towards A7075 during preheating. Therefore, the strength of A7075 was kept high enough. The fabricated weld coupon consisted of A7075 and SS400, primary materials to be joined, and a center sheet as indicated by thin yellow arrows in Figs. 6-4(a-d). The flash formation towards SS400 is indicated by blue arrows, and that of the A7075 side is shown by broken arrows in Figs. 6-4(a-d). The flash formation towards A7075 is not finely visible as it remains another side of the center sheet.

Figs. 6-4(e-h) show the joint interface macrographs of the fabricated welds. The presence of any un-jointed regions was identified throughout the joint interface. As can be seen in Fig. 6-4e, the joint fabricated without preheating revealed the presence of several un-jointed regions throughout the weld line as indicated by red arrows. Moreover, the center sheet experienced rupture during welding and remained within the butt surfaces of side materials, as indicated by black arrows. Similarly, for a preheating duration of 0.5s and 1s, there were several un-jointed regions at the interface and also, the center sheet remained discontinuously within the butt surfaces, as indicated by black arrows in Figs. 6-4f and 6-4g, causing uneven joining interface throughout the weld line. These un-jointed regions, as shown by red arrows, are presumably caused by unevenness of the joint interfaces due to insufficient preheating. Therefore, it is thought that the remained

un-jointed regions due to the uneven joint interface would have greatly influenced the weld strength[122]. In contrast, a preheating time of 1.5s resulted in complete suppression of these un-jointed regions and formation of a quite flat weld interface without unevenness as shown in Fig. 6-4h. Suppression of un-jointed regions and formation of a flat weld interface, after 1.5s preheating, can be attributed to the thorough expulsion of center sheet around the joining area. This enabled direct joining between SS400 and A7075 alloy.

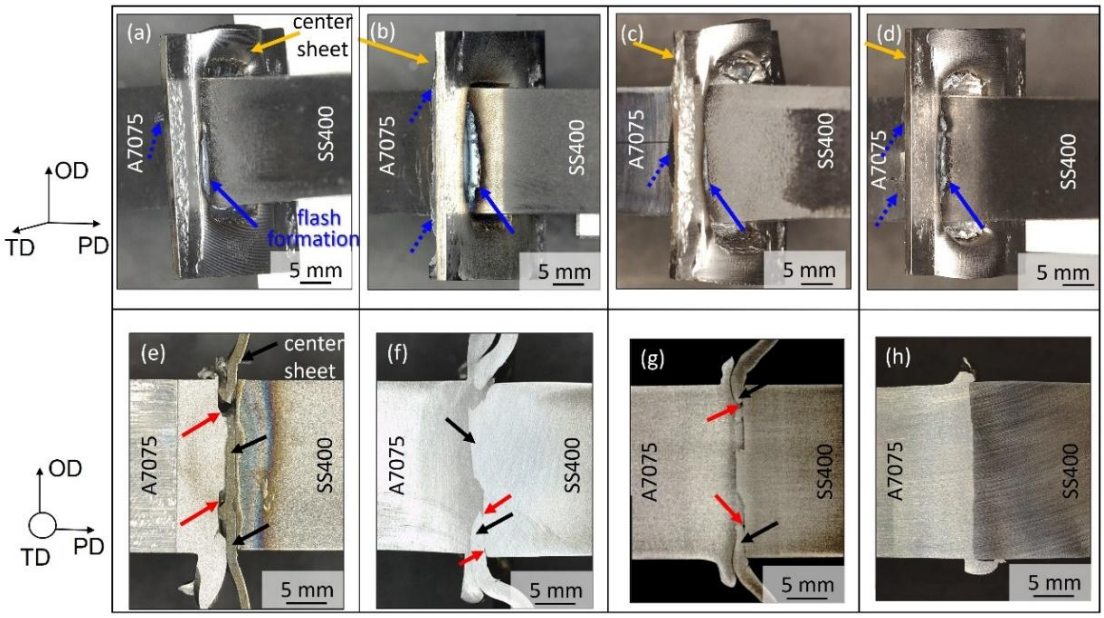

OD: Oscillation direction, PD: Pressure direction, TD: Transverse direction

Fig. 6-4 Joint appearance of fabricated welds with a frictional preheating period of; (a) without preheating, (b) 0.5s, (c) 1s, (d) 1.5s; and (e-h) corresponding joint interface macrostructure analysis of fabricated welds.

6.3.2. Effect of forging speed and its relation to welding pressure

Figs. 6-5(a-c) show the macrographs of the fabricated joints at variable forging speeds of 30 mm/s, 40 mm/s, and 50 mm/s towards A7075 side, respectively. The preheating time towards SS400 was kept constant at 1.5s. Figs. 6-5(d-f) show the interface macrostructure of the corresponding joints. The center sheet was expelled from the butt

surfaces during welding, as indicated by the white arrows in Figs. 6-5(d-f), enabling direct joining of SS400 and A7075. The interface macrostructure analysis of all the fabricated joints revealed a quite flat interface without any un-jointed regions and without uneven joint interface throughout, ensuring a sound dissimilar joining between SS400 and A7075.

Figs. 6-6 (a-c) show the relationship between forging speed and welding pressure during SSLFW at varying forging speeds of 30 mm/s, 40 mm/s and 50 mm/s towards A7075. The burn-off length towards SS400 and A7075 is presented in Fig. 6-6d. The burn-off length is the total linear measurement of the materials consumed or plasticized out as flash during the LFW process. The burn-off length for SS400 is shown only of the joint fabricated at a forging speed of 50 mm/s. The data show that as soon as the preheating time of 1.5s was reached, A7075 was pressed against the center sheet with a preset forging speed. It should be noted that the welding pressure increased as the forging speed increased towards A7075. It was observed that just after the completion of the preheating period and start of loading towards A7075 side, the welding pressures towards SS400 and A7075 showed equal value. The peak welding pressures were observed to be 227.2 MPa, 371 MPa and 451 MPa at forging speeds of 30 mm/s, 40 mm/s, and 50 mm/s, respectively. Therefore, the obtained results suggest that the higher forging speeds resulted in increased welding pressures, which can lead to decreased interface temperatures.

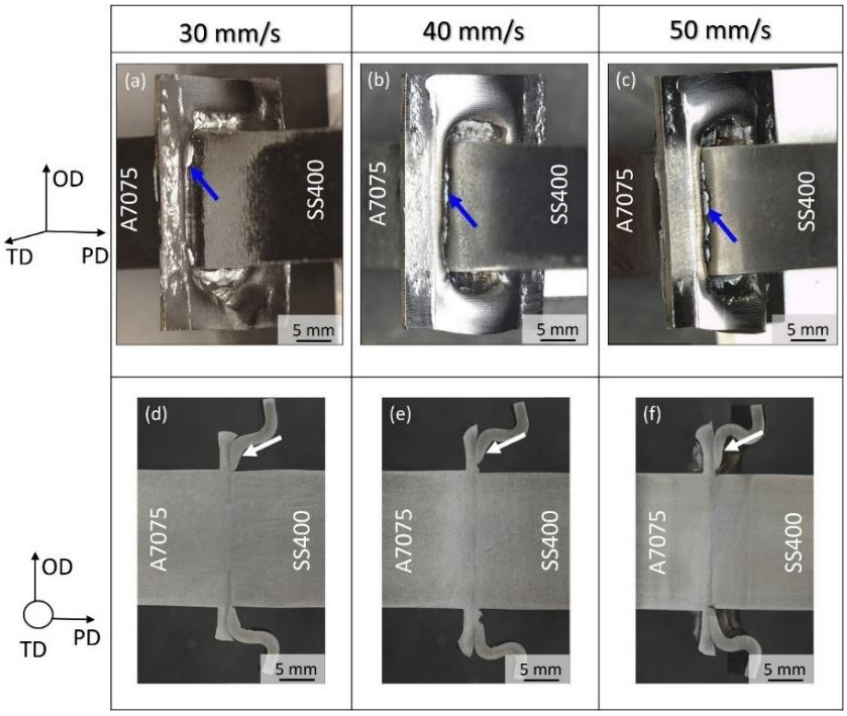

Fig. 6-5 Joint appearance of fabricated welds by keeping preheating time constant at 1.5s and varying forging speed towards A7075 (a) 30mm/s, (b) 40mm/s, (c) 50mm/s; and (d-f) corresponding joint cross-section macrostructure analysis of fabricated joints.

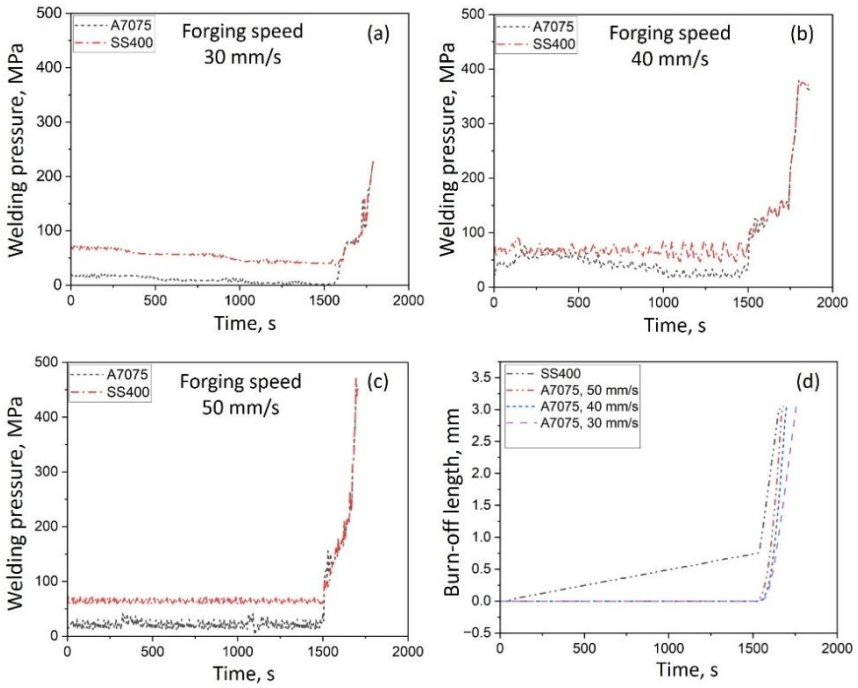

Fig. 6-6 Welding pressure vs time curve during SSLFW under variable forging speeds of (a) 30mm/s, (b) 40mm/s, (c) 50mm/s towards A7075 side, (d) depicting the burn-off length during SSLFW.

6.3.3. Mechanical performance of the fabricated welds

6.3.3.1. Joint tensile strength and fractured tensile specimen

Further, the mechanical and microstructure characterizations were performed for the joints fabricated at a preheating period of 1.5s under the forging speeds of 20 mm/s, 30 mm/s, 40 mm/s, and 50 mm/s towards A7075. Tensile tests were conducted to evaluate the joint strength of the fabricated welds. The tensile test specimens were prepared so that the welding interface was in the center of the specimen, as illustrated in Fig. 6-7e. Lower joint strengths with average value of ~290 MPa and ~352 MPa were obtained at comparatively lower forging speeds of 20 mm/s and 30 mm/s (hereinafter referred to as 20 mm/s-joint and 30 mm/s-joint, respectively) as shown in Fig. 6-7a. The joint strength was observed to be increased with increasing forging speed from 20 to 40 mm/s. However, the welds produced using forging speeds of 40 mm/s and 50 mm/s (hereinafter referred to as 40 mm/s-joint and 50 mm/s-joint, respectively) exhibited comparable joint strengths. The average joint strength reached a peak value of 425 MPa for 40 mm/s-joint and 50 mm/s-joint revealing a joint efficiency of ~88% with respect to the base metal (BM) strength of SS400. Here, the joint efficiency is defined as the ratio of the weld strength to the tensile strength of the unaffected softer SS400. For a more comprehensive assessment of the joint performance, joint efficiency is also calculated relative to the tensile strength of the unaffected harder A7075 base material, which was 72%. This dual-reference approach offers a clearer comparison of the weld strength relative to both material perspectives. Fig. 6-7b depicts the fractured tensile specimen of the corresponding joint, revealing its fracture location. The fracture location and joint interfaces are denoted by red and yellow arrows, respectively. Although the welds were obtained without any un-jointed regions irrespective of the forging speeds, as shown in Figs. 6-4h and 6-5(d-f); however, a clear difference in their fracture behavior is evident. 20 mm/s-joint revealed a

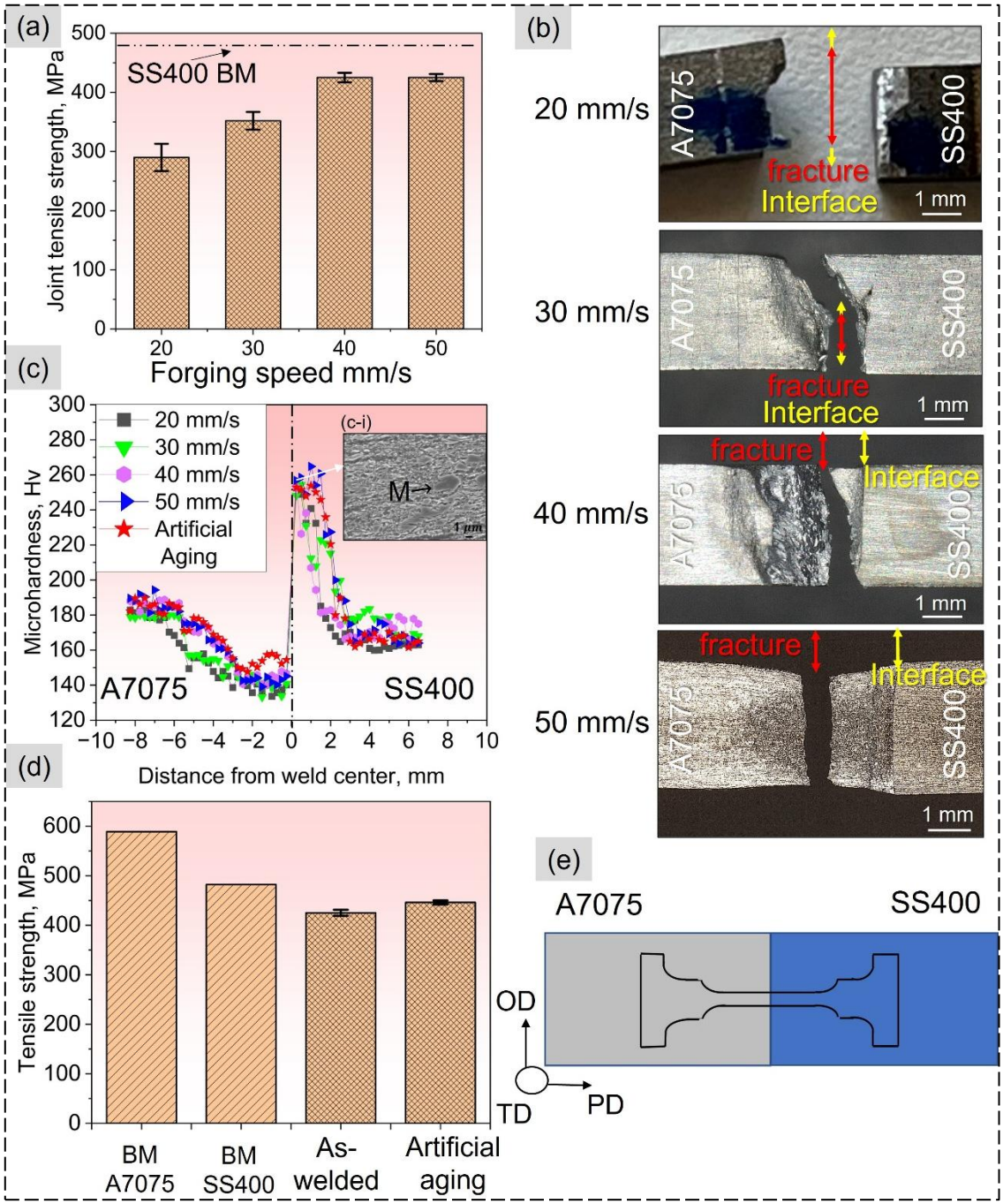

Fig. 6-7 Mechanical performance of the fabricated welds (a) joint tensile strength (b) fractured tensile specimen of the welds (c) microhardness distribution, (c-i) SEM image at 50 mm/s-joint interface towards SS400 side (d) tensile strength comparison of 50mm/s-joint as-welded and aging treated specimen along with base metals (e) schematic and location of tensile test specimen.

brittle fracture which presumably took place through the IMC layer in the interface. Whereas 30 mm/s-joint showed a mixed mode fracture behavior of ductile mode on the

A7075 side and brittle mode at the interface. Evidently, the fracture behavior was improved with increasing forging speed. As a result, 40 and 50 mm/s-joints showed a fracture with necking, and the fracture took place far from the joint interface towards A7075 side, apparently through the softened region of A7075. It is interesting that despite the thorough expulsion of center sheet around butt surfaces and obtaining a smooth and uniform interface without un-jointed regions during SSLFW, a lower joint strength with brittle fracture mode was obtained in case of 20 mm/s-joint and 30 mm/s-joint compared to the 40 mm/s-joint and beyond. To clarify this happening, the joint interface microstructure was thoroughly investigated as explained later in section 6.3.4.

6.3.3.2. Microhardness distribution and effect of artificial aging

Fig. 6-7c shows the hardness distribution on the joint cross-sections of 20, 30, 40, and 50 mm/s-joints along with the artificially aged (AA) 50 mm/s-joint. The base materials, SS400 and A7075, exhibited average hardness values of 165 Hv and 182 Hv, respectively. Hardness distribution was observed to be significantly different on either side of the weld center line. All the produced welds revealed a sharp increase in hardness as moving from SS400 BM to the joint interface, exhibiting peak hardness ranging from 260 Hv to 275 Hv. This significant hardening adjacent to the joint interface towards SS400 can be attributed to the grain refinement strengthening due to possible dynamic recrystallization together with the presence of partial martensitic (M) structure formed near the joint interface, as confirmed in SEM micrograph shown in Fig. 6-7(c-i). The martensite formation was thought to occur due to the elevated temperature at SS400/SS400 interface during the pre-heating phase, followed by cooling of the fabricated weld. On the other hand, A7075 alloy or Al-Zn-Mg alloy, are strengthened by metastable precursors and the stable η phases precipitates. The literature reveals that the

size and distribution of these precipitates mainly affect the strength of A7075 alloy joints[113]. Since the mechanical strength of precipitation-hardened Al alloys heavily depends on the size, distribution, and density of these precipitates. Therefore, dissolution of these hardening particles during welding results in a significant loss of strength and hardness in the weld metal and the heat-affected zone (HAZ). Temperatures higher than 200°C start softening in these alloys, and full dissolution of the precipitates may take place above 400°C[108], leading to significant reduction of the strength of A7075 alloy as also shown in temperature dependence of strength curve in Fig. 6-3a. Therefore, in the hardness distribution curve towards A7075, all joints exhibited a noticeable decrease in hardness when moving from the A7075 BM toward the joint interface, despite the grain refinement caused by dynamic recrystallization as discussed later. This reduction indicates the formation of a softening zone near the joint interface. It is primarily due to the dissolution or coarsening of hardening particles under the thermal and mechanical effects of the LFW process. However, the average hardness values in the softened region of A7075 were improved with the increase of forging speed. It revealed an average hardness of 137.8 Hv, 139.9 Hv of 20 mm/s and 30 mm/s-joints, respectively, and 144.1 Hv and 145.2 Hv of 40 mm/s and 50 mm/s-joints, respectively. Despite the hardness improvement with the increase of forging speed, the lowest hardness was always observed in the softened region of A7075 across all the joint interfaces, marking the minimum hardness point.

Therefore, post-weld artificial aging (AA) was performed on the 50 mm/s-joint to suppress the softened region towards A7075. The observed results were compared with the as-welded specimen to assess the effect of AA on the mechanical performance of the obtained weld. Figs. 6-7c and 6-7d compares the microhardness and joint tensile strength

between AA and as-welded 50 mm/s-joint, respectively. BM strengths of A7075 and SS400 are also shown for an intuitive view in Fig. 6-7d. AA at 170℃ for 10 h promotes an increase in hardness in the TMAZ of A7075 with an average improvement of 11 Hv compared to the as-welded specimen. However, the recovery of hardness in HAZ was comparatively lower than TMAZ region near the joint interface, leading to the minimum hardness point likely due to the coarsening of the strengthening precipitates in HAZ[113]. The recovery in hardness induced by artificial aging is reflected in the tensile performance of the weld. Artificially aged specimen revealed an average joint strength of ~448 MPa leading to improve the joint efficiency from 88% in as-welded state to 93% after aging with respect to the strength of un-affected softer SS400 BM.

6.3.4. Joint interface microstructure analysis

The dissimilar joint interfaces were investigated by conducting SEM and EDS analysis to observe the presence of possible IMCs at A7075/SS400 interface. Furthermore, the reason for increasing the forging speed is discussed in this section. Figs. 6-8(a-c) show the SEM micrographs and corresponding SEM-EDS line analysis of the interfaces of fabricated joints. The IMCs at the joint interface are bordered with the two-dot chain lines at all the joint interfaces as shown in Figs. 6-8(a-i) to (c-i). A considerably thick IMC layer was observed at the joint interface of 20 mm/s-joint which adversely affected the joint strength and fracture mode of the fabricated weld. The SEM-EDS analysis confirms that as the forging speed increased, the IMC layer thickness reduced from ~1.8 μm to ~0.8 μm for 20 and 30 mm/s-joints, respectively, as shown in Figs. 6-8(a-i) and (b-i). On the other hand, at the interface of 40 mm/s-joint and beyond, no IMC was observed at the SEM level, as shown in Fig. 6-8(c-i). Therefore, the 40 and 50 mm/s-joint interfaces were characterized using TEM investigation. The TEM micrographs coupled with TEM-EDS

line scan analysis are presented in Figs. 6-9a and b, respectively. Although, no IMC was observed using SEM; however, TEM investigation revealed the presence of extremely thin IMC at the interfaces of 40 and 50 mm/s-joints. The IMC was identified having a thickness of ~75 nm (0.075 μm) and ~51 nm (0.051 μm) at the interfaces of 40 and 50 mm/s-joints, respectively, as indicated by the broken lines in Figs. 6-9(a-i) and (b-i). The increase in joint strength and improved fracture behavior with increasing forging speed is thought due to the suppression of the formation of thick brittle IMC layer. This is because the higher forging speed resulted in increased welding pressure, which might have led to fabricating a joint at a lower welding temperature during LFW. The selected area electron diffraction (SAED) image of 50 mm/s-joint is shown in Fig. 6-9c. The diffraction pattern revealed the formation of $Al_5Fe_{2\,(002)}$ and $Al_5Fe_{2\,(222)}$ IMC at the dissimilar joint interface.

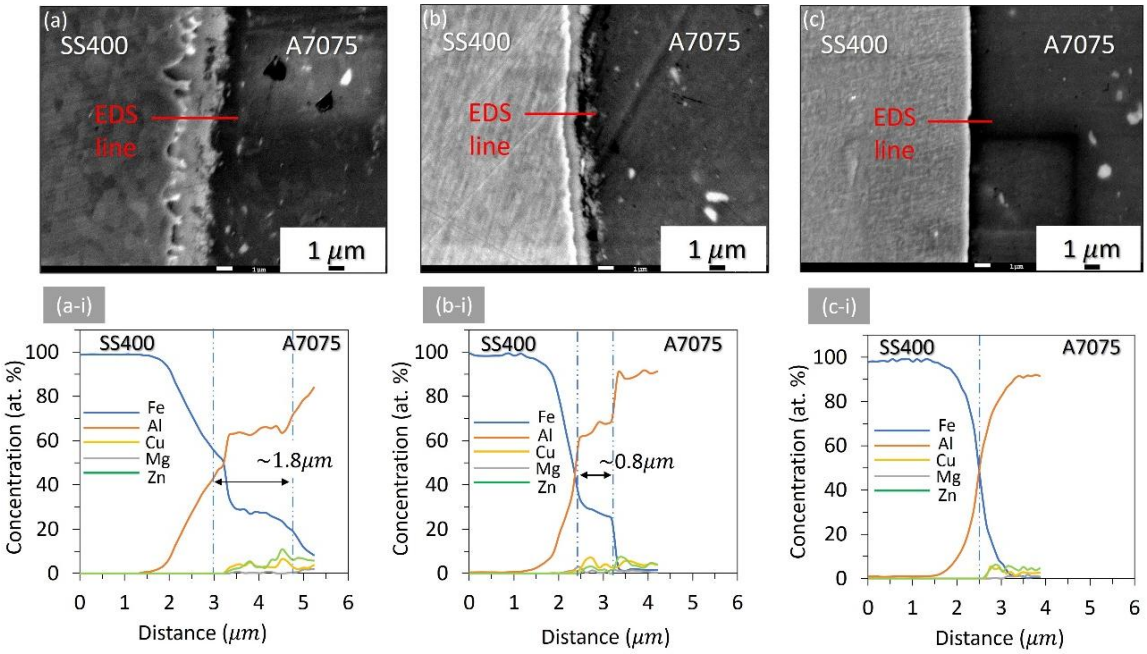

Fig. 6-8 SEM micrographs of joint interfaces (a) 20 mm/s-joint, (b) 30 mm/s-joint, (c) 40 mm/s-joint; and corresponding SEM-EDS line analysis of joints as (a-i), (b-i), and (c-i), respectively.

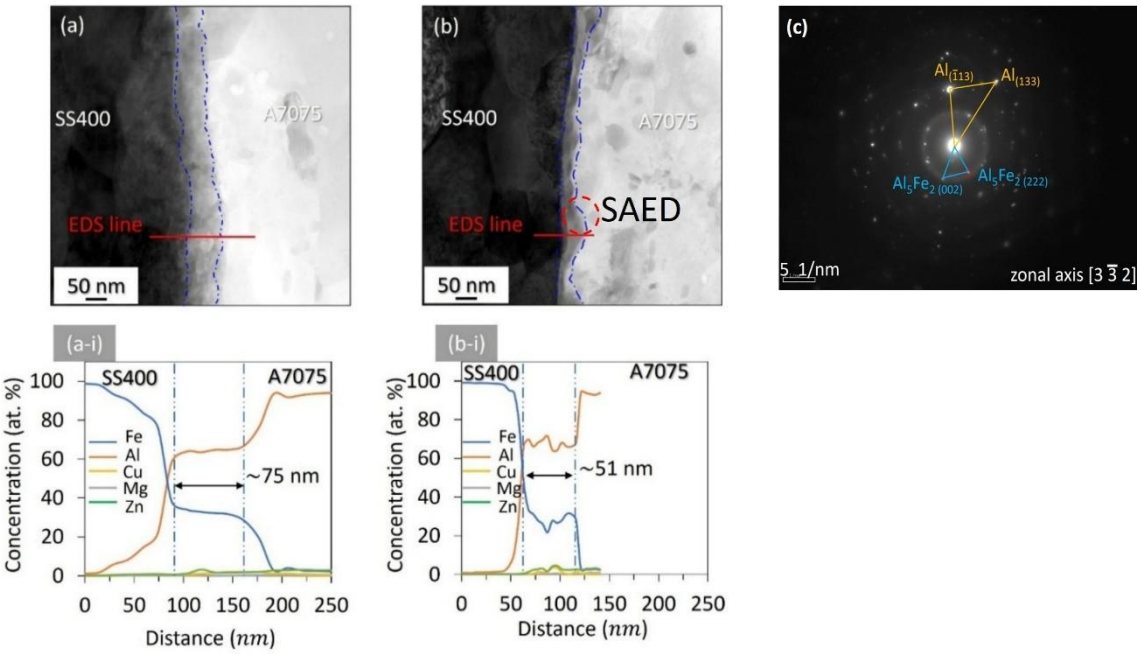

Fig. 6-9 TEM analysis of joint interfaces (a) 40 mm/s-joint and (b) 50 mm/s-joint showing SAED of IMC in the inset; and corresponding TEM-EDS analysis as (a-i), and (b-i), respectively.

The electron backscatter diffraction (EBSD) analysis is utilized to observe the microstructural characteristics of SS400 and A7075 base metal (BM) and 50 mm/s-joint interface. Figs. 6-10(a) and (b) depict the EBSD-inverse pole figure (IPF) maps of SS400 and A7075 BM, respectively. The EBSD-IPF maps, at 0.1 mm from the 50 mm/s-joint interface, towards SS400 and A7075 side are shown in Figs. 6-10(c) and (d), respectively, which reveals the crystallographic orientation of the grains. High angle grain boundaries (HAGBs), having misorientation angle $\theta > 15°$, are represented by black lines, while low angle grain boundaries (LAGBs), $5° \leq \theta \leq 15°$, are represented by white lines. Additionally, grain size distribution of BM in initial conditions are presented in Figs. 6-10(e) and (g) for SS400 and A7075, respectively, and that of after LFW is shown in Figs. 6-10(f) and (h) towards SS400 and A7075, respectively. The BM of SS400 and A7075 alloy were observed to be composed of coarse grains with average size of $\sim 25.8\ \mu m$ and $\sim 56\ \mu m$, respectively. Notably, after LFW grains were significantly refined either side of the joint

interface compared to initial microstructural conditions of base alloys as confirmed by EBSD-IPF maps in Figs. 6-10(c) and 6-10(d) towards SS400 and A7075, respectively. The refinement of grains was related to occurrence of dynamic recrystallization due to severe plastic deformation and localized frictional heating during LFW process. After LFW, the average grain size near interface was observed to be approximately ~1.1 μm and ~3.6 μm towards A7075 and SS400, respectively. Therefore, evidently, the initial coarser grains are being consumed and new equiaxed grains are formed with substantially reduced size as moving from BM to the joint interface which is one of the main features easily recognizable under dynamic recrystallization conditions. Dynamic recrystallization is an important phenomenon in solid-state welding processes like LFW. During LFW, the combination of severe plastic deformation and intense localized heating at the interface leads to the nucleation and growth of new, fine grains, replacing the original coarse grains. This process plays a key role in enhancing the material properties of the welded joint, particularly near the interface. Dynamic recrystallization significantly influences the microstructure of both SS400 and A7075 alloys. The refined grains along with presence of martensite at the joint interface contribute to the higher hardness observed near the joint interface, especially towards SS400 side as can be seen in Fig. 6-7c. On the contrary, the microhardness of A7075 exhibited a reduction in hardness near the joint interface despite the formation of an ultrafine grain structure by dynamic recrystallization. This reduction in hardness near the joint interface, towards A7075, can be attributed to the dissolution of hardening particles of A7075 due to elevated temperature during LFW[108], leading to the minimum hardness region across the weld.

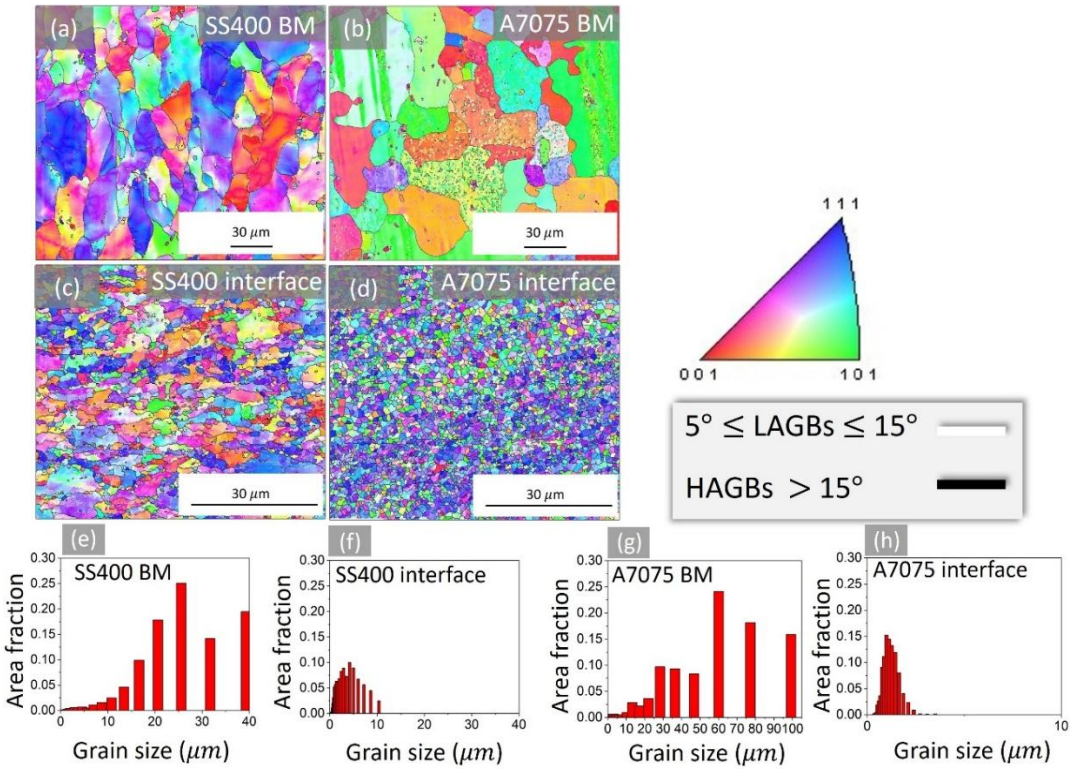

Fig. 6-10 EBSD-IPF maps of base metal (a) SS400, (b) A7075 and 50 mm/s-joint at 0.1 mm from interface towards (c) SS400, (d) A7075, along with (e-h) bar graphs illustrating grain size distribution of base metals in initial condition and after LFW.

Fig. 6-11 presents a comparison of recent studies on friction-based joining of precipitation-hardened Al alloys (A6061 and A7075) with various types of steel, including carbon steels and stainless steels. While the CDDS-LFW method achieved higher joint strength than previous approaches, the weld strength remained inherently limited by the center material, where fracture occurred during tensile testing. Additionally, conventional LFW and other friction welding techniques often suffer from insufficient interface deformation[71] and excessive IMC formation[35]. As shown in Fig. 6-11, the SSLFW method developed in this study overcame these limitations, achieving a high joint strength of ~425 MPa, which was further enhanced to ~448 MPa through post-weld artificial aging. To the best of the authors' knowledge, this is the highest reported joint strength for dissimilar joining of A7075 with any iron-based alloy to date.

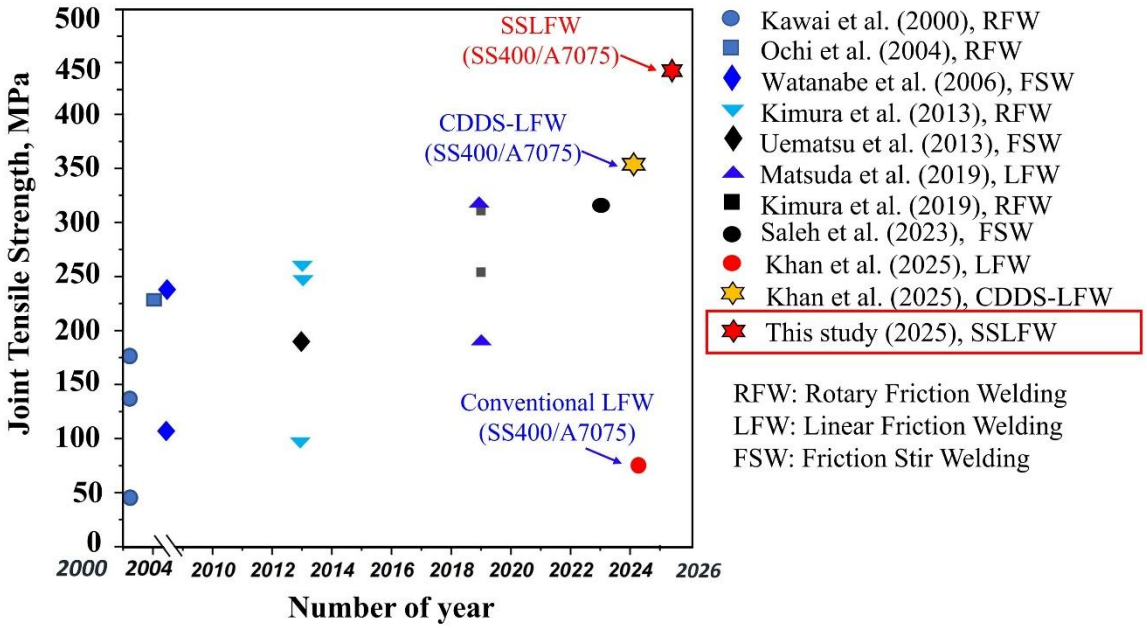

Fig. 6-11 Comparison of joint tensile strengths achieved by friction-based welding of precipitation hardened Al alloy (A6061 and A7075) with various steels.

6.4. Conclusions

Novel sacrificing-sheet linear friction welding (SSLFW) method by oscillating a center sheet of SS400 steel was exploited to fabricate dissimilar joints between SS400 steel and A7075 aluminum alloy. The results obtained are summarized as follows:

1. By establishing a preheating stage that frictionally heats only SS400 side for a certain period of time, the center sheet was effectively expelled from the joint interface, and SSLFW that directly joins the SS400 and A7075 has been achieved.
2. The joint obtained without preheating resulted in several un-jointed region throughout the weld interface and the center sheet remained within the butt surface of the side materials.
3. In the cases with preheating time of 0.5s and 1.0s uneven joint interfaces were revealed and several un-jointed regions were identified at the joint interface. Whereas, the joint fabricated with a preheating time 1.5s resulted in sound joining without any

un-jointed regions with a quite flat interface.

4. A thick IMC layer of 1.8 μm and 0.8 μm were formed at the interface of the joints with forging speed of 20 mm/s and 30 mm/s, respectively. Whereas, the higher forging speed of 40 mm/s and 50 mm/s resulted in extremely thin IMC thickness of 51 nm (0.051 μm) and 75 nm (0.075 μm) at the joint interface, respectively.
5. The joints with the forging speed of 40 mm/s and 50 mm/s showed excellent joint strength of 425 MPa revealing a joint efficiency of 88% with respect to the strength of un-affected softer SS400 steel base material. Additionally, aging treatment at 120℃ for 10h promotes the hardness recovery in the softening zone of A7075 leading to further improving the joint efficiency to 93%.

Chapter 7: Elucidating process parameters and bonding mechanism of S45C/A6061 dissimilar joint exploiting novel SSLFW

Following the development and utilization of the novel sacrificing-sheet linear friction welding (SSLFW) method for joining dissimilar steel and Al alloys in Chapter 6, this chapter aims to further explore the applicability and robustness of the SSLFW technique by applying it to a new dissimilar material pair, i.e., S45C steel and A6061 Al alloy. This is the case where there exists an extremely large difference in the temperature dependence of flow stress of the two dissimilar materials without a cross point between temperature-strength curves. The present chapter systematically investigates the influence of key process parameters such as preheating duration, applied pressure, and upset length on joint formation, interfacial microstructure, and mechanical performance. Emphasis is placed on identifying optimal processing conditions for achieving high-strength, defect-free joints. This chapter is largely based on the published manuscript titled ‘‘Process parameter optimization and bonding mechanism in dissimilar S45C/A6061 joints via novel sacrificing-sheet linear friction welding’’ authored by Furkan Khan, Takuya Miura, Yoshiaki Morisada, Kohsaku Ushioda, Hidetoshi Fujii in the *Journal of Advanced Joining Processes, 2025;12:100331*.

7.1. Introduction

The successful development of the novel SSLFW method presented in Chapter 6, demonstrating sound dissimilar joining SS400 steel and A7075 Al alloy, is extended in this chapter to a more challenging dissimilar material pair, i.e., S45C steel and A6061-T6 Al alloy, which exhibit significant strength differences across all temperature ranges. It

makes conventional LFW unsuitable due to the difficulty in removing surface oxides and achieving simultaneous interfacial deformation of mating materials regardless of the applied pressure. To address this, the SSLFW approach is applied, incorporating a preheating stage that selectively softens the S45C steel through frictional heating prior to pressurization towards the A6061 alloy.

The purposes of this chapter are to achieve effective joining of these two materials, viz. S45C steel and A6061-T6 Al alloy, and to determine the optimum operating conditions for the SSLFW process. The influence of key process parameters, such as preheating time, applied pressure, and upset length, on joint integrity, mechanical properties, and interfacial characteristics is systematically evaluated to establish optimal operating conditions. Furthermore, post-weld artificial aging treatment is applied to the optimized joint to enhance its mechanical performance, with particular focus on tensile strength and hardness recovery in the softened zone of Al alloy. Additionally, a comprehensive analysis of the joint microstructure and bonding mechanisms is conducted using advanced characterization techniques, including scanning electron microscope (SEM), electron backscatter diffraction (EBSD), and transmission electron Microscope (TEM), to provide deeper insight into the metallurgical phenomena governing the weld formation.

7.2. Base materials and experimental procedure

JIS A6061-T6 Al alloy (hereinafter referred to as A6061) and JIS S45C steel (hereinafter referred to as S45C) specimens with dimensions of 80 mm^{PD} x 20 mm^{OD} x 5 mm^{TD} were selected as the primary materials to be joined, where PD, OD and TD stand for pressure, oscillation and transverse directions. The 5 mm x 20 mm face was used as the friction surface. A 2 mm thick rectangular sheet (25 mm x 40 mm) made of S45C was

used as center sheet with the independent applied pressures towards A6061 and S45C sides. SSLFW was performed at an oscillation amplitude and frequency of 2 mm and 50 Hz, respectively. The Chemical compositions (wt.%) and UTS of these base metals are shown in Table 3-1 in Chapter 3.

To achieve SSLFW between A6061 and S45C, center-driven double-sided LFW equipment was utilized. The detailed joining concept of SSLFW process is explained in Chapter 6. Preheating of S45C side was performed by applying a pressure of 50 MPa (*P1*) for a certain preheat duration. Once the preheating time reached the set value, variable pressures (*P2*) of 100 MPa, 200 MPa, 300 MPa, and 400 MPa were applied towards A6061 to observe the effect on joints mechanical performance and interface microstructure. The upset length was kept 2 mm each side. Furthermore, keeping the preheating pressure 50 MPa towards S45C and applied pressure 300 MPa towards A6061, which resulted in the optimum joint conditions as discussed later, the upset lengths were varied from 0.5 mm, 1.0 mm, 1.5 mm, and 2 mm. The applied pressures of 50 MPa and 300 MPa were selected based on the temperature dependence behavior of materials' strengths, shown in Fig. 7-1. In this combination of steel and Al alloy, the temperature dependence curves suggest that both A6061 and S45C are expected to plastically deform when the temperature exceeded ~190℃ and ~600℃, respectively, under an applied pressure of 300 MPa (*P2*) as indicated by black arrows in Fig. 7-1. Temperature above 190℃ is assumed to be obtained by preheating and friction heating towards A6061 side, while the temperature above 600℃ can be achieved due to thermal conduction from S45C/S45C interface which have nearly ~930℃ under a preheat pressure of 50 MPa (*P1*). Furthermore, post-welding artificial aging treatment was carried out at the joint fabricated using optimum SSLFW conditions. The aging treatment was performed for

different aging times of 20 min, 1 h and 10 h at 170℃. Additionally, all the metallographic sample preparation and mechanical testing were performed as described in detail in Chapter 3.

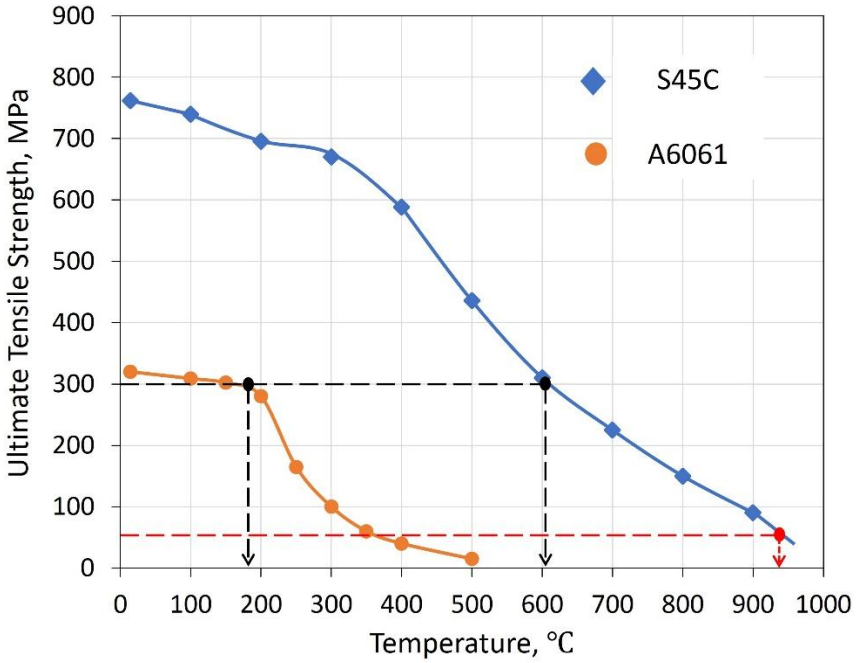

Fig. 7-1 Temperature dependence of UTS of S45C and A6061.

7.3. Results and discussion

7.3.1. Effect of upset length

Figs. 7-2(a-d) show the joint appearance of the fabricated welds at different amounts of upset length. The experiments were conducted by applying a preheating pressure of 50 MPa (*P1*) towards S45C. Preheating of steel was performed for a period of 1s. After the preheating time is reached, a pressure of 300 MPa (*P2*) was applied towards A6061. Furthermore, the upset was varied on each side from 0.5 mm to 2 mm with an interval of 0.5 mm in order to assess the effect on joint's mechanical performance. The fabricated weld coupon consisted of S45C steel and A6061 Al alloy, primary materials to be joined, and a center sheet as indicated by broken yellow arrows are shown in Figs. 7-2(a-d). The flash formation towards S45C is indicated by blue arrows, and that of the A6061 side is

not finely visible as it remains another side of the center sheet. Figs. 7-2(e-h) show the joint cross-sectional macrographs of the fabricated welds. Comparatively, lower upset length leads to partial joining and occurrence of several unjointed regions throughout interface, as pointed out by white arrows in Figs. 7-2e and f. As can be seen, in the case of 0.5 mm upset; only central region was joined whereas joining was not achieved towards edge of the weld, as indicated by white arrows in Fig. 7-2e, resulting in partial joining of the interface. In contrast, the occurrence of partial joining and presence of these unjointed regions were completely suppressed with further increase of upset as shown in Figs. 7-2g and h, ensuring sound joining.

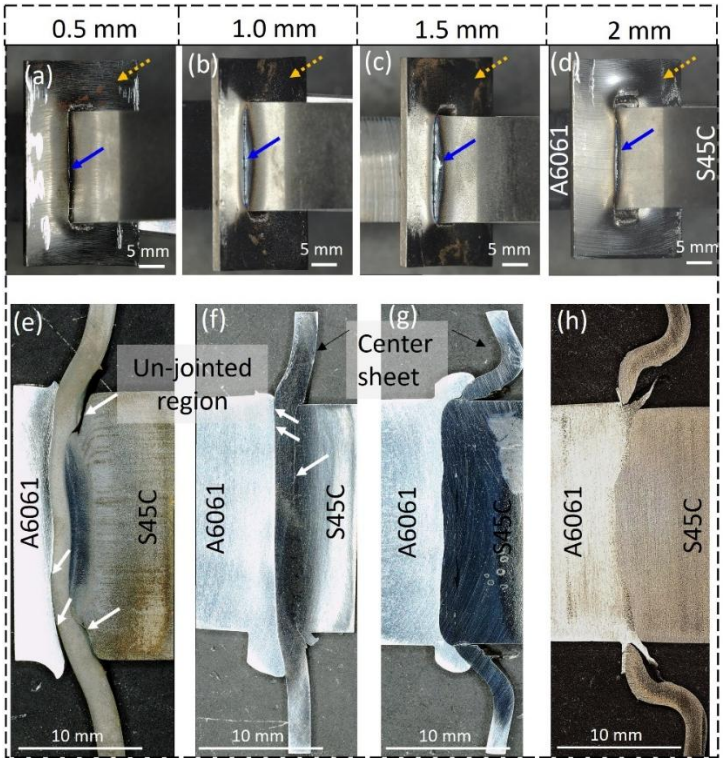

Figs. 7-2 Joint appearance of fabricated welds with upset lengths of; (a) 0.5 mm, (b) 1.0 mm, (c) 1.5 mm, (d) 2.0 mm; and (e-h) corresponding joint cross-sectional macrographs.

Furthermore, optical microscope was used to highlight the remained center sheet, if any, between the butt surfaces of the side materials on a magnified scale. Figs. 7-3(a-d) show the optical micrographs of SSLFW joint interfaces of the fabricated welds at

variable upset lengths of 0.5 mm, 1 mm, 1.5 mm, and 2.0 mm. The center sheet thickness between the butt surfaces of side materials was progressively reduced with the increase of upset. As the upset increased from 0.5 mm to 1.5 mm the center sheet thickness reduced from 2 mm to 0.49 mm due to progressive expulsion of center sheet, owing friction cycles and heating, revealing two joint interfaces, i.e., A6061/S45C, and S45C/S45C as indicated by black arrows in Fig. 7-3a. Furthermore, an upset value of 2 mm leads the center sheet to be completely expelled, which enabled direct joining between the side specimens resulting in single joint interface as shown in Fig. 7-3d. This is because the higher upset value leads to increased thermomechanical effect and friction cycles to achieve the targeted upset. Apart from this, un-jointed regions were identified in the case of lower upset values of 0.5 mm and 1 mm as indicated by red-rectangles, which may have greatly affected the weld strength, whereas, increased upset resulted in sound joining without defects.

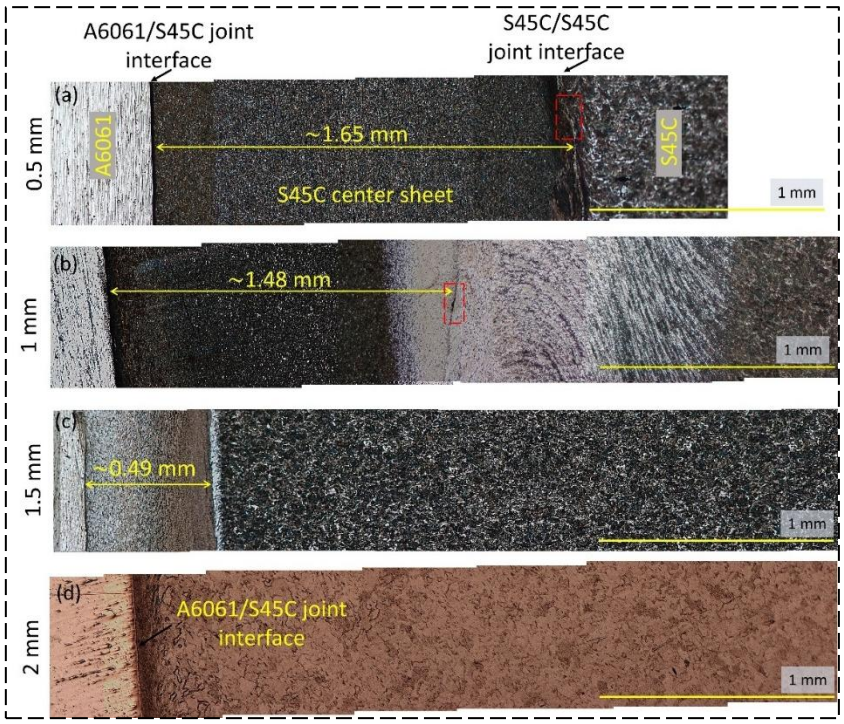

Fig. 7-3 Optical micrographs of joint cross-sections fabricated at different upset lengths of (a) 0.5 mm, (b) 1.0 mm, (c) 1.5 mm, (d) 2.0 mm.

7.3.2. Effect of applied pressure

Figs. 7-4(a-d) show the joint interface macrographs of the welds fabricated under different applied pressures of 100, 200, 300, and 400 MPa, respectively, towards A6061 with constant upset of 2 mm on each side. Evidently, the center sheet was expelled from the butt surfaces of side materials, as indicated by broken yellow arrows, enabling direct joining between S45C and A6061 alloy. It was thought that the center sheet was preferentially expelled around the central region, first, due to increased thermomechanical effect and intense heating near the central region followed by pullout of any remained center sheet towards the edge of the weld. The un-jointed regions were suppressed throughout the joining line ensuring a sound joining. However, in the case of 400 MPa applied pressure, defects were observed in the form of un-jointed regions as indicated by white arrow in Fig. 7-4d.

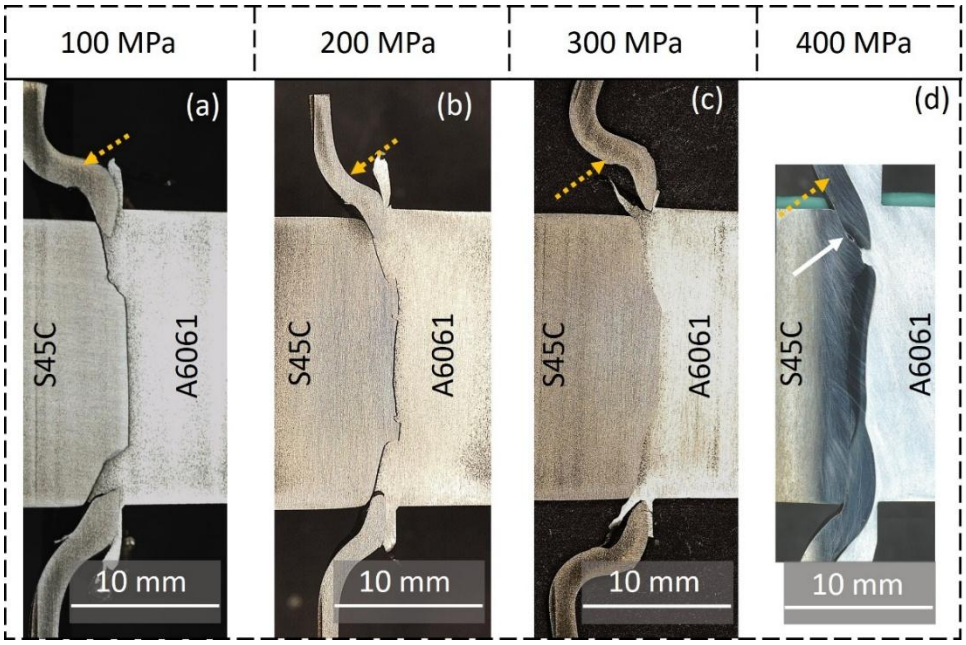

Fig. 7-4 Interface cross-sectional macrographs of the welds fabricated under an applied pressure of (a) 100 MPa, (b) 200 MPa, (c) 300 MPa, (d) 400 MPa.

7.3.3. Effect of pre-heating time

Figs. 7-5(a-d) show the joint cross-sectional macrographs of the welds fabricated

under different preheating durations. The applied pressure and upset length were kept constant at 300 MPa and 2 mm, respectively. Interface regions of the fabricated welds were analyzed to address the effect of preheating time on the weld quality. As can be seen in Fig. 7-5a, the weld fabricated without preheating revealed the presence of un-jointed regions throughout the joining line as indicated by white arrows. Additionally, the center sheet was observed to be remained within the butt surfaces of the side materials. Furthermore, the preheat duration of 0.5 s resulted in the partial suppression of these un-jointed regions. However, center sheet remained discontinuously within the butt surfaces of the side materials due to insufficient preheating. It causes an uneven joining interface throughout the weld line as shown in Fig. 7-5b. In contrast, as the preheat duration was further increased to 1 s and 1.5 s the un-jointed regions were completely suppressed, leading to the formation of a flat weld interface as shown in Figs. 7-5c and d, respectively. The complete suppression of un-jointed region and formation of a flat joining interface at increased preheat duration can be attributed to the thorough expulsion of center sheet from the joining area. It leads to the direct joining between S45C and A6061.

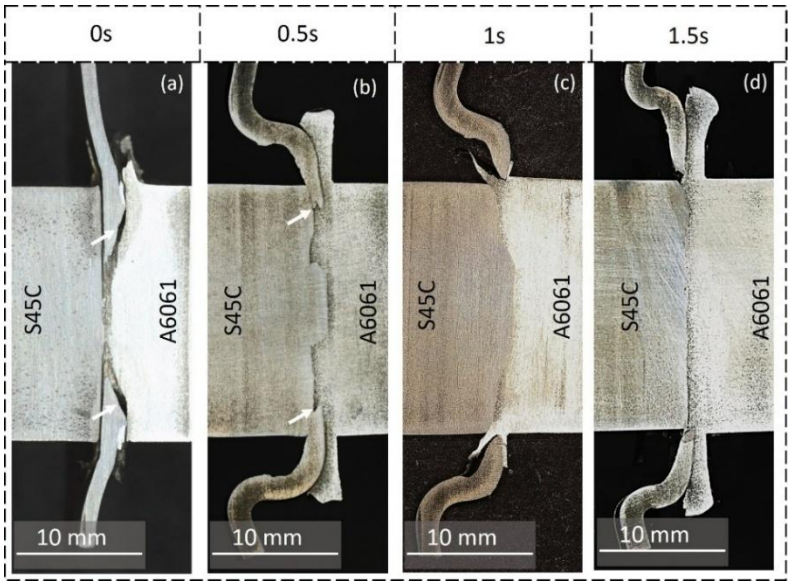

Fig. 7-5 Interface cross-sectional macrographs of the welds fabricated under various preheat durations of (a) 0 s (no preheat), (b) 0.5 s, (c) 1 s, (d)1.5 s.

7.3.4. Joint interface microstructure analysis

7.3.4.1. TEM analysis of joint interface

The effect of applied pressure on the joint interfacial characteristics, specifically formation of interface IMC thickness, was analyzed using TEM. Thin foil specimens were extracted from selected joint interfaces and prepared for TEM characterization. Figs. 7-6(a-g) present TEM micrographs alongside TEM-EDS line analyses of the fabricated joint interfaces. The IMC layers at the interfaces are outlined with single-dot chain lines. TEM-EDS analysis indicates that IMC layer thickness decreases with increasing applied pressure. Notably, at 100 MPa and 200 MPa, the IMC layer thicknesses were measured as approximately 1.23 μm and 0.56 μm, respectively, as seen in Figs. 7-6(a-i) and (b-i). The presence of a thick IMC layer at the dissimilar interface of steel-aluminum alloy may have negatively impacted the joint strength. Contrarily, under 300 MPa and 400 MPa pressures, extremely thin IMCs were observed. Under these conditions, TEM-EDS line scans were performed at higher magnifications, as shown in Figs. 7-6(d, f, g), due to the formation of extremely thin IMC layers. The corresponding line-scan graphs are shown in Figs. 7-6(d-i, f-i, g-i). The joint fabricated under 300 MPa exhibited a very thin and uniform IMC layer of ~0.10 μm as shown in Fig. 7-6(d-i)). Whereas under 400 MPa, IMC formation was discontinuous; as Fig. 7-6(f-i) shows no IMC presence, while Fig 7-6(g-i) reveals an extremely thin IMC layer. The reduction in IMC thickness with increased applied pressure may be attributed to a decrease in welding temperature, consistent with findings reported by Lim et al.[133].

Fig. 7-7 shows the microstructure of the base material and the joint interface region towards S45C and A6061 sides of the weld. The joint was fabricated with a 1 s preheat duration under 300 MPa applied pressure with 2 mm upset length. The microstructure observation was carried out by using SEM and EBSD for S45C and A6061 alloy,

respectively. The base metal of S45C was composed of ferrite and pearlite as indicated in Fig. 7-7a. After LFW, a microstructure consisting of a small amount of ferrite grains in the martensite matrix was observed as shown in Fig. 7-7b. The martensite formation was thought to occur due to the elevated temperature at S45C/S45C interface during the pre-heating phase, followed by rapid cooling of the fabricated weld. These results suggest that the temperature at the S45C/S45C interface during the pre-heating phase was increased to approximately the A_3 temperature, which leads to the formation of martensite. On the other hand, Figs. 7-7c and d show the EBSD-IPF maps of A6061 base metal and near the joint interface, respectively. The base metal of A6061 side contained a coarse grain structure with an average grain size of $\sim$59 μm. Notably, after LFW, the grains were significantly refined near the joint interface compared to the initial microstructure condition as shown in Fig. 7-7d. The refinement of grains can be attributed to the occurrence of dynamic recrystallization due to severe plastic deformation and localized frictional heating during LFW process. Dynamic recrystallization is an important phenomenon in solid-state welding processes like LFW. During LFW, the combination of severe plastic deformation and intense localized heating at the interface leads to the nucleation of new, fine grains, replacing the original coarse grains. After LFW, the average grain size towards A6061 was reduced to $\sim$4 μm near the joint interface. Therefore, evidently, the initial coarser grains are being consumed and new equiaxed grains are formed with substantially reduced size as moving from base metal toward the joint interface.

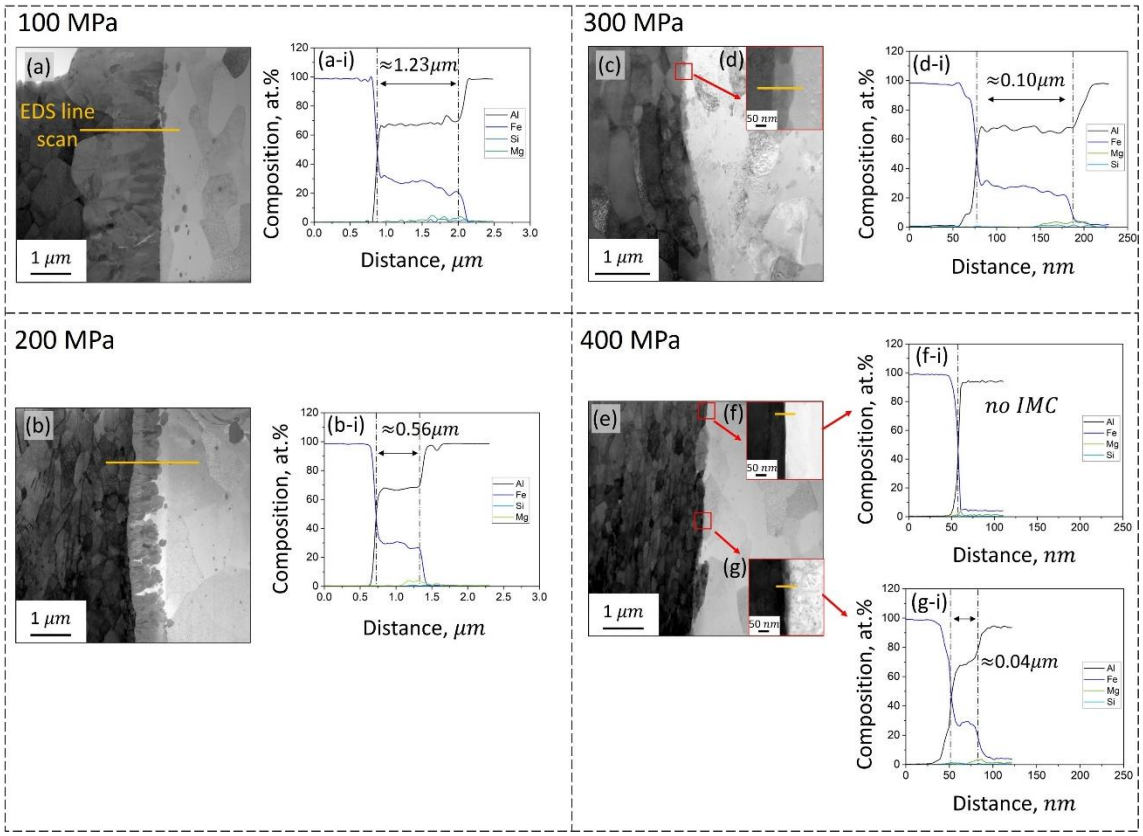

Fig. 7-6 TEM micrographs of joint interface fabricated at (a) 100 MPa, (b) 200 MPa, (c) 300 MPa, (e) 400 MPa; and alongside corresponding joint's TEM-EDS line scan analysis.

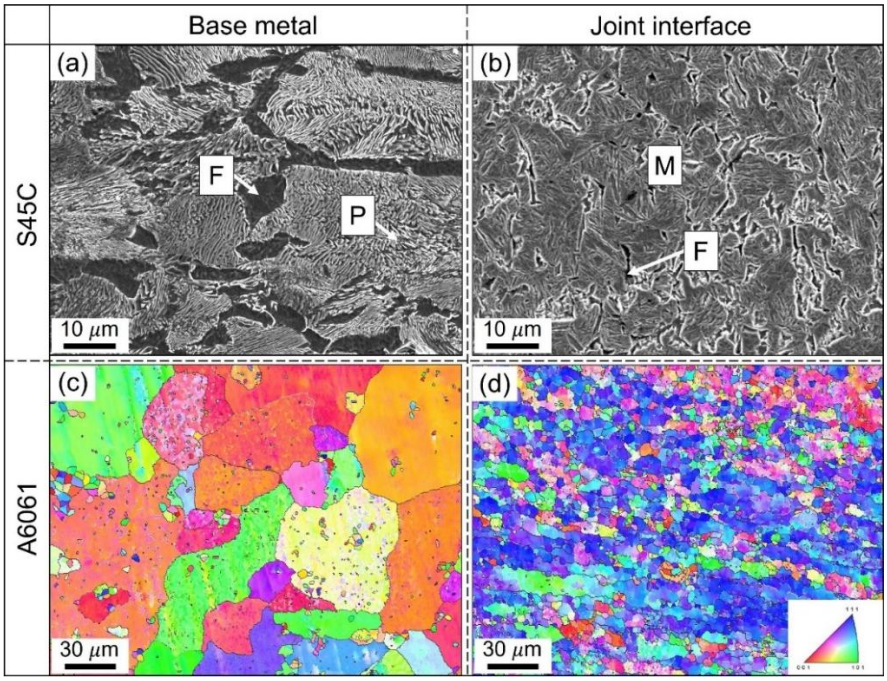

Fig. 7-7 SEM images showing microstructure of S45C (a) base metal, (b) joint interface; and EBSD-IPF maps of A6061 (c) base metal, (d) joint interface.

7.3.5. Mechanical performance of the fabricated welds

7.3.5.1. Weld tensile strength and fractured tensile specimen

Fig. 7-8 shows the effect of process parameters on the tensile performance of the fabricated welds. Fig. 7-8a shows that weld strength increases with increased upset and becomes saturated after certain limit. The welds fabricated at lower upset values of 0.5 mm and 1 mm resulted in poor joint strengths with an average value of ~66.8 MPa and ~130 MPa, respectively, with fracture at the interface. Lower upset values of 0.5 mm and 1.0 mm were thought to be insufficient to completely suppress the un-jointed regions, hence; negatively impacting the joint strength. In contrast, the joint produced with upset values of 1.5 mm and 2 mm effectively suppressed these un-jointed regions, leading to the enhanced joint strengths of ~233.2 MPa and ~235.3 MPa, respectively. Moreover, Fig. 7-8b shows the effect of applied pressure on the joint strength of fabricated welds. Joint tensile strength shows an increasing trend with the increase of applied pressure, reaches a peak value and starts declining. Specifically, joints fabricated under 100 MPa and 200 MPa show poor joining strengths with an average value of ~139 MPa and ~196 MPa, respectively. Poor joint strengths at lower applied pressures can be attributed to the formation of comparatively thicker IMC layer at the joint interfaces of S45C and A6061. While 300 MPa significantly reduced the interface IMC thickness which corresponds to the peak joint tensile strength of ~235.3 MPa. With a further increase in the applied pressure to 400 MPa, the joint exhibits a reduced tensile strength of approximately ~171 MPa, despite the formation of a very thin yet discontinuous IMC layer at the joint interface. This poor strength may be attributed to the appearance of joint defects in terms of unjointed regions due to very large applied pressure with respect to UTS of A6061[134]. Furthermore, Figs. 7-8c shows the influence of the preheating duration on the tensile strength of fabricated welds. Weld produced without preheating leads to poor joint

strength due to the formation of un-jointed regions throughout joining line. Similarly, weld produced with 0.5 s preheat duration resulted in comparatively improved but lower joint strength due to insufficient preheating to completely suppress the joint defects. Further increasing the preheating time to 1 s led to an improvement in joint strength. However, excessive preheating, such as at 1.5 s, resulted in a decline in joint strength. Therefore, based on the experimental results, a preheating duration of 1 s under an applied pressure 300 MPa with 2 mm upset value is associated with a recorded maximum tensile strength of ~235.3 MPa. This corresponds to a joint efficiency of over ~73 % with respect to A6061.

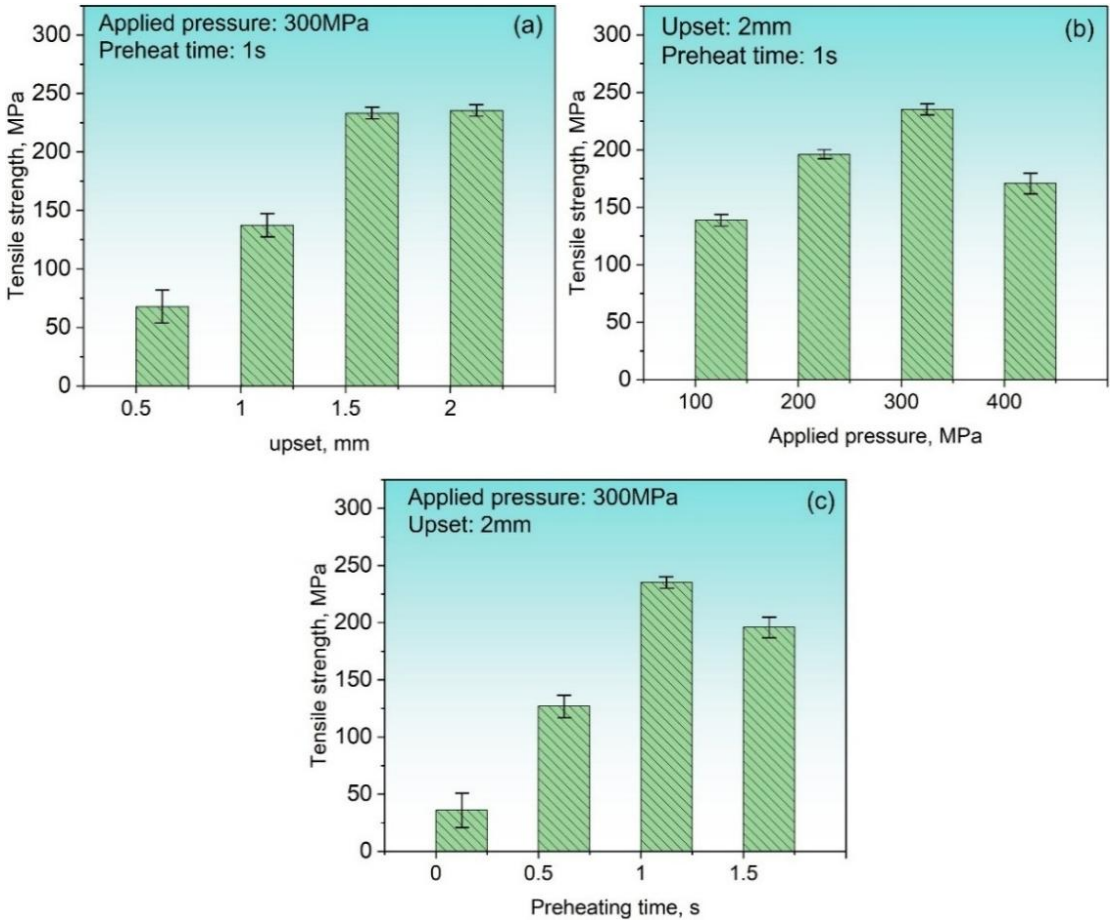

Fig. 7-8 Tensile strength of fabricated welds under various process parameters: (a) upset length, (b) applied pressure, (c) preheating time.

Figs. 7-9(a-d) depict the complete view of fractured tensile specimens of the joints fabricated under different applied pressures revealing their fracture locations. Additionally, a schematic of the tensile test specimen is shown in Fig. 7-9i. The joint interfaces and fracture locations are denoted by broken yellow and red arrows, respectively, in Figs. 7-9(e-h) presenting the magnified images of joint interfaces and fracture locations. Fracture modes of the obtained welds were improved with the increase of applied pressure up to certain value. Joint fabricated under an applied pressure of 100 MPa exhibited a brittle mode of fracture presumably through IMC layer, Fig. 7-9e. Whereas, the joint fabricated with 200 MPa applied pressure showed mixed fracture mode of ductile mode on A6061 side and brittle mode at the interface in Fig. 7-9f. Evidently, fracture behavior was improved significantly under 300 MPa applied pressure showing a fracture with necking towards A6061 side, and the fracture took place far from the joint interface, Fig. 7-9g. In contrast, fracture shifted to interface again under 400 MPa applied pressure as shown in Fig. 7-9h.

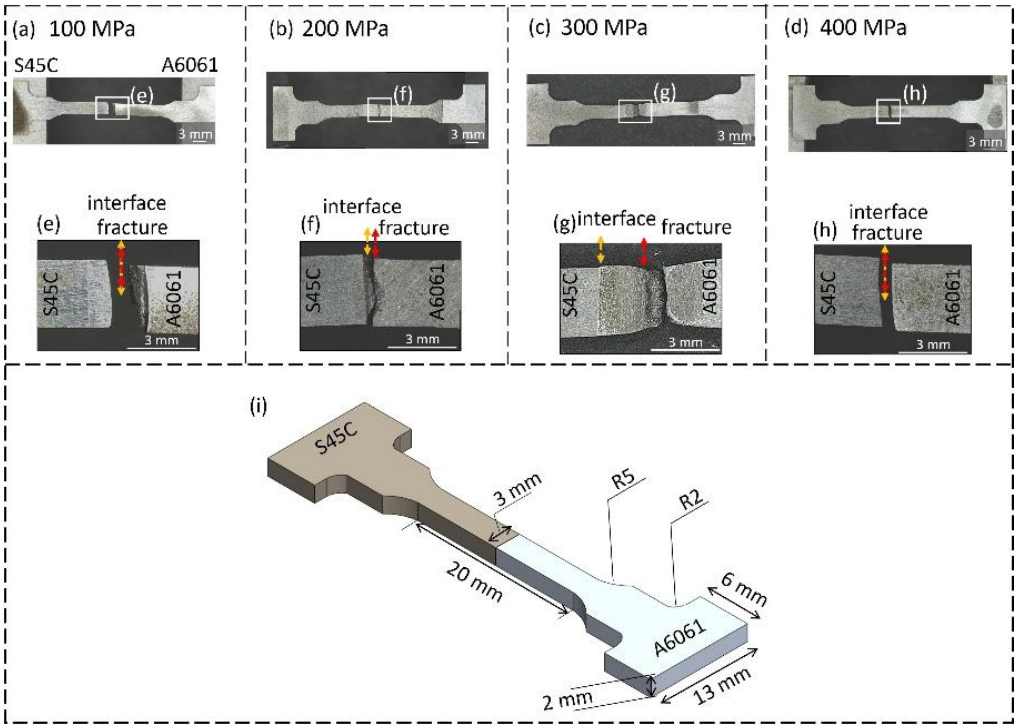

Fig. 7-9 Fracture tensile specimens of the welds fabricated at (a) 100 MPa, (b) 200 MPa, (c) 300 MPa, (d) 400 MPa; and (e-h) magnified images of joint interface and fracture locations, (i) schematic of used tensile test specimen.

7.3.5.2. Vickers microhardness distribution

The microhardness distributions on the joint cross-sections of the welds fabricated at various upset values and applied pressures are presented in Figs. 7-10a and 7-10b, respectively. Hardness distribution for 0.5 mm upset is not shown as the sample was broken during preparation. The microhardness distribution was observed to be significantly different on either side of the weld center line in each case. All the produced welds revealed a sharp increase in hardness moving from S45C base metal towards the joint interface, exhibiting peak hardness ranging from 540 Hv to 620 Hv. It is worth noting that under upset lengths of 1 mm and 1.5 mm, the microhardness value towards S45C reaches a peak and starts declining, as indicated by the black ellipses in Fig. 7-10a. This discrepancy in microhardness was thought to occur due to temperature gradient on the remaining center sheet within the butt surfaces of the side materials during SSLFW under

upset lengths of 1 mm and 1.5 mm, as seen in Figs. 7-3(b-c). Additionally, Fig. 7-10b shows the microhardness distribution of the welds fabricated under different applied pressures. Similarly, microhardness rapidly increases near the joint interface towards S45C side as compared to the base metal hardness. On the other hand, regardless of the given process parameters, all the produced welds show the occurrence of softening towards the A6061 side near the S45C/A6061 joint interface. The lowest hardness was always observed in the softened region of A6061 across the joint interfaces. The sharp hardness increase towards S45C is dominantly attributed to the presence of martensite, transformed from austenite during cooling due to elevated temperature at S45C/S45C interface. While the softening towards A6061 is caused by the dissolution of hardening particles despite the grain refinement hardening.

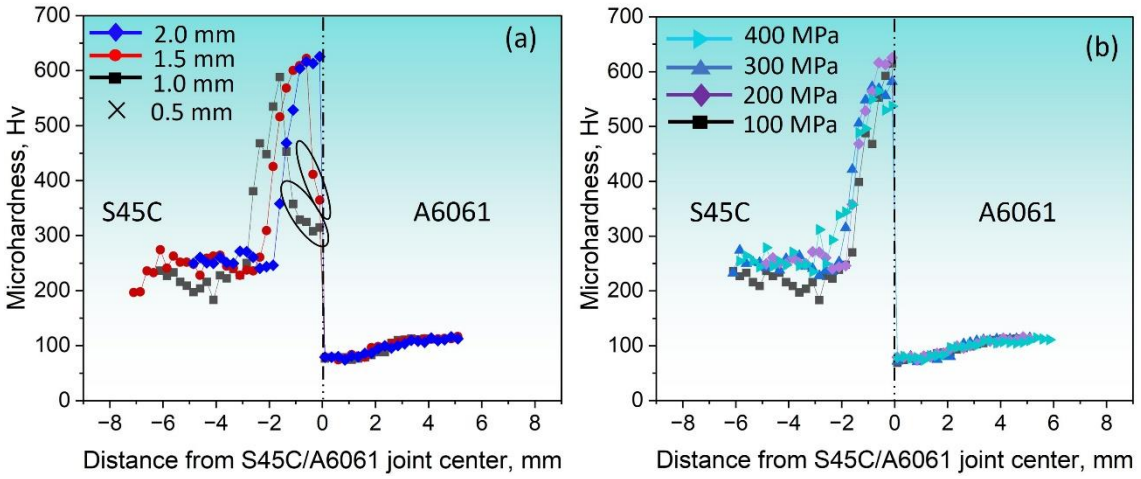

Fig. 7-10 Vickers microhardness distribution of the fabricated welds under different (c) upset lengths, (d) applied pressures.

7.3.6. Effect of artificial aging on microstructure and mechanical performance of the fabricated weld

7.3.6.1. Effect on microhardness and tensile strength

To assess the influence of artificial aging (AA) on the joint's mechanical performance, microhardness measurement and tensile tests were performed on the artificially aged

specimens and the observed results were compared with as-welded specimen. Artificial aging of specimens was carried out at 170℃ for 20 min, 1 h, and 10 h. Fig. 7-11 shows the microhardness profiles after aging-treatment and compared with as-welded condition. Black-broken horizontal line corresponds to the base metal hardness of A6061 alloy. Microhardness profiles provide an overview of anticipated mechanical behavior of the weldment. Aging for 20 min and 1 h contributed minimal to hardness recovery in softening zone of A6061 leading to minimum hardness point across the joint interface. Contrarily, a significant improvement is recorded in hardness towards A6061 side after 10 h of aging at 170 ℃, suppressing the softening region of A6061. The notable improvement in hardness may be attributed to the reprecipitation of very fine hardening particles during aging treatment which were dissolved during SSLFW due to elevated temperature. However, hardness recovery in the HAZ of A6061 remained slightly lower than that of the base material, indicating a localized minimum hardness region. Despite the significant improvement in hardness near joint interface, this minimum hardness point is likely due to the precipitates coarsening in the HAZ of A6061 alloy.

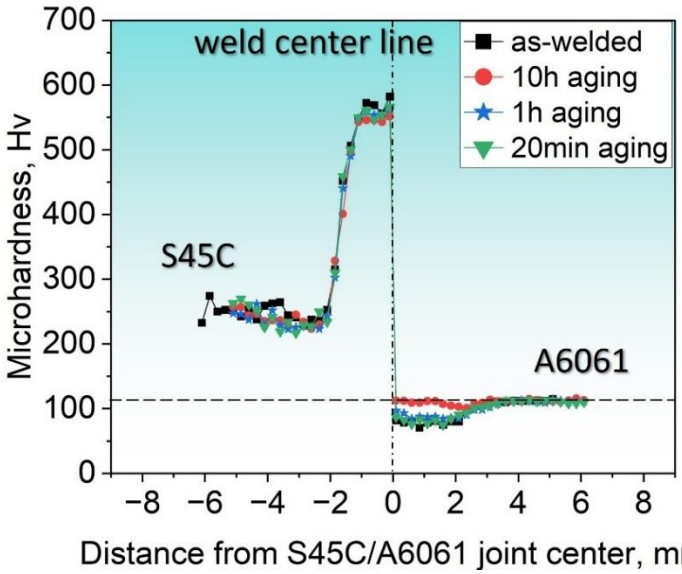

Fig. 7-11 Microhardness profile across the weldments after artificial aging at 170℃ for various aging time and compared with the as-welded specimen.

The hardness recovery induced by artificial aging is reflected in the tensile properties of the fabricated joints. The tensile properties of the weldments after aging are summarized in Table 7-2, along with the as-welded specimen for an intuitive view. Following to aging for 20 min and 1 h, the tensile strength improved marginally to about 236 MPa and 246 MPa which corresponds to a joint efficiency of nearly 74% and 77%, respectively, with respect to A6061 alloy. Furthermore, the notable hardness recovery after 10 h of artificial aging was evident in the tensile strength of the joint. As a result, post-weld aging for 10 h resulted in substantial improvement in tensile strength to 307 MPa, revealing a joint efficiency of ~96 % with respect to A6061 alloy.

Table 7-1. Tensile strengths of welds in as-welded and various aging treated conditions.

S. No.	Condition	Joint tensile strength (MPa)	Joint efficiency (%)	Tensile fracture location
1.	As-welded	235 ± 4	~73	A6061 side
2.	20min aging	236 ± 3	~74	A6061 side
3.	1h aging	246 ± 3	~77	A6061 side
4.	10h aging	307 ± 2	~96	A6061 side

7.3.6.2 TEM microstructure analysis of precipitates in A6061 alloy

Al-Mg-Si alloys belong to the class of age-hardenable Al alloys, offering a wide range of aging treatments to optimize their strength and hardness[135]. The primary hardening phase β" forms at aging temperatures of nearly 150-190°C and achieve an adequate distribution after ~10-20 h of aging[136,137]. The β'' precipitate has been the subject of significant research interest due to its strong correlation with peak-aged conditions[138]. Figs. 7-12(a-c) present TEM micrographs of A6061 base metal (BM), as-welded specimen, and the post-weld aging treated specimen (aged for 10 h at 170°C),

respectively. Figs. 7-12(d-f) provide higher-magnification images of the selected regions in Figs. 7-12(a-c), respectively. The BM of A6061 exhibited a high density of finely dispersed precipitates, approximately 2.0-3.0 nm in size, aligning with hardening β'' precipitate sizes of 2.2-3.0 nm reported in previous studies[139,140], suggesting a co-existence of clusters and β'' phase. In contrast, SSLFW led to the complete dissolution of these very fine unstable β'' precipitates due to the elevated temperatures during welding, resulting in a localized reduction in hardness. However, within the softened region, sparse but coarser precipitates were observed (Fig. 7-12e). Following post-weld aging at 170°C for 10 h, a high density of very fine β'' precipitates (2.0-3.0 nm) retrieved and became the dominant microstructural feature, as shown in Fig. 7-12f. This aging treatment significantly enhanced the alloy's hardness, indicating that the fine β'' precipitates play a crucial role in strengthening. Furthermore, the significant increase in hardness after 10 h of aging, in contrast to the negligible improvement observed after 20 min and 1 h of aging, suggests a time-dependent strengthening behavior. The clusters after short term aging accelerate the strengthening response of the alloy, likely by modifying the cluster composition to that of the strengthening precipitates β'' [140]. This is in well agreement with the results of tensile strength summarized in Table 7-2 and hardness results observed in Fig 7-11.

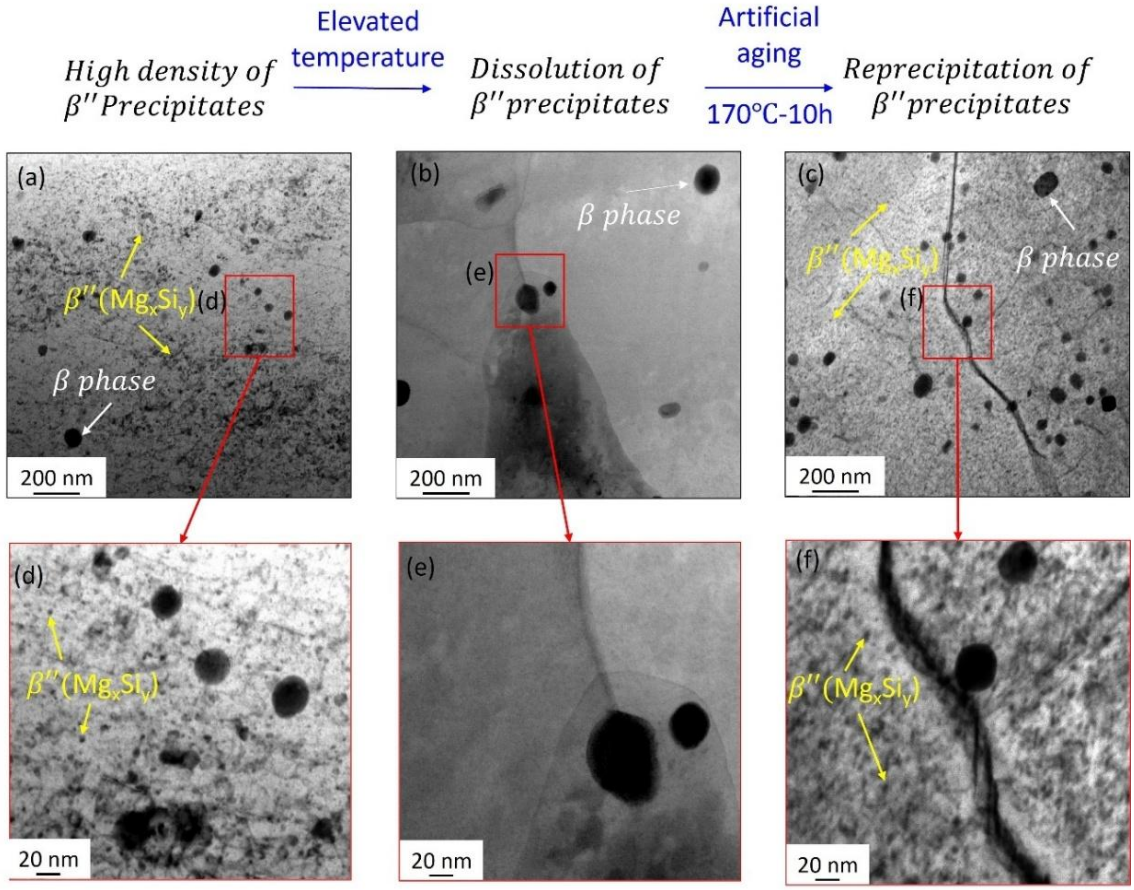

Fig. 7-12 TEM micrographs of (a) A6061 BM, (b) as-welded specimen, (c) post weld; aging treated specimen at 170℃ for 10h; and (d-f) higher magnification images of the red rectangles in (a-c), respectively.

7.4. Conclusions

The operating conditions of novel sacrificing-sheet linear friction welding (SSLFW) method to directly join S45C and A6061 using S45C sheet as a center-driven material were optimized by investigating the influence of various weld parameters. The influences of preheat time, upset length and applied pressures on mechanical performance and joint interface microstructure were assessed and joining mechanism was elucidated. Furthermore, the post-weld artificial aging treatment of the optimized joint was subjected to explore the joints' strength reachable exploiting the new welding technique of SSLFW. The key conclusions are summarized as follows:

1. Sound dissimilar joint between S45C steel and A6061 Al alloy can be achieved by oscillating a center sheet of S45C steel and establishing a preheating stage that heats only S45C for a certain period of time utilizing a novel SSLFW method.
2. When the center sheet of S45C steel was preheated for 1s duration under a pressure of 50 MPa, followed by pressurization at 300 MPa towards the A6061 alloy with 2 mm upset length, the unjointed regions were effectively suppressed. A uniform IMC layer with a minimized thickness of approximately 100 nm was identified at the dissimilar joint interface. As a result, this set of process parameters resulted in the optimized process conditions revealing maximum joint strength of ~235.3 MPa, which corresponds to over 73 % joint efficiency concerning A6061 alloy.
3. Lower upset lengths of 0.5 mm and 1.0 mm led to partial joining and occurrence of several un-jointed areas throughout the weld interface which adversely affected the joint strength and resulted in poor joining.
4. IMC layer thickness at the dissimilar joint interface of S45C steel and A6061 alloy was observed to be reduced with the increase of applied pressure towards A6061, reducing the brittleness of the dissimilar joint. As a result, the fracture mode was improved and the joint fabricated at an optimum 300 MPa applied pressure exhibited a fracture with necking towards A6061 side.
5. The recovered microhardness in the softening zone of A6061 alloy was almost comparable to that of base metal after 10 h of artificial aging at 170℃. Hardness recovery is reflected in the joint tensile strength, which was improved from ~235.3 MPa in as-welded state to ~307 MPa after artificial aging, indicating a substantial improvement in joint efficiency from 73 % to 96 % with respect to A6061 alloy BM.

Chapter 8: Conclusions and future work

8.1. Conclusions

This thesis focuses on the linear friction welding (LFW) method, capable to precisely control the joining temperature, of dissimilar combination of steel and Al alloys. The efforts were invested to achieve high-quality dissimilar joining between steel and Al alloys using LFW.

Chapter 1 introduced the overview of the study.

Chapter 2 presented a comprehensive literature review of previous studies on the dissimilar joining of steel and Al alloys; emphasis was placed on the LFW process. The necessity of dissimilar joining of steel and Al alloys from the viewpoint of multi-materialization was presented, and the challenges of dissimilar material joining using conventional joining methods were described in Chapter 2. The conclusions from the literature review allowed for the thesis aim and objectives to be identified as mentioned in detail in Section 2.5.2.

For clarity and emphasis, the primary objectives of the present study are restated as follows.

- Previous studies on LFW of carbon steel and Al alloys suffers to prevent fracture at the joint interface, primarily due to the formation of brittle intermetallic-compound (IMC) layer and lack of simultaneous interfacial deformation of mating materials during welding. Therefore, in this study, efforts are invested to enhance joint efficiency and fracture mode of steel and Al alloy dissimilar weld by promoting simultaneous interfacial deformation of mating materials. This was achieved by exploiting cross-point concept of temperature-strength curves, with aim of producing sound dissimilar joint between steel and Al alloys with minimized IMC thickness at

the interface.

- To systematically explore the process parameters of center-driven double-sided (CDDS)-LFW and to achieve sound dissimilar joint between steel and Al alloys couple, which have a cross-point at extremely low temperature or lack a cross-point in their temperature-strength curves. The primary objective is to enhance joint efficiency and improve fracture mode while overcoming the inherent challenges of the CDDS-LFW method that previous study has faced.
- To explore strategies for further enhancing joint strength of steel and Al alloy dissimilar weld. Since the joint strength in CDDS-LFW can be limited by the strength of the center material, efforts have been invested to eliminate this dependency and improve overall joint performance. Building upon these efforts, a novel joining method termed as sacrificing-sheet linear friction welding (SSLFW) was developed and utilized to effectively weld dissimilar couples of steel and Al alloys that are particularly difficult to be joined by using conventional LFW. Consequently, SSLFW is expected to offer a promising solution to the limitations faced in CDDS-LFW and holds potential for further improving joint strength in dissimilar material welding.

Chapter 3 presented materials and the main methodologies and techniques employed for the materials preparation, LFW joining equipment and process, metallurgical and mechanical characterization.

The first objective point was primarily addressed in Chapter 4. In this, direct LFW was attempted and sound dissimilar joint was obtained between mild steel (MS) and A7075 Al alloy by optimization of welding parameters. Under an applied pressure of 300 MPa, corresponding to the cross-point strength on temperature-strength curves of both alloys, the simultaneous interfacial deformation of both alloys was promoted during

welding, which leads to suppressing the interfacial joint defects. Additionally, an extremely thin IMC layer of ~34.7 nm thickness was identified at the dissimilar joining interface. As a result, the fabricated weld revealed excellent joint strength exhibiting 100 % joint efficiency with re spect to MS. The fracture was located in the base metal region of MS. To the best of author's knowledge, this is the first study to report 100 % joint efficiency between A7075 and any iron-based alloy dissimilar LFW joint, and exhibiting a base metal fracture towards steel side.

The second objective point was addressed in Chapter 5. Chapter 5 reports the dissimilar joining of SS400 and A7075 Al alloy. The challenges during conventional LFW between SS400/A7075 were identified, and a promising solution was presented using CDDS-LFW method. Conventional direct LFW between SS400/A7075 was difficult due to the absence of interfacial deformation towards SS400 during welding, which led to several un-jointed regions throughout the joint interface and eventually resulted in a poor joint strength exhibiting an interfacial fracture. Therefore, CDDS-LFW is employed to effectively weld SS400 and A7075 Al alloy. MS was selected as the center material because temperature-strength curves of MS and A7075 possess a cross-point, and MS also has the temperature at which material strength is almost equal to SS400. The interface temperatures were controlled by changing the applied pressures, corresponding to the cross-point strengths at each interface. CDDS-LFW promoted the simultaneous interfacial deformation of the mating materials at both MS/A7075 and MS/SS400 interfaces by exploiting the cross-point concept. As a result, obtained joint exhibited a superior tensile strength of ~347.5 MPa compared to the past investigations of SS400 with any Al alloy joints, revealing 100 % joint efficiency concerning MS, and the fracture took place in the base metal region of MS, away from both the joint interface, i.e.,

SS400/MS and MS/A7075.

One potential drawback of the study in this Chapter 5 may be that, although, the joint efficiency reaches 100 % concerning MS base metal, the joint strength was inherently limited by the strength of center material, i.e., MS base metal itself. It indicated the ongoing challenges to further improve the joint strength of SS400/A7075 dissimilar joint. Also, it raises further concerns about the need to develop the process to enhance the joint strength and remove the dependence of weld strength on the strength of center material. Therefore, the authors believe that a stronger joint may be obtained by systematically employing alternative strategies to fabricate high-quality dissimilar weld with enhanced joint strength.

In Chapter 6, a novel sacrificing-sheet linear friction welding (SSLFW) method, by oscillating a center sheet of SS400 steel utilizing the CDDS-LFW machine, was exploited to further enhance the joint strength of dissimilar weld between SS400 and A7075 Al alloy. In this novel method, by establishing a preheating stage that frictionally heats only SS400 side for a certain period of time, the center sheet was effectively expelled from the joint interface, and SSLFW that directly joins the SS400 and A7075 has been achieved. Without preheating, several unjointed regions were identified and center sheet remained within the butt surfaces of side materials resulting in uneven joining interface. Furthermore, IMCs layer thickness at dissimilar joint interface was minimized with increase in welding pressure accompanied by increased forging speed. Consequently, joints produced exploiting SSLFW revealed the maximum joint strength of 448 MPa, exhibiting a joint efficiency of 93 % with respect to base metal strength of softer SS400. This indicates a significant improvement over the CDDS-LFW method for SS400/A7075 dissimilar joints in Chapter 5, effectively overcoming its strength limitation of ~347.5

MPa.

SSLFW technique offers a significant advancement over the CDDS-LFW method by enabling the effective expulsion of the center sheet from the joint interface during welding. In the CDDS-LFW approach, the joint strength was inherently limited by the strength of the center material, which remains at the interface and becomes the weakest portion in the joint. In contrast, SSLFW eliminates this dependency by expelling center sheet from the joining interface, enabling direct joining between the side materials. Thereby enhancing the overall mechanical performance of the joint. This novel approach not only enhances joint strength but also addresses a critical challenge in dissimilar material joining, particularly when joining the materials with significantly different mechanical and thermal properties, and opens new possibilities for fabricating high-strength, light weight structural components.

Chapter 7 aimed to further explore the applicability of SSLFW method by applying it to a more challenging dissimilar material combination, i.e., S45C and A6061 Al alloy, which exhibit significant strength difference across all temperature ranges. The operating conditions of novel SSLFW method were optimized by investigating the influence of key process parameters, i.e., preheat time, upset length and applied pressures, on mechanical properties and interfacial microstructure. Obtained results indicate that defect free, sound joint with high joint strength can be achieved using optimum welding parameters. Additionally, optimum process conditions were proved to contribute to the simultaneous deformation of both materials through sacrificing role of center sheet together with formation of the very thin uniform IMC layer with a thickness of about 100 nm. Consequently, the optimum joint revealed a peak tensile strength of ~235.3 MPa in the as-welded condition. Furthermore, the hardness recovery induced by aging treatment

significantly enhanced the joint strength to ~307 MPa and increased joint efficiency from ~73% in the as-welded condition to ~96% with respect to A6061 Al alloy.

8.2. Future works

Building upon the findings of the study as presented in Chapters 6 and 7, several avenues for future research are proposed to further advance the understanding and application of the novel SSLFW method.

I. Investigation to other dissimilar material combination

While this study successfully demonstrated the feasibility of SSLFW for joining particular dissimilar ferrous/non-ferrous combinations such as SS400/A7075 and S45C/A6061, the broader applicability of the technique remains to be explored. Future research would investigate the extension of this approach to other challenging dissimilar materials pairs that are commonly utilized in structural applications. These may include, but are not limited to, nickel super alloy/austenitic stainless-steel, titanium/aluminum, stainless steel/magnesium, and copper/aluminum alloy combinations. Success in these dissimilar combinations could position SSLFW as a versatile solid-state joining method for advanced multi-material assemblies in the aerospace and automotive industries.

II. Fatigue and corrosion performance evaluation

The present work focuses on the process optimization, tensile strength and joint interface microstructural characterization of SSLFW. However, long-term durability assessments under service-like conditions remains a critical concern for structural applications in aerospace industries, where materials such as A7xxx series alloy are widely used for their excellent strength-to-weight ratio. Therefore, future work would address the fatigue resistance and corrosion behavior of SSLFW joints.

References

1. Hanifa, M., Agarwal, R., Sharma, U., Thapliyal, P. C. & Singh, L. P. A review on CO_2 capture and sequestration in the construction industry: Emerging approaches and commercialised technologies. J CO_2 Util. 67, 102292 (2023).

2. Solomon, S., Climate Change 2007: The Physical Science Basis: Working group I contribution to the fourth assessment report of the intergovernmental panel on climate change. (Cambridge University Press, 2007) (2007).

3. Fawzy, S., Osman, A. I., Doran, J. & Rooney, D. W. Strategies for mitigation of climate change: a review. Environ Chem Lett 18 2069–2094 (2020).

4. Masson-Delmotte, V., Zhai, P., Portner, HO., Roberts, D., Skea, J., Shukla, PR., Pirani, A., et al. Global warming of 1.5℃. An IPCC special report on the impacts of global warming of 1.5℃ above pre-industrial levels and related global greenhouse gas emission pathways (2018).

5. Masson-Delmotte, V., Psnmon, Z., Hans-Otto, P., Debra, R. et. al. Global Warming of 1.5°C (Cambridge University Press, 2022) (2022).

6. Hsieh, M. J., Lee, R. T. & Chiou, Y. C. Friction stir spot fusion welding of low-carbon steel to aluminum alloy. J Mater Process Technol 240, 118–125 (2017).

7. Kar, A., Vicharapu, B., Morisada, Y. & Fujii, H. Elucidation of interfacial microstructure and properties in friction stir lap welding of aluminium alloy and mild steel. Mater Charact 168 (2020).

8. Zhang, D., Qin, G., Geng, P. & Ma, H. Study of plastic flow on intermetallic compounds formation in friction welding of aluminum alloy to stainless steel. J Manuf Process 64, 20–29 (2021).

9. Dong, H., Yang, J., Li, Y., Xia, Y., et al. Evolution of interface and tensile properties in 5052 aluminum alloy/304 stainless steel rotary friction welded joint after post-weld heat treatment. J Manuf Process 51, 142–150 (2020).

10. Mahto, R. P., Kumar, R., Pal, S. K. & Panda, S. K. A comprehensive study on force, temperature, mechanical properties and micro-structural characterizations in friction stir lap welding of dissimilar materials (AA6061-T6 & AISI304). J Manuf Process 31, 624–639 (2018).

11. Yao, Y., Jing, L., Wang, S., Li, G., et al. Mechanical properties and joining mechanisms of Al-Fe magnetic pulse welding by spot form for automotive application. J Manuf Process 76, 504–517 (2022).

12. Gullino, A., Matteis, P. & Aiuto, F. D. Review of aluminum-to-steel welding technologies for car-body applications. Metals, 9 315 (2019).

13. Ohhama, S., Hata, T., Yahaba, T., Kobayashi, T., Miyahara, T., Sayama, T., Application of an FSW continuous welding technology for steel and aluminum to an automotive subframe. in SAE Technical Papers vol. 2 (SAE International, 2013) (2013).

14. Beygi, R. Galvao, I., Safar, A., Pouraliakbar, H., Fallah, V., Silva, LFM.. Effect of Alloying Elements on Intermetallic Formation during Friction Stir Welding of Dissimilar Metals: A critical review on aluminum/steel. Metals, 13, 768. (2023).

15. Howlader, M. M. R., Kaga, T. & Suga, T. Investigation of bonding strength and sealing behavior of aluminum/stainless steel bonded at room temperature. Vacuum 84, 1334–1340 (2010).

16. Rans, C., Straznicky, P. V. & Alderliesten, R. Riveting process induced residual stresses around solid rivets in mechanical joints. J Aircr 44, 323–329 (2007).

17. Zhang, H. & Liu, J. Microstructure characteristics and mechanical property of aluminum alloy/stainless steel lap joints fabricated by MIG welding-brazing process. Mater Sci Eng A 528, 6179–6185 (2011).

18. Bhamji, I., Preuss, M., Threadgill, PL., Richard, M., Addison, A., Peel M. Linear friction welding of AISI 316L stainless steel. Mater Sci and Eng: A 528, 680–690 (2010).

19. Akbarimousavi, SAA., GohariKia, M. Investigations on the mechanical properties and microstructure of dissimilar cp-titanium and AISI 316L austenitic stainless steel continuous friction welds. Mater Des 32, 3066–3075 (2011).

20. Mehta, K. P. A review on friction-based joining of dissimilar aluminum-steel joints. J Mater Res. 34 78–96 (2019).

21. Hussein, S. A., Tahir, A. S. M. & Hadzley, A. B. Characteristics of aluminum-to-steel joint made by friction stir welding: A review. Mater Today Commun 5, 32–49 (2015).

22. Lim, Y., Lim, Y., Squires, L., Pan, T., Miles, M., et al. Study of mechanical joint strength

of aluminum alloy 7075-T6 and dual phase steel 980 welded by friction bit joining and weld-bonding under corrosion medium. Mater Des 69, 37–43 (2015).

23. Lim, Y., Squires, L., Pan, T., Miles, M., et al. Corrosion behaviour of friction-bit-joined and weld-bonded AA7075-T6/galvannealed DP980. Sci Tech Weld Join 22, 455–464 (2017).

24. Su, Y., Hua, X. & Wu, Y. Effect of input current modes on intermetallic layer and mechanical property of aluminum-steel lap joint obtained by gas metal arc welding. Mater Sci Eng A 578, 340–345 (2013).

25. Su, Y., Hua, X. & Wu, Y. Influence of alloy elements on microstructure and mechanical property of aluminum-steel lap joint made by gas metal arc welding. J Mater Process Technol 214, 750–755 (2014).

26. Wang, P., Chen, X., Pan, Q., Madigan, B. & Long, J. Laser welding dissimilar materials of aluminum to steel: an overview. Int J Adv Manuf Tech 87, 3081–3090 (2016).

27. Song, J. L., Lin, S. B., Yang, C. L. & Fan, C. L. Effects of Si additions on intermetallic compound layer of aluminum-steel TIG welding-brazing joint. J Alloys Compd 488, 217–222 (2009).

28. Hu, S., Haselhuhn, A., Ma, Y., Li, Z., et al. Effect of external magnetic field on resistance spot welding of aluminium to steel. Sci Tech Weld Join 27, 84–91 (2022).

29. Hu, S., Haselhuhn, A., Ma, Y., LI, Y., et al. Sensitivity of dissimilar aluminum to steel resistance spot welds to weld gun deflection. J Manuf Process 68, 534–545 (2021).

30. Yang, Y., Luo, Z., Zhang, Y. & Su, J. Dissimilar welding of aluminium to steel: A review. J Manuf Process 110 376–397 (2024).

31. Dong, H. G., Hu, W. J. & Zhang, X. C. Detachment of interfacial layers during arc-brazing of Aluminum alloy to carbon steel with filler wire. Trans Nonferrous Met Soc China (English Edition) 23, 1583–1588 (2013).

32. Yang, T., Dai, W., Zhuang, Y., Liu, J., et al. Investigation on the control of interfacial layer uniformity in laser-metal inert-gas hybrid welded-brazed Al/steel butt joint. J Manuf Process 58, 1241–1250 (2020).

33. Kweon, J. H., Jung, J. W., Kim, T. H., Choi, J. H. & Kim, D. H. Failure of carbon

composite-to-aluminum joints with combined mechanical fastening and adhesive bonding. Compos Struct 75, 192–198 (2006).

34. Fukumoto, S., Tsubakino, H., Okita, K., Aritoshi, M. & Tomita, T. Friction welding process of 5052 aluminium alloy to 304 stainless steel. Mater Sci Technol, 15, 1080-1086 (2013).

35. Kawai, G., Ogawa, K., Ochi, H. & Tokisue, H. Friction weldability of aluminium alloys to carbon steel. Weld Int 14, 101–107 (2000).

36. Lee, W. B., Yeon, Y. M., Kim, D. U. & Jung, S. B. Effect of friction welding parameters on mechanical and metallurgical properties of aluminium alloy 5052 - A36 steel joint. Materials Science and Technology 19, 773–778 (2003).

37. Kimura, M., Suzuki, K., Kusaka, M. & Kaizu, K. Effect of friction welding condition on joining phenomena and mechanical properties of friction welded joint between 6063 aluminium alloy and AISI 304 stainless steel. J Manuf Process 26, 178–187 (2017).

38. Ambroziak, A., Korzeniowski, M., Kostron, P., Winnicki, M., Sokolowski, P., Harapinska, E. Friction welding of aluminium and aluminium alloys with steel. Adv Mater Sci Eng, 981653 (2014).

39. Saleh, M., Liu, H., Ushioda, K. & Fujii, H. Effect of Zn interlayer on friction stir butt welding of A1100 and SUS316L stainless steel. Sci Tech Weld Join 27, 361–373 (2022).

40. Saleh, M., Morisada, Y., Ushioda, K. & Fujii, H. Improvement of weldability and fracture behavior of mild steel and A7075 aluminum alloy dissimilar friction stir welded joints by increasing welding speed. Mater Today Commun 37, (2023).

41. Tanaka, T., Morishige, T. & Hirata, T. Comprehensive analysis of joint strength for dissimilar friction stir welds of mild steel to aluminum alloys. Scr Mater 61, 756–759 (2009).

42. Kimura, M., Suzuki, K., Kusaka, M. & Kaizu, K. Effect of friction welding condition on joining phenomena, tensile strength, and bend ductility of friction welded joint between pure aluminium and AISI 304 stainless steel. J Manuf Process 25, 116–125 (2017).

43. Cai, W., Daehn, G., Vivek, A., Li, J., Khan, H., Mishra, RS., Komarasamy, M. A state-of-the-art review on solid-state metal joining. Journal of Manufacturing Science and

Engineering, J Manuf Sci Eng, 141, 031012 (2019).

44. Pashazadeh, H., Masoumi, A. & Teimournezhad, J. A study on material flow pattern in friction stir welding using finite element method. Proc Inst Mech Eng B J Eng Manuf 227, 1453–1466 (2013).

45. Thomas, W. M., Threadgill, P. L. & Nicholas, E. D. Feasibility of friction stir welding steel. Sci Tech Weld Join, 4, 365-372 (1999).

46. Mitlin, D., Radmilovic, V., Pan, T., Chen, J., et al. Structure-properties relations in spot friction welded (also known as friction stir spot welded) 6111 aluminum. Mater Sci Eng A 441, 79–96 (2006).

47. Gao, Z., Niu, J., Krumphals, F., Enzinger, N., et al. FE modelling of microstructure evolution during friction stir spot welding in AA6082-T6. Weld World 57, 895–902 (2013).

48. Maalekian, M. Friction welding - Critical assessment of literature. Sci Tech Weld Join, 12 738–759 (2007).

49. Uday, M. B., Fauzi, M. N. A., Zuhailawati, H. & Ismail, A. B. Advances in friction welding process: A review. Sci Tech Weld Join, 15 534–558 (2010).

50. Maalekian, M., Kozeschnik, E., Brantner, H. P. & Cerjak, H. Comparative analysis of heat generation in friction welding of steel bars. Acta Mater 56, 2843–2855 (2008).

51. Richter W. Creation of an adhesive bond between plaques of tool steel and their supports in the manner of welding or soldering. (1929).

52. James Kauzlarch, B. J. 8 2-3-4 2-72 ATTORNEYS. vol. 3 (1969).

53. Vairis, A. & Frost, M. High Frequency Linear Friction Welding of a Titanium Alloy. Wear, 217, 117-131 (1998).

54. Dalgaard, E., Wanjara, P., Gholipour, J., Cao, X. & Jonas, J. J. Linear friction welding of a near-β titanium alloy. Acta Mater 60, 770–780 (2012).

55. Wanjara, P., Jahazi, M. Linear friction welding of Ti-6Al-4V: Processing, microstructure, and mechanical-property inter-relationships. Metall Mater Trans A, 36, 2149-2164 (2005).

56. Mary, C. & Jahazi, M. Linear friction welding of IN-718 process optimization and microstructure evolution. Adv Mater Res, 15–17 357–362 (Trans Tech Publications, 2007).

57. Gangil, N., Mishra, A., Lone, NF., Bajaj, D., et al. Linear Friction Welding of Similar and Dissimilar Materials: A Review. Met Mater Int, 31, 1-21 (2024).

58. Vairis, A. & Frost, M. Modelling the Linear Friction Welding of Titanium Blocks. Mater Sci Eng A, 292, 8-17 (2000).

59. Vairis, A. & Frost, M. On the Extrusion Stage of Linear Friction Welding of Ti 6Al 4V. Mater Sci Eng A, 271, 477-484 (1999).

60. Khan, F., Ito, T., Miura, T., Morisada, Y., et al. Sound dissimilar linear friction welding of A7075-T6 Al and mild steel by simultaneous interfacial deformation using higher forging speed. J Manuf Process 109, 512–523 (2024).

61. Chamanfar, A., Jahazi, M., Gholipour, J., Wanjara, P. & Yue, S. Maximizing the integrity of linear friction welded Waspaloy. Mater Sci Eng A 555, 117–130 (2012).

62. Li, W. Y. et al. Microstructure characterization and mechanical properties of linear friction welded Ti-6Al-4V alloy. Adv Eng Mater 10, 89–92 (2008).

63. Turner, R., Gebelin, J. C., Ward, R. M. & Reed, R. C. Linear friction welding of Ti-6Al-4V: Modelling and validation. Acta Mater 59, 3792–3803 (2011).

64. Schröder, F. et al. Linear friction welding of Ti6Al4V: Experiments and modelling. Materials Science and Technology (United Kingdom) 31, 372–384 (2015).

65. Ma, T. J., Li, W. Y. & Yang, S. Y. Impact toughness and fracture analysis of linear friction welded Ti-6Al-4V alloy joints. Mater Des 30, 2128–2132 (2009).

66. Choi, J. W., Aoki, Y., Ushioda, K. & Fujii, H. Linear friction welding of Ti-6Al-4V alloy fabricated below β-phase transformation temperature. Scr Mater 191, 12–16 (2021).

67. Choi, J. W., Aoki, Y., Ushioda, K. & Fujii, H. Effect of the welding parameters on microstructure and mechanical properties of linear friction welded Ti-6Al-4V alloy. J Manuf Process 75, 651–663 (2022).

68. Fujii, H., Aoki, Y., Zhao, Y. & Ushioda, K. Cold-dwell fatigue property of linear friction

welded Ti-6Al-4V alloy joint. in Proceedings of 15th World Conference on Titanium (Ti-2023), Institute of Materials, Minerals & Mining (IOM3) (Edinburgh, 2023).

69. Li, W., Wu, H., Ma, T., Yang, C. & Chen, Z. Influence of parent metal microstructure and post-weld heat treatment on microstructure and mechanical properties of linear friction welded Ti-6Al-4V joint. Adv Eng Mater 14, 312–318 (2012).

70. Bhamji, I., Preuss, M., Threadgill, P. L. & Addison, A. C. Solid state joining of metals by linear friction welding: A literature review. Mater Sci Tech, 27 2–12 (2011).

71. Ito, T., Kamai, M., Miura, T., Morisada, Y. & Fujii, H. Dissimilar joining of carbon steel, pure nickel and aluminum alloys by center-driven double-sided linear friction welding. J Adv Join 8, 100165 (2023).

72. Addison, A. Linear Friction Welding of Engineering Metals. TWI Industrial Members Report - 894/2008. Cambridge, U.K.; 2008.

73. McAndrew, A. R., Colegrove, P. A., Flipo, B. C. D. & Bühr, C. 3D modelling of Ti–6Al–4V linear friction welds. Sci Tech Weld Join 22, 496–504 (2017).

74. McAndrew, A. R., Colegrove, P. A., Bühr, C., Flipo, B. C. D. & Vairis, A. A literature review of Ti-6Al-4V linear friction welding. Prog Mater Sci, 92 225–257 (2018).

75. McAndrew, A. R., Colegrove, P. A., Addison, A. C., Flipo, B. C. D. & Russell, M. J. Modelling the influence of the process inputs on the removal of surface contaminants from Ti-6Al-4V linear friction welds. Mater Des 66, 183–195 (2015).

76. Guo, Y., Jung, T., Chiu, Y., Li, H., et al. Microstructure and microhardness of Ti6246 linear friction weld. Mater Sci Eng A 562, 17–24 (2013).

77. Turner, R., Ward, R. M., March, R. & Reed, R. C. The magnitude and origin of residual stress in Ti-6Al-4V linear friction welds: An investigation by validated numerical modeling. Metall Mater Trans B: 43, 186–197 (2012).

78. García, A. BLISK Fabrication by Linear Friction Welding. In: Benini E, Editor. Adv Gas Turbine Technol. Winchester: InTech; 411–434, (2011).

79. Leyens, C. & Peters, M. Titanium and Titanium Alloys: Fundamentals and Applications. 1st Ed. Darmstadt: Wiley-VCH; 2003.

80. Grujicic, M., Arakere, G., Pandurangan, B., Yen, C. F. & Cheeseman, B. A. Process modeling of Ti-6Al-4V linear friction welding (LFW). J Mater Eng Perform 21, 2011–2023 (2012).

81. Frankel, P., Preuss, M., Steuwer, A., Withers, P. J. & Bray, S. Comparison of residual stresses in Ti-6Al-4V and Ti-6Al-2Sn-4Zr-2Mo linear friction welds. Materials Science and Technology 25, 640–650 (2009).

82. Geng, P., Qin, G., Ma, H., Zhou, J., et al. Numerical modelling on the plastic flow and interfacial self-cleaning in linear friction welding of superalloys. J Mater Process Technol 296, (2021).

83. TWI Ltd, linear friction welding; https://www.twi-global.com/technical-knowledge/job-knowledge/linear-friction-welding-146, accessed on Feb 3 2025.

84. Ma, T., Li, W., Xu, Q., Zhang, Y., et al. Microstructure evolution and mechanical properties of linear friction welded 45 steel joint. Adv Eng Mater 9, 703–707 (2007).

85. Li, W. Y., Ma, T.J., Yang, S., Xu, Q., et al. Effect of friction time on flash shape and axial shortening of linear friction welded 45 steel. Mater Lett 62, 293–296 (2008).

86. Ofem, U. U., Colegrove, P. A., Addison, A. & Russell, M. J. Energy and force analysis of linear friction welds in medium carbon steel. Science and Technology of Welding and Joining 15, 479–485 (2010).

87. Li, W., Wang, F., Shi, S., Ma, T., et al. 3D Finite Element Analysis of the Effect of Process Parameters on Linear Friction Welding of Mild Steel. J Mater Eng Perform 23, 4010–4018 (2014).

88. Fratini, L., Buffa, G., Campanella, D. & La Spisa, D. Investigations on the linear friction welding process through numerical simulations and experiments. Mater Des 40, 285–291 (2012).

89. Wang, Y., Tsutsumi, S., Kawakubo, T. & Fujii, H. Microstructure, mechanical properties and fatigue behaviors of linear friction welded weathering steels. Int J Fatigue 159, 106829 (2022).

90. Wang, Y., Tsutsumi, S., Kawakubo, T. & Fujii, H. Fatigue strength and fracture characteristics of linear friction welded joints of weathering mild steel. Fatigue Fract Eng

Mater Struct 45, 2769–2783 (2022).

91. Miao, H., Tsutsumi, S., Yamashita, T., Morisada, Y. & Fujii, H. Fatigue strength improvement of linear friction welded butt joints of low carbon steel by pressurizing after oscillation. J Manuf Process 102, 795–805 (2023).

92. Li, Y., Liu, Y., Liu, C., Li, C., Ma, Z., et al. Microstructure evolution and mechanical properties of linear friction welded S31042 heat-resistant steel. J Mater Sci Technol 34, 653–659 (2018).

93. Nakamoto, T., Shirakawa, N., Miyata, Y. & Inui, H. Selective laser sintering of high carbon steel powders studied as a function of carbon content. J Mater Process Technol 209, 5653–5660 (2009).

94. Deng, D. FEM prediction of welding residual stress and distortion in carbon steel considering phase transformation effects. Mater Des 30, 359–366 (2009).

95. Tamaki, T., Kawakami, H., Suzuki, J. Effects of carbon content and peritectic reaction on hot cracking of high-carbon steel weld metal. Weld Int, 17, 26-35, (2010).

96. Miao, H., Yamashita, T., Tsutsumi, S., Morisada, Y. & Fujii, H. Multiple analyses of factors influencing fatigue life of linear friction welded low carbon steel. J Adv Join 9, 100201 (2024).

97. Miao, H., Yamashita, T., Ushioda, K., Tsutsumi, S., Morisada, Y., Fujii, H. Linear friction welding of T-Joints in low carbon steel: Effect of welding parameters on joint quality. J Adv Join 10, 100267 (2024).

98. Shotri, R., Miura, T., Geng, P., Morisada, Y., Ushioda, K., Fujii, H. Understanding thermal-mechanical variations and resulting joint integrity of pressure-controlled linear friction welding of thin-steel sheets. Int J Mach Tools Manuf 204, 104235 (2025).

99. Li, W., Vairis, A., Preuss, M. & Ma, T. Linear and rotary friction welding review. Inter Mater Rev, 61 71–100 (2016).

100. Shimizu, K., Nakayama, S., Shoji, H., Kawakubo, T., Nagira, T., Ohata, M., Fujii, H. Significance of fracture toughness for linear friction welded joint of weathering steel. Weld World, 69 739-750 (2024).

101. Kuroiwa, R., Liu, H., Aoki, Y., Yoon, S., Fujii, H., et al. Microstructure control of medium

carbon steel joints by low-temperature linear friction welding. Sci Tech Weld Join 25, 1–9 (2020).

102. Aoki, Y., Kuroiwa, R., Fujii, H., Murayama, G. & Yasuyama, M. Linear friction stir welding of medium carbon steel at low temperature. ISIJ International 59, 1853–1859 (2019).

103. Attallah, M. M., Preuss, M. & Bray, S. Microstructural development during linear friction welding of titanium alloys', Proc. 8th Int. Conf. on 'Trends in welding research', (ed. S. A. David et al.), 486–491; 2009, Materials Park, OH, ASM International. in.

104. Romero, J., Attallah, M. M., Preuss, M., Karadge, M. & Bray, S. E. Effect of the forging pressure on the microstructure and residual stress development in Ti-6Al-4V linear friction welds. Acta Mater 57, 5582–5592 (2009).

105. Grujicic, M., Yavari, R., Snipes, J. & Ramaswami, S. A linear friction welding process model for Carpenter Custom 465 precipitation-hardened martensitic stainless steel: A weld microstructure-evolution analysis. Proc Inst Mech Eng B J Eng Manuf 229, 1997–2020 (2015).

106. Orłowska, M., Olejnik, L., Campanella, D., Buffa, G., Morawinski, L., Fratini, L., Lewandowska, M. Application of linear friction welding for joining ultrafine grained aluminium. J Manuf Process 56, 540–549 (2020).

107. Sivaraj, P., Vinoth Kumar, M. & Balasubramanian, V. Microstructural characteristics and tensile properties of linear friction-welded AA7075 aluminum alloy joints. In: Lakshminarayanan, A., Idapalapati, S., Vasudevan, M. (eds) Advances in Materials and Metallurgy. Lecture Notes in Mechanical Engineering. Springer, Singapore. 467–476 (2019).

108. Lis, A., Mogami, H., Matsuda, T., Sano, T., Yoshida, R., Hori, H., Hiroshi. Hardening and softening effects in aluminium alloys during high-frequency linear friction welding. J Mater Process Technol 255, 547–558 (2018).

109. Mogami, H., Matsuda, T., Sano, T., Yoshida, R., et al. High-frequency linear friction welding of aluminum alloys. Mater Des 139, 457–466 (2018).

110. Buffa, G., Cammalleri, M., Campanella, D. & Fratini, L. Shear coefficient determination in linear friction welding of aluminum alloys. Mater Des 82, 238–246 (2015).

111. Buffa, G., Campanella, D., D'Annibale, A., di Ilio, A. & Fratini, L. Experimental and Numerical Study on Linear Friction Welding of AA2011 Aluminum Alloy. Key Eng Mater 611–612, 1511–1518 (2014).

112. Rotundo, F., Ceschini, L., Morri, A., Jun, T. S. & Korsunsky, A. M. Mechanical and microstructural characterization of 2124Al/25 vol.% SiCp joints obtained by linear friction welding (LFW). Composites Part A: Applied Science and Manufacturing vol. 41 1028–1037 (2010).

113. Mahoney, M. W., Rhodes, C. G., Flintoff, J. G., Spurling, R. A. & Bingel, W. H. Properties of Friction-Stir-Welded 7075 T651 Aluminum. (1998).

114. Komarasamy, M., Alagarsamy, K., Ely, L. & Mishra, R. S. Characterization of 3″ through-thickness friction stir welded 7050-T7451 Al alloy. Materials Science and Engineering: A 716, 55–62 (2018).

115. Choi, J. W., Li, W., Ushioda, K. & Fujii, H. Flat hardness distribution in AA6061 joints by linear friction welding. Sci Rep 11, (2021).

116. Choi, J. W., Li, W., Ushioda, K., Yamamoto, M. & Fujii, H. Strengthening mechanism of high-pressure linear friction welded AA7075-T6 joint. Mater Charact 191, (2022).

117. Choi, J. W., Li, W., Ushioda, K., Yamamoto, M. & Fujii, H. Microstructure evolution and hardness distribution of linear friction welded AA5052-H34 joint and AA5083-O joint. J Mater Res Tech 17, 2419–2430 (2022).

118. Matsuda, T., Adachi, H., Sano, T., et al. High-frequency linear friction welding of aluminum alloys to stainless steel. J Mater Process Technol 269, 45–51 (2019).

119. Matsuda, T. et al. Formation of interfacial reaction layer for stainless steel/aluminum alloy dissimilar joint in linear friction welding. Mater Today Commun 26, (2021).

120. Buffa, G., Cammalleri, M., Campanella, D., La Commare, U. & Fratini, L. Linear friction welding of dissimilar AA6082 and AA2011 aluminum alloys: microstructural characterization and design guidelines. Int J Mater Form 10, 307–315 (2017).

121. Kimura, M., Yukawa, T., Kusaka, M., Kaizu, K. & Fuji, A. Possibility of direct friction welding between type 7075 aluminum alloy and low carbon steel. in Proceedings of the 1st International Joint Symposium on Joining and Welding 267–273 (Elsevier, 2013).

122. Liu, H., Aoki, Y., Aoki, Y., Ushioda, K. & Fujii, H. Principle for obtaining high joint quality in dissimilar friction welding of Ti-6Al-4V alloy and SUS316L stainless steel. J Mater Sci Technol 46, 211–224 (2020).

123. Fujii, H. Low-temperature Linear Friction Welding of Metal and Alloys with 100％ Joint Efficiency. Keikinzoku Yosetsu/Journal of Light Metal Welding 58, 8–13 (2020).

124. Anderson, T. How to avoid cracking in aluminum alloys. Weld Journal (Miami, Fla.) 84, 25–7 (2005).

125. Cheng CM, Chou CP, Lee IK, Lin HY. Hot cracking of welds on heat treatable aluminium alloys. Sci Technol Weld Join 10, 344–52 (2005).

126. Kimura M, Kusaka M, Kaizu K, Hayashida K. Simultaneous friction welding and characterization of joints between 7075-T6 al alloy and low-carbon steel using pure al as an insert metal. J Mater Eng Perform 28, 7726–7736 (2019).

127. Ochi H, Ogawa K, Yamamoto Y, Kawai G, Tsujino R, Suga Y. Effect of intermetallic compounds on friction weldability of aluminum alloys to S25C carbon steel. J Soc Mater Sci 53, 532–538 (2004).

128. Nakashima R, Fuji A, Tohkuni H, Kimura M. friction welding of A7075/low carbon steel joint-Study with insert material. Preprints of the National Meeting of JWS 87, 15-16 (2010). (in Japanese)

129. Yamagishi H. Spot forge-welding for rapid dissimilar joining of Fe to Al to produce an intermetallic compound-free interface. Mater Trans 62:MT-M2021080 (2021).

130. Guili L, Fang G. Grain-boundary segregation and corrosion mechanism of Al-Zn-Mg-Cu ultra high strength aluminum alloys. Rare Metal Mat Eng 38, 1598–1601 (2009).

131. Zobac O, Kroupa A, Zemanova A, Richter KW. Experimental description of the Al-Cu binary phase diagram. Metall Mater Trans A 50, 3805–3815 (2019).

132. Matsuda F, Nakata K, Shimokusu Y, Tsukamoto K, Arai K. Effect of additional element on weld solidification crack susceptibility of Al-Zn-Mg alloy (Report I). Materials, Metallurgy &, Citation Transactions of JWRI 12, 81–87 (1983).

133. Lim Y, Morisada Y, Liu H, Fujii H. A sound dissimilar AA5052/S45C joint formed by uniform and simultaneous deformation of both materials using pressure-controlled joule

heat forge welding. ISIJ International 62 1715–1724 (2022).

134. Kimura M, Choji M, Kusaka M, Seo K, Fuji A. Effect of friction welding conditions and aging treatment on mechanical properties of A7075-T6 aluminium alloy friction joints. Sci Tech Weld Join 10, 406-412 (2005).

135. Zhu S, Shih H, Cui X, Yu C, Ringer SP. Design of solute clustering during thermomechanical processing of AA6016 Al–Mg–Si alloy. Acta materialia 203, 116455 (2021).

136. Engler O, Marioara CD, Aruga Y, Kozuka M, Myhr OR. Effect of natural ageing or pre-ageing on the evolution of precipitate structure and strength during age hardening of Al–Mg–Si alloy AA 6016. Mater Sci Eng: A 759, 520–529 (2019).

137. Boonma J, Khammuangsa S, Uttarasak K, Dutchaneephet J, Boonruang C, Sirikulrat N. Post-Weld Heat Treatment Effects on Hardness and Impact Strength of Aluminum Alloy 6061 Friction Stir Butt Weld. Mater trans 45, 1072-1076 (2015).

138. Edwards GA, Stiller K, Dunlop GL, Couper MJ. The precipitation sequence in Al–Mg–Si alloys. Acta materialia, 46, 3893-3904 (1998).

139. Yang M, Orekhov,A, Hu ZY, Feng M, Jin S, Sha G, Li K, Samaee V, Song M, Du Y, Tendeloo GV, Schryvers D. Shearing and rotation of β″ and β′ precipitates in an Al-Mg-Si alloy under tensile deformation: In-situ and ex-situ studies. Acta Mater. 220, 117310 (2021).

140. Philip A, Phillip D, Peter UJ, Matheus AT, Florian S, Lukas S, Stefan P. Unraveling the potential of Cu addition and cluster hardening in Al-Mg-Si alloys. Materialia 36, 102188 (2024).

141. Khan F, Miura T, Morisada Y, Ushioda K, Fujii H. Dissimilar joining of A7075 aluminum and SS400 steel utilizing center-driven double-sided linear friction welding using mild steel as a center material: Processing, mechanical and microstructure characterization. J Manuf Process 139, 67-80 (2025).

142. Watanabe T, Takayama H, Yanagisawa A. Joining of aluminum alloy to steel by friction stir welding. J Mater Process Technol 178, 342-349 (2006).

143. Uematsu Y, Kakiuchi T, Kondoh E, Tozaki Y, Ibrahim I. Fatigue behavior of dissimilar A6061/rolled steel (SS400) friction stir welds. Proceedings of the Japan Welding Society 31, 112-118 (2013).

Research achievement

Journal papers

1. **Furkan** K., Miura, T., Morisada, Y., Ushioda, K., Fujii, H., 2025. Novel sacrificing-sheet linear friction welding method to fabricate sound dissimilar joint between steel and aluminum alloy. *Science and Technology of Welding and Joining*, In-press. *https://doi.org/10.1177/13621718251353588*

2. **Furkan** K., Miura, T., Morisada, Y., Ushioda, K., Fujii, H., 2025. Process parameter optimization and bonding mechanism in dissimilar S45C/A6061 joints via novel sacrificing-sheet linear friction welding. *Journal of Advanced Joining Processes 12, 100331*. *https://doi.org/10.1016/j.jajp.2025.100331*

3. **Furkan** K., Miura, T., Morisada, Y., Ushioda, K., Fujii, H., 2025. Dissimilar Joining of A7075 Aluminum and SS400 Steel utilizing Center-Driven Double-Sided Linear Friction Welding using Mild Steel as a Center Material: Processing, Mechanical and Microstructure Characterization. *Journal of Manufacturing Processes* 139, 67-80. *https://doi.org/10.1016/j.jmapro.2025.02.017*

4. **Furkan** K., Miura, T., Ito, T., Morisada, Y., Ushioda, K., Fujii, H., 2024. Sound dissimilar linear friction welding of A7075-T6 Al and mild steel by simultaneous interfacial deformation using higher forging speed. *Journal of Manufacturing Processes* 109, 512–523. *https://doi.org/10.1016/j.jmapro.2023.12.023*

Conference proceedings: (International-01, National-05,)

1. **Furkan** K., Miura, T., Morisada, Y., Ushioda, K., Fujii, H., Novel Dissimilar Joining of AA7075 Aluminum and SS400 Steel utilizing Center-Driven Double-Sided Linear Friction Welding (CDDS-LFW) with Mild Steel Center Material. ***77th IIW Annual Assembly and International Conference on Welding and Joining, Rhodes, Greece,*** 7th-12th July 2024.
2. **Furkan** K., Miura, T., Morisada, Y., Ushioda, K., Fujii, H., Joining mechanism of sacrificing-sheet linear friction welding for dissimilar materials. ***Japan Welding Society (Spring lecture)***, ***Tokyo***, 22nd Apr- 24th Apr 2025.
3. **Furkan** K., Miura, T., Morisada, Y., Ushioda, K., Fujii, H., Novel Sacrificing-Sheet Linear Friction Welding of S45C Steel and A6061 Aluminum Alloy. ***Japan Welding Society (Fall lecture)***, ***Hokkaido,*** 4th Sep- 6th Sep 2024.
4. **Furkan** K., Miura, T., Morisada, Y., Ushioda, K., Fujii, H., High-quality A7075/SS400 dissimilar welding utilizing frictionally pre-heated insert material with center-driven linear friction welding. ***Japan Welding Society (Spring lecture)***, ***Osaka,*** 22nd Apr- 24th Apr 2024.
5. **Furkan** K., Miura, T., Morisada, Y., Ushioda, K., Fujii, H., Center Driven Double-Sided Linear Friction Welding of A7075 and Carbon Steel. ***Japan Welding Society (Fall lecture)***, ***Nagoya,*** 13th Sep- 15th Sep 2023.
6. **Furkan** K., Miura, T., Morisada, Y., Ushioda, K., Fujii, H., Dissimilar linear friction welding of 7075-T6 Al and low carbon steel. ***Japan Welding Society (Spring lecture)***, 25th April- 27th April 2023.

Poster presentation

1. **Furkan** K., Miura, T., Morisada, Y., Ushioda, K., Fujii, H., Novel Sacrificing-Sheet Linear Friction Welding of S45C Steel and A6061 Aluminum Alloy. ***Japan Welding Society***, ***Hokkaido,*** 5th Sep 2024.
2. **Furkan** K., Miura, T., Morisada, Y., Ushioda, K., Fujii, H., Center Driven Double-Sided Linear Friction Welding of A7075 and Carbon Steel. ***Japan Welding Society***, ***Nagoya,*** 14th Sep 2023.